

The Gregory-Laflamme Instability of Black Strings and Violation of the Weak Cosmic Censorship Conjecture



Chenxia Gu

School of Mathematical Sciences
Queen Mary, University of London

This dissertation is submitted for the degree of
Doctor of Philosophy

August 2023

I would like to dedicate this thesis to my loving parents.

Declaration

I, CHENXIA GU, confirm that the research included within this thesis is my own work or that where it has been carried out in collaboration with, or supported by others, that this is duly acknowledged below and my contribution indicated. Previously published material is also acknowledged below.

I attest that I have exercised reasonable care to ensure that the work is original, and does not to the best of my knowledge break any UK law, infringe any third party's copyright or other Intellectual Property Right, or contain any confidential material.

I accept that the College has the right to use plagiarism detection software to check the electronic version of the thesis.

I confirm that this thesis has not been previously submitted for the award of a degree by this or any other university.

The copyright of this thesis rests with the author and no quotation from it or information derived from it may be published without the prior written consent of the author.

Signature: CHENXIA GU Date: 26/02/2023

Details of collaboration and publications: parts of this work have been published in the following papers:

- P. Figueras, T. França, C. Gu, & T. Andrade, Endpoint of the Gregory-Laflamme instability of black strings revisited, *Physical Review D*, 107, 044028, 2023.
- T. Andrade et al., GRChombo: An adaptable numerical relativity code for fundamental physics, *Journal of Open Source Software*, 6(68), 3703, 2021.

Chenxia Gu
August 2023

Acknowledgements

First and foremost I would like to thank my supervisor Prof. Pau Figueras, who has always been supportive, motivative and encouraging me at every step throughout my Ph.D. journey. I really appreciate him for bring me into the field of numerical relativity. Thanks to his patient and consistent guidance and always pointing me to the right direction along the way. I would also like to thank Ulrich Sperhake for introducing me to the field of numerical relativity and Juan Valiente Kroon for his supervision and many intriguing discussions during my time at QMUL. Furthermore, I would like to thank my examiners, Dionysios Anninos and Shabnam Beheshti, for their valuable comments and suggestions.

I have been so lucky to be surrounded by so many collaborative friends and colleagues during my time in UK. I would like to thank Tomas Andrade and Tiago Frasca for collaborations on the project of black string simulations. I would like to thank everyone in our GRCHOMBO Team and in my research group at QMUL for providing such a collaborative environment. Thank my fellow PhDs, friends and colleagues at QMUL, especially Tiago, Peng, Biel, Lorenzo and Xianming, for many interesting and enjoyable discussions. Thank for the company of my friends during my stay at QMUL to Shaoxiong, Jin, Ye, Cheng and Mikeal for making my time in London so wonderful. Last but not least, I would like to thank Lizhi for always being by my side and my parents for their unconditional love and support from China for the years I was in UK.

My PhD is supported by the European Research Council Grant No. ERC-2014-StG 639022-NewNGR. In addition, I received funding from Queen Mary Postgraduate Research Fund from QMUL for attending conferences. For the work on black string, we would like to thank Roberto Emparan, Luis Lehner and Frans Pretorius for very useful comments and discussions on a draft of the article. We also want to thank

the entire GRCHOMBO ¹ collaboration, and Miren Radia in particular, for their support and code development work.

The simulations and calculations presented in this thesis used the following supercomputers:

- PRACE resources under Grant No. 2020235545, PRACE DECI-17 resources under Grant No. 17DECI0017, the CSD3 cluster in Cambridge under projects No. DP128 and No. DP214. The Cambridge Service for Data Driven Discovery (CSD3), partially operated by the University of Cambridge Research Computing on behalf of the STFC DiRAC HPC Facility. The DiRAC component of CSD3 is funded by BEIS capital via STFC capital Grants No. ST/P002307/1 and No. ST/R002452/1 and STFC operations Grant No. ST/R00689X/1. DiRAC is part of the National e-Infrastructure.² We gratefully acknowledge the Gauss Centre for Supercomputing e.V.³ for providing computing time on the GCS Supercomputer SuperMUC-NG at Leibniz Supercomputing Centre.⁴
- Sulis Tier 2 HPC platform hosted by the Scientific Computing Research Technology Platform at the University of Warwick. Sulis is funded by EPSRC Grant No. EP/T022108/1 and the HPC Midlands+ consortium.
- Apocrita HPC facility at QMUL, supported by QMUL Research-IT [1].
- Young Tier 2 HPC cluster at UCL. We are grateful to the UK Materials and Molecular Modelling Hub for computational resources, which is partially funded by EPSRC (No. EP/P020194/1 and No. EP/T022213/1).
- MareNostrum and the technical support provided by BSC (No. RES-FI-2020-3-0007).
- Athena at HPC Midlands+ cluster.
- ARCHER2 UK National Supercomputing Service.⁵

I would also like to thank the technical support and the computer resources received from the above institutions.

¹www.grchombo.org

²www.dirac.ac.uk

³www.gauss-centre.eu

⁴www.lrz.de

⁵www.archer2.ac.uk

Abstract

Einstein's general relativity is a remarkably successful theory of space, time and gravitation. Over a hundred years since its birth, it has been verified by all of the experiments and observations with incredibly high accuracy. It has shown us its power in predicting exotic objects such as gravitational waves and black holes. Despite its great success, its predictive power has been questioned due to the existence of the singularities which would break down the theory. This brings out the weak cosmic censorship conjecture, suggesting that singularities are always hidden inside black hole horizons so that they cannot cause any problem to the outside. Whether the conjecture is true or false remains as one of the biggest open questions in the field. Although a rigorous mathematical proof or disproof to the conjecture is still lacking, there have been evidence against it arising from a family of numerical studies on the Gregory-Laflamme instability. The most studied case that has tuned our current understanding of the conjecture is about the five-dimensional black strings. The first full numerical work done by Lehner and Pretorius suggests a pinch-off of the horizon at the endpoint of the Gregory-Laflamme instability of black strings, which provides solid evidence against the conjecture. However, their study is more than ten years old and has not been reproduced independently in any other literature. The development in numerical techniques and computer power facilitate us to have an independent study on the black strings.

In this thesis, we revisit the previous study by Lehner and Pretorius on the endpoint of the Gregory-Laflamme instability of the five-dimensional black strings. We not only reproduce and confirm their results with a different and independent formalism, but also improve the simulation with better resolution and extend the evolution much closer to the endpoint. The simulations in the thesis are conducted by using our own GRCHOMBO code. Our results provide further evidence about the fractal structure that the horizon develops into in the late-time dynamics of the black string instability. Moreover, we investigate unstable black strings with fixed thickness but different lengths and provide a more general picture of the development of the

instability. In all cases, we confirm that the intermediate dynamics of the evolution can be described by a quasi-stationary sequence of spherical black holes of various sizes connected by string segments on different scales. In particular, with better resolution, our results respect the particular symmetry of the problem. However, our numerical results do not support the existence of a global timescale relating subsequent generations as stated in the previous study. Instead, our results indicate that, due to the non-uniform development of the string, the late-time dynamics are governed by the joint effect from the Gregory-Laflamme instability and the local dynamics of the bulges. Finally, we confirm that the endpoint of the instability is the pinch off of the horizon in finite asymptotic time, which constitutes to the violation of the weak cosmic censorship conjecture.

Table of contents

List of figures	xi
List of tables	xv
1 Introduction	1
1.1 Structure of this thesis	5
2 Numerical Construction for Higher Dimensions	7
2.1 Numerical relativity for higher dimensions	8
2.2 The Einstein field equations	10
2.3 The $d+1$ split of spacetime	11
2.4 From EFE to CCZ4 formalism	12
2.4.1 The ADM formulation	13
2.4.2 The ADM version of Z4 system	14
2.5 Evolving with GRChombo	18
2.5.1 Code design	18
2.5.2 Mesh refinement	19
2.5.3 Tagging Criteria	19
2.6 Dimension reduction in numerical relativity	21
2.6.1 Dimension reduction by $SO(D-1)$ symmetry	21
2.6.2 Dimension reduction by $SO(D-n)$ symmetry	22
3 Analysis Methods for Higher Dimensional Black Holes	25
3.1 Black holes in higher dimensions	26
3.1.1 The Schwarzschild-Tangherlini solution	27
3.1.2 The Black string solution	27
3.2 Initial conditions	29
3.2.1 The Schwarzschild-Tangherlini solution	29
3.2.2 The black string solution	29

3.3	Apparent Horizon	31
3.3.1	Introduction	31
3.3.2	Numerical methods	33
3.3.3	Flow method	34
3.3.4	Newton-Raphson method	34
3.4	Embedding diagram	37
3.5	Curvature invariant	38
3.6	Black hole thermodynamics	38
3.6.1	The corrected thermodynamics	39
4	Endpoint of Black String Instability	41
4.1	Introduction	42
4.1.1	The weak cosmic censorship conjecture	43
4.1.2	The Gregory-Laflamme instability	44
4.1.3	Previous numerical evolution on the black string	46
4.2	Numerical methods	49
4.2.1	The evolution	50
4.2.2	Gauge conditions	51
4.2.3	Modified Gamma-Driver	52
4.2.4	Initial data	52
4.2.5	Singularity Diffusion	53
4.2.6	Localised perturbation	54
4.2.7	Grid hierarchy	55
4.3	Analysis methods	58
4.3.1	Apparent horizon	58
4.4	Results	59
4.4.1	The geometry of the AH	59
4.4.2	Horizon dynamics	60
4.4.3	Dynamics beyond the third generation	62
4.4.4	The evolution of horizon area	64
4.4.5	Properties of the horizon	66
4.4.6	Velocity profile	69
4.4.7	Approach to the singularity	70
4.4.8	Mode behaviour	72
4.5	Numerical tests	79
4.6	Discussion	82

5	Results from Strings with Different Lengths	84
5.1	The geometry of the horizons	85
5.2	The AH area	87
5.3	Horizon properties	89
5.4	Satellite formation	90
5.5	Approach to the singularity	93
5.5.1	The pinch off	94
5.5.2	Evolution of the proper length	95
5.5.3	Velocity profile	96
5.5.4	Mode behaviour	97
5.6	Discussion	100
6	Conclusion and Outlook	101
	References	104
	Appendix A Symmetry reduction terms	114
	Appendix B Numerical test	116

List of figures

2.1	The foliation of spacetime and the definitions for lapse and shift. (regenerated from [2])	11
2.2	Imposing $SO(3)$ to a scalar field $\mathbf{v}(r)$, vector field $\mathbf{v}(\mathbf{x})$ and tensor $(T_{\mathbf{x}})_{ij}$ in Cartesian coordinates.	22
4.1	A demonstration of the unstable black string that induces ripples along the compact string direction.	45
4.2	The embedding diagram of the apparent horizon from [3].	48
4.3	Examples of the grid hierarchy from two different refinement criteria from a black string with length $L = 16$. Left: grid hierarchy from χ tagging criterion. The grid structure is dynamically changing with the evolution based on the gradients of the evolution variable χ ; Right: grid hierarchy from rectangular tagging criterion. The location of each level depends on the resolution at the AH. The actual location of the AH is depicted in a red curve.	57
4.4	Embedding of the AH, with induced Kretschmann invariant (in red curve) imposed on the AH.	60
4.5	Zoom-in of the region near the 3rd generation on the embedding of the AH. The induced Kretschmann invariant is imposed on the AH in red curve.	60
4.6	Snapshots of the embedding diagrams of the AHs in our simulation at different stages. The length in the Z direction extends to 13.69 in the $L = 10$ case.	61
4.7	Embedding diagrams of the AH. After the second generation has formed, the string connecting the first and the second generations become non-uniform, which triggers the formation of the third generation.	63

4.8	Embedding diagrams of the AH at the late stages. We can see the third generations has fully formed, and the fourth and fifth one are coming up.	64
4.9	Evolution of the AH area for the unstable black string in 5D with 4D mass parameter $r_0 = 1$ and $L = 10$. The black dashed line is the area for a 5D Schwarzschild BH. And the red dashed line is the corrected area for a 5D Schwarzschild BH in KK space.	65
4.10	Evolution of the AH area for the unstable black string in 5D with 4D mass parameter $r_0 = 1$ and $L = 10$. The red dashed line is the total area for two BHs.	66
4.11	Time derivative of the logarithm of the equatorial radius for each of the generations for the $L = 10$ case as a function of time.	68
4.12	The tangential velocity and radial velocity at the final stage of the evolution of the $L = 10$ run.	70
4.13	Logarithm plot of the areal radius R of the AH vs the time to the pinch off for the $L = 10$ run. We also display the evolution of the radius of several generations and the minimal radius on the string. .	71
4.14	Plot of the proper length vs. time in logarithmic coordinates for $L = 10$ run. The slope of the dotted line, which is a linear fit to the late-time data, is ~ 0.053	72
4.15	The evolution of the AHs at $t=0, 50, 68$. This is the period before the first generation is about to form.	73
4.16	Values of the expansion coefficients for the whole string.	74
4.17	The evolution of the AHs at $t=100, 110, 117$, when it is at last stage of the formation of the first generation, but before the second generation has fully formed.	74
4.18	Values of the expansion coefficients for the string segment corresponding to the 1st generation.	75
4.19	The evolution of the AHs at $t=120, 121, 122$, when it is at last stage of the formation of the second generation, but before the third generation has fully formed. The fitted curves are plotted in red. . .	76
4.20	Values of the expansion coefficients for the string segment corresponding to the 3rd generation.	77
4.21	The AH at $t=126$ (in red).	77
4.22	The evolution of the AHs at $t=125.9, 126.1$ and 126.4 for z in $[2.8, 4.6]$. .	78
4.23	Values of the expansion coefficients for the string segment on the left corresponding to the 4th generation.	78

4.24	The evolution of the AHs at $t=125.9, 126.1$ and 126.4 for z in $[5, 5.7]$.	79
4.25	Values of the expansion coefficients for the string segment on the right corresponding to the 4th generation.	79
4.26	Test results for the outer boundary at 80, 160 and 256, respectively. The glitch indicates that the outer boundary starts to have some effects on the inside physics.	80
4.27	Test results from the medium and high resolution respectively. The glitch indicates when the outer boundary starts to have some effects on the inside physics.	80
4.28	Convergence test for the AH area for the $r_0 = 1, L = 10$ black string. The medium resolution run has spacing $h = 0.25r_0$ in the coarsest grid level. This plot shows that the order of convergence is roughly three. The computational cost of the high resolution run limited the time of the tests.	81
5.1	Top: Embeddings of the geometry of the AH at the last stage of our simulations for $L = 8, 10, 12, 16$, from top to bottom; the corresponding length along the Z direction is 11.32, 13.69, 15.90 and 21.03 in units of r_0 , respectively. For better visualisation, we have rescaled the height of the plots so that all of them have the same width while maintaining the proportions of the embeddings. The induced Kretschmann invariant is superposed to the AH in red. Bottom: zoom in of the thinnest part near the second generation on the string in the $L = 10$ case, where we can see the third and fourth generations are obviously visible. The fourth is growing and moving towards the first blob. The fifth generation is about to form as well.	86
5.2	Evolution of the AH area for the unstable black string in 5D with 4D mass parameter $r_0 = 1$ and different L 's. The dashed lines indicate the area for a slightly deformed 5D KK black hole with the same mass as the unperturbed black string [4]; The dotted lines are the areas of two black holes on a circle [5] with the same total mass as the unperturbed black string and the same radii as the first and second generation blobs measured at the end of the simulation. . . .	88
5.3	Radius ratio of the first and second generations.	89
5.4	Snapshots of the embedding diagrams of the AHs in our simulation at different stages. The length in the Z direction extends to 11.32 in the $L = 8$ case.	91

5.5	Local dynamics of the bulges for the $L = 12$ case. The third and fourth generation bulges do not have enough time to fully form before being absorbed by the existing second generation bulge on the left. On the other hand, the fifth generation bulge fully forms and by the end of our simulation it is moving towards the second generation bulge. From the last panel we can see the sixth generation is about to form.	92
5.6	The areal radius R of the AH as a function of the time to the singularity in the logarithmic coordinates, for the $L = 8, 10, 12, 16$ cases, from left to right and top to bottom, respectively. We display the evolution of the minimum string radius R_{min} as well as the equatorial radii of several generations. The grey dashed line is a visual add of the linear fit to the late-time minimal radius.	94
5.7	The proper length of the string as a function of the logarithm of the time to the singularity in the logarithmic coordinates, for the $L = 8, 10, 12, 16$ cases, from left to right and top to bottom, respectively. The dashed line is linear fit to the late-time development of the proper length. The slop is 0.053, 0.053, 0.049, 0.049 for the $L = 8, 10, 12, 16$ cases, respectively.	95
5.8	Velocity profile at the last stage of the simulations for $L = 8, 10, 12, 16$, from top to bottom, respectively. The tangential and orthogonal velocities are shown in red and blue curves respectively.	96
5.9	Mode behaviour of the first string segment for different L 's, from $t_{n,1}$ to $t_{p,2}$	98
5.10	Mode behaviour of the second string segment for different L 's, from $t_{n,2}$ to $t_{p,3}$	99
B.1	Convergence test for the AH area for the $r_0 = 1$, $L = 10$ black string. This plot shows that the order of convergence is roughly three. The computational cost of the high resolution run limited the time of the tests.	116
B.2	Convergence test for the AH area for the $r_0 = 1$, $L = 10$ black string. This plot shows that the order of convergence is roughly three. The computational cost of the high resolution run limited the time of the tests.	117

List of tables

4.1	Properties of the black string apparent horizon (by 1.5 radius of the surrounding string segment)	67
4.2	Properties of the black string apparent horizon (by first negative peak of the radial velocity)	69
5.1	Properties of the various generations according to our definitions for the time of formation.	90
5.2	Slope of the scaling law (5.2) and the estimated pinch off time for the different L 's.	94

Chapter 1

Introduction

General relativity (GR), postulated by Einstein in 1915, is a beautiful theory of space, time and gravitation. It is widely appreciated for its simple and elegant form and concepts. In GR, gravity becomes a geometric property of spacetime so that every gravitational interactions in the universe can be described by just one simple line of equations. Such unconventional viewpoint of space and time is rather counterintuitive, which challenges the way in which we are used to think. It is undeniable that the birth of GR marks as a new era of our understanding of the universe, but the abstruse concepts of the theory make it very difficult to understand. Probably on this account, the field of GR has been dormant for almost half a century, until the interests in GR have been revived by the needs from the development of other fields in physics, such as astronomy and quantum theory of gravitation. The field of GR stays active since then. On the other side, GR has also laid the foundation to the field of astrophysics and cosmology, which have largely improved our understanding of the universe in large scale. Apart from its impact on other fields in physics, GR per se is universally acknowledged as a remarkably successful theory. Over a hundred years since its birth, it has passed all the experimental and observational tests with extraordinary accuracy [6]. In particular, it has shown its power in predicting exotic objects and events, such as black holes and gravitational waves.

Lying in the core of GR is the Einstein field equations (EFE), which is acknowledged as one of the most beautiful equations in human history. It is appreciated for its universal ability to describe and predict any gravitational interactions in the universe with very simple concepts and its elegant form. The majority of the current work in the field are related to solving the EFE. Due to the high non-linearity of

EFE, its mathematical properties are hard to analyse and the analytical solutions are very difficult to find. So far, there are only a few exact solutions, most of which are found in extreme conditions such as under symmetry assumptions of the problem. Among all the solutions, black holes (BHs) are one of the most important predictions by GR. As the simplest solutions of GR that capture the key aspects of the theory, BHs are crucial to our understanding of gravity. The first BH solution, the Schwarzschild solution, was found just a few months after the formulation of general relativity, under spherical symmetry assumption [7]. Years later after the discovery of Schwarzschild solution, a generalisation to the charged case was found, known as the Reissner-Nordström solution [8, 9]. After that, it took almost 50 years for a more complicated solution, the Kerr solution to be found, which depends on mass and angular momentum [10].

Although the existence of BHs has been predicted a hundred years ago, its astrophysical evidence has only become available recently. The landmark event of science happened in 2015. With the breakthrough of the accuracy of the detectors, the first direct detection of gravitational waves have been made and announced by the LIGO/Virgo collaboration [11, 12], from two merging BHs. It not only confirms the existence of gravitational waves which were predicted by Einstein in 1916, but also adds as a piece of indirect evidence for BHs. Since then, more gravitational wave events of various types have been detected by Advanced LIGO/Virgo/KAGRA, from mergers that involve neutron stars and BHs with huge disparity in mass [13–21]. More recently, the first images of the event horizons of the BHs M87* and Sgr A* have been published [22, 23]. It was the first time that we have the direct visualisation of BHs, which brings us to a new stage of exploring black hole physics. It is now widely accepted that BHs are ubiquitous in our universe. It is truly remarkable that the current observational data are highly consistent with the predictions by GR. With the improvement of techniques and sensitivity in the detectors, it is expected that more detections would become available in the upcoming years, which will allow us to test more aspects of the theory in the strong gravity regime.

Despite the success of GR, its predictive power has been questioned as the theory seems to have its own flaws: the singularities. Singularities are where the curvature would blow up and anything bizarre could happen to the metric that describes the spacetime at the singularities. It seems to be ubiquitous phenomena that our universe has singularities, such as the ones at the Big Bang and in the interior of BHs. However, the singularities predicted above are based on highly symmetric

conditions. This makes people wonder whether singularities actually exist, as there is a possibility that the singularities are just the product from the extreme conditions. In 1965, Penrose proved that singularities are generic features, as he found that the ultimate fate of a star is always a black hole [24]. He and Hawking further postulated the singularity theorem and proved the existence of the singularities [25]. The existence of singularities would cause the entire theory built by GR to fall down. The reason is that due to the extreme conditions near the singularities, all the physical laws are broken and the description of the spacetime by EFE becomes invalid. Everything built up by GR would therefore collapse, putting into doubt the integrity of the theory. For a theory to stand, this is not acceptable to have such singularities that break the laws of physics. The fact that the singularities seems always to be covered by black hole horizons motivates Penrose to postulate the weak cosmic censorship conjecture (WCCC) [26]. The conjecture states that singularities must be covered by BH horizons, denying the existence of naked singularities [27–29]. The modern formulation of the WCCC is presented in chapter 4. As long as the singularity is inside the horizon, it will not cause any problem to the outside. For decades, many efforts have been put into formulating and verifying the conjecture [30, 29]. However, a mathematical proof or disproof is still lacking. Whether the conjecture is true or false is still one of the most important open questions in the field of mathematical relativity.

Another important question in GR is whether the theory stands in higher dimensions. Recently, increasing attentions have been paid to higher dimensional GR. It is interesting from both physical and mathematical point of view. For mathematics, it is interesting to understand whether the dynamics of the solutions to certain systems of PDEs (in our case, vacuum EFE) are related to the number of dimensions that one considers. It is sensible and natural to think that the spacetime of the world we live in has four dimensions. Therefore, most work in the field has restricted their attention to four dimensions. However, the characteristic of EFE makes it possible to be generalised to arbitrary dimensions. This motivates people to ask whether its properties in four dimensions still hold for higher dimensions and what are the structure of the solutions in higher dimensions. On the other end, from physical point of view, physical theory requires higher dimensions. The earliest study in higher dimensions can be traced back to the study by Kaluza and Klein about gravitation and electromagnetism [31, 32]. More recently, the search for a quantum theory of gravity also motivates the study on higher dimensions. Moreover, ideas from brane-world cosmology, string theory and gauge/gravity duality rises more

attention to study BHs in higher dimensions. In addition, the singularity theorem proves the existence of the singularities, but it gives little information about its properties. The nature and the structure of the singularities are still mysterious. The study of singularities also leads to finding a unified theory that can be applied to the singularities, which involves higher dimensions. In contrast, studies in higher dimensions can in turn give insight to our understanding of the theory in four dimensions.

It turns out that the dynamics of the solutions to the EFE in higher dimensions is richer than that within the usual 3+1 dimensions. In 1993, Gregory and Laflamme found that black strings are unstable to long wavelength perturbations [33]. With the development of numerical relativity, in 2010, Lehner and Pretorius carried out the first full numerical evolution of the black strings and concluded that the endpoint of the Gregory-Laflamme (GL) instability is a naked singularity [3]. Their study provides a concrete counterexample to the WCCC. Recent years, a family of counterexamples in higher dimensions are found by numerical studies on the endpoint of the GL instability in similar scenarios [34–37]. It seems the conjecture is likely to be false in higher dimensions. The studies in higher dimensions could give more insight to the verification of the conjecture. If the WCCC is false, then GR will lose its predictive power. On the other hand, the extensive study in rapidly spinning asymptotically flat BHs [38–41], black rings [42], and in anti-de Sitter BHs [43, 44] indicates that the GL instability is a very general phenomenon in higher dimensions. It no doubt brings up more interests in studying the physics of the higher-dimensional BHs in different scenarios.

In this thesis, we carry out numerical simulations to explore the spacetime dynamics in higher dimensions and the gravitational instabilities that violates the weak cosmic censorship conjecture. We focus on a simple and fundamental object in higher dimensions: black strings. Our goal is to reproduce the previous study on the numerical evolution of the five-dimensional black strings with an independent method and improve and extend the simulation with higher resolution. First, we build up the numerical construction for evolving the spacetimes in higher dimensions and develop numerical methods to achieve stable simulations and analyse the results in higher dimensions. In particular, we focus on applying the numerical formulation and techniques to the study of the black string instability in five dimensions. Then, we carry out simulations and compare the results with the previous study [3]. We aim to improve the simulation results with higher resolution and extend the evolution further to explore more about the late-time dynamics of the GL

instability. Moreover, we explore strings with different lengths to obtain a more general picture of the development of the GL instability. In order to reduce the cost of computational resources, the modified Cartoon method has been applied to impose the symmetry of the problem [45, 46]. Applying symmetry reduced the computational and memory usage associated with the problem, allowing the researchers to obtain results on the supercomputers available at the time. The numerical simulations in the thesis are carried out by using our own `GRCHOMBO` code [47, 48]. It is an open source library for numerical relativity, developed and maintained by a group of researchers from Argonne National Laboratory, King's College London, Queen Mary University of London, the University of Cambridge and the University of Oxford. The code is based on finite difference method and is built on top of the `CHOMBO` framework [49], adapting `CCZ4` formulation and featured with fully adaptive mesh refinement techniques. It has many applications in various research areas and has been published in many papers [1, 34–37, 50–82]. Based on `GRCHOMBO` code, we generalised the code to work in higher dimensions with our specific problems.

1.1 Structure of this thesis

This thesis is organised as follows. Chapter 1 gives a brief overview about the field of GR, its great success in predicting exotic objects, its latest advances and its limitations. Then it presents the aspects we would like to explore in the field, as well as the motivations to work in higher dimensions by numerical relativity. More relevant background corresponds to our studies in higher dimensions is given at the beginning of the rest of each chapter.

Chapter 2 provides the relevant background of numerical relativity in higher dimensions and presents the necessary numerical construction for working in higher dimensions. It also demonstrates the general numerical techniques used in our study, including the modified Cartoon method. In addition, it gives an overview of the main features and applications of the `GRCHOMBO` code. The specific numerical methods and analysis methods designed for higher dimensional BHs are introduced in Chapter 3. In addition, we demonstrate how we monitor the dynamics and track the geometry of the apparent horizon during the evolution.

In Chapter 4, we present in detail the numerical methods we use to reproduce the numerical evolution on determining the endpoint of the black string instability. We provide details about our choice of the parameters, initial conditions and the grid

hierarchy. Then we demonstrate our simulation results and compare our results with the previous study [3]. We also provide the key results from the convergence tests. We confirm that the horizon will pinch off in finite asymptotic time. However, different than what is stated in [3], we find no evidence for the universal time-scale in terms of the time relating the subsequent generations.

In Chapter 5, we explore strings with different lengths and provide a more general picture on the late-time dynamics of the GL instability of the black strings. In particular, we find that the local dynamics together with the GL instability governs the late-time evolution of the horizon. We conclude that in finite asymptotic time there is a pinch off of the horizon in all cases. We provide more results about the convergence tests in the Appendix [B](#).

Finally, we summarise our results from the black string simulations in Chapter 6 and outline directions for future research, including follow-up studies about the pinch-off and higher derivative corrections.

Chapter 2

Numerical Construction for Higher Dimensions

The Einstein field equations (EFE) are written in generalised coordinates of space-time. The whole system consists of ten coupled non-linear partial differential equations, which has thousands of terms if we fully expand it. Therefore, solving the EFE turns out to be difficult in practice. Due to its fully non-linearity and high complexity, there are very few analytical solutions to it. Exact solutions are only discovered under high symmetry assumptions. It is simply impossible to solve the equations exactly for fields with less symmetry or strong dynamics. The needs of finding these solutions brings out a new field, numerical relativity, which turns out to be a powerful tool to study systems in highly dynamical and non-linear regime. Indeed, numerical relativity is probably the most powerful way to reveal the nonlinear dynamics of the spacetime, as it can help investigate scenarios that could never be considered before which could lead to new and deeper understanding of compact objects and their dynamics [83]. For example, gravitational waveforms can be generated from numerical simulations of the merger of binary black hole and neutron star system and compared with the observational data. Especially in higher dimensions where black holes are found to have exotic geometry and unusual dynamics, their mathematical properties are very hard to find due to the complexity of the EFE. Hence, numerical relativity becomes one of the most important tools to study the black hole solutions and general relativity in higher dimensions.

In this chapter, we first give an overview of the relevant numerical relativity background for higher dimensions in Sec. [2.1](#). Then, we present the numerical constructions from the EFE to CCZ4 formulation that we use to evolve systems in

higher-dimensional scenarios in our study in Sec. 2.2. In particular, we present the generalisation of the $3 + 1$ formalism to $d + 1$ dimensions. In Sec. 2.5, we introduce the main features of the GRCHOMBO code where we carry out the evolution. In addition, we introduce dimension reduction by different symmetries and present the reduced terms by modified cartoon method in Sec. 2.6 and Sec. A.

2.1 Numerical relativity for higher dimensions

In order to have an intuitive idea of the dynamical nature of the EFE, most of the numerical studies have adapted $3 + 1$ decomposition of the spacetime. In this way, it can break the 4D covariance of the field equations and separate the spacetime into the three spatial dimensions and the time dimension. In this way, the EFE can be posed as a Cauchy problem which can be solved numerically on supercomputers. Most of the current three-dimensional codes of numerical relativity adapt the following two formulations. One famous formulation is known as Harmonic formulation [84], which is based on a fully 4D form of the EFE in harmonic coordinates. The other one is called the ADM formalism. It was initially published in 1959 [85], named after its authors Richard Arnowitt, Stanley Deser, and Charles W. Misner. Although the original ADM formalism was rarely used in numerical simulations for technical reasons, it was considered as a starting point of many numerical constructions. In practice, the one in use is the conformal and traceless reformulation of the $3+1$ ADM equations [85], which is also known as the Baumgarte-Shapiro-Shibata-Nakamura (BSSN) formulation [86–88]. The development of numerical relativity was very slow due to the lack of sufficient power of computers.

Nowadays, most of the numerical relativity codes are based on the improved versions of the above formulations: the conformal covariant formulation of Z4 system (CCZ4) [89] and the generalised harmonic formulation (GH) [90]. Each formulation has its own advantages and disadvantages. The GH formulation is derived from coordinates that resemble the harmonic coordinates. It has the advantage of being well-known for its principle part as a wave equation and thus numerical studies can benefit from its well-known properties. However, GH formulation is unable to deal with the physical singularity. As a result, horizon excision is needed to handle the region inside the horizon. This means we need to get rid of the inner region inside the horizon and evolve the system by applying some boundary conditions at the edges of the inner region. Therefore, special numerical techniques are needed for handling

the computational domain inside the horizon to make sure that the inside will not pollute the physics outside. The CCZ4 formulation is an improved version of BSSN. In contrast, CCZ4 separates the physical singularity into a conformal factor. It has well-tested and robust gauge conditions such as the $1+\log$ family [91]. Similarly, the spatial gauges can rely on the hyperbolic Gamma-driver condition for the shift vector [92] (or some recent variants for unequal-mass binaries [93–95]), which removes to a large extent, the gauge dynamics near the compact objects. When combined, these two gauge choices eliminate the need to excise a region of the computation domain inside the apparent horizon. Instead, we can evolve on the whole domain which greatly simplifies the numerical infrastructure. Both are wisely used in many studies and provide reliable results. For example, in the numerical study of black strings [3] has used GHC. The CCZ4 formulation has successfully evolved binary black hole and binary neutral star systems [89, 96]. The main advantage of CCZ4 formulation over GH formulation is that there is no need for excision. It means with CCZ4 the calculations for locating the apparent horizon can be separated from the process of evolving the spacetime. However, in GH formulation, apparent horizon needs to be found periodically during the evolution in order to excise the singularity from the computational domain [84].

Most of the numerical studies based on the above two formulations have restricted their focus on spacetimes in four dimensions, but increasingly attention has been paid to higher spatial dimensions. Study in higher dimensions can reveal new phenomena that are not apparent in four dimensions. With the development in both theoretical work and numerical techniques, as well as the advances in the power of computational resources, it has become possible to study the dynamics in higher dimensions by numerical simulations. With the aid of numerical relativity, the non-linear dynamics can be uncovered. On the other side, numerical study in higher dimensions usually means higher cost of computational resources. In fact, the cost can grow exponentially with the number of extra dimensions, especially when there is less symmetry of the problem. When there is symmetry in the problem, it is possible to reduce the dimension of the problem by modified Cartoon method which can make the computations more affordable [45, 46, 97]. Due to limited computational domain, one sometimes needs to apply some artificial boundary conditions at the outer boundary of the computational domain. One need to be careful about the constraint violations from the boundary, which can propagate to the inside and sometimes affect the evolution. One usual way to fix this issue is to put the outer boundary far away enough. The reduced equations of BSSN

formulation by Cartoon method can be found in [46], which can be easily generalised to CCZ4 formulation. In higher dimensions, we just need to solve the Einstein field equations of the same form. In the rest of this chapter, we present the derivation of the CCZ4 formalism of numerical relativity in arbitrary dimensions, which is suitable for simulating a large variety of spacetimes in higher dimensions.

2.2 The Einstein field equations

In 1915, Einstein formulated the field equation of general relativity, known as the *Einstein field equations* (EFE) [98],

$$G_{ab} = 8\pi T_{ab}, \quad (2.1)$$

where $a, b = 0, 1, 2, 3$ and G_{ab} and T_{ab} are the Einstein tensor and the stress-energy tensor. Here Latin indices a, b, \dots denote for the spacetime indices of the tensor components running from 0 to 3. The EFE is written in a fully covariant form, which means there is no distinction between space and time. It is a quite natural result from differential geometry. From this point of view, this fully covariant form provides a better understanding of the relation between space and time. It is so compact and simple that all gravitational interactions in the universe can be described by this one single line of equations. However, sometimes we would like to rewrite the equations in some other ways in order to recover the dynamical evolution of the gravitational field, as the form that the EFE takes is not suitable for numerical evolutions. One common way is called $3 + 1$ formalism, where spacetime is split into three-dimensional space and time, so that given certain initial data, the subsequent evolution can be recovered in time. Thus, the problem can be turned into an initial value problem (IVP), and can be solved numerically.

The form that the EFE takes makes it possible to be generalised to higher dimensions. We define the number of spacetime dimensions as D and the number of spatial dimension as $d = D - 1$. In D dimensions, the equations we want to solve is

$$^{(D)}G_{\mu\nu} = 8\pi T_{\mu\nu}, \quad (2.2)$$

where $^{(D)}G_{\mu\nu}$ and $T_{\mu\nu}$ are the D -dimensional Einstein tensor and the stress-energy tensor. Here we use Greek letters for spacetime dimensions, i.e. $\mu, \nu, \dots = 0, 1, 2, \dots, d$. Then, to turn the problem into an IVP, we need the generalisation of the $3+1$ formalism to $d + 1$ dimensions accordingly.

2.3 The d+1 split of spacetime

First, by splitting the D -dimensional spacetime into d dimensions in space and one dimension in time, we can obtain a simple generalisation of the usual $3+1$ formalism [2] to arbitrary dimensions, i.e. the $d+1$ decomposition of spacetime. In $d+1$ decomposition, the spacetime \mathcal{M} is foliated into d -dimensional spacelike hypersurfaces Σ_t , such that $\mathcal{M} = \cup_{t \in \mathbb{R}} \Sigma_t$. On each hypersurface Σ_t , there is a coordinate system (t, x^i) , where x^i is a chart for each hypersurface. We define two functions to relate the coordinates in two adjacent slices: the lapse function α and the shift vector β^i , as shown in Fig. 2.1.

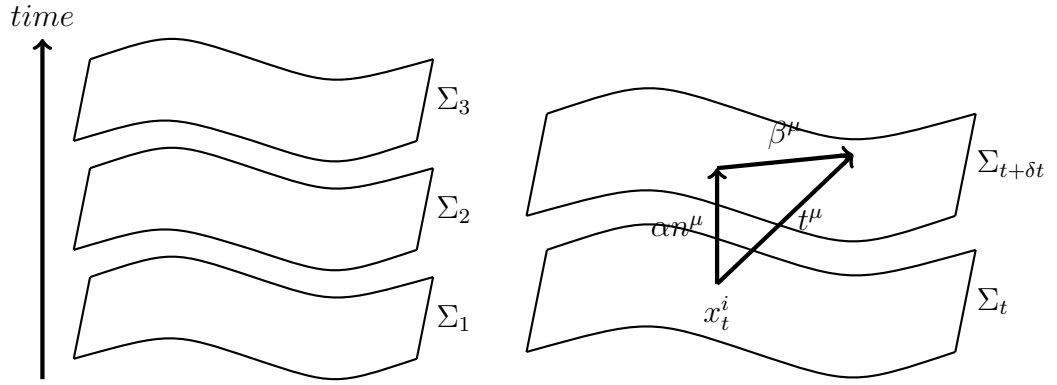


Fig. 2.1 The foliation of spacetime and the definitions for lapse and shift. (regenerated from [2])

The lapse measures the proper time between two adjacent hypersurfaces:

$$d\tau = \alpha dt,$$

and the shift measures the changes in the spatial coordinate systems:

$$x_{t+dt}^i = x_t^i - \beta^i(t, x^j) dt.$$

So we can construct a time vector that is tangent to the time lines as

$$t^\mu := \alpha n^\mu + \beta^\mu.$$

Evidently, the components of the normal vector can be found as

$$n_\mu = (-\alpha, 0), \quad n^\mu = \left(\frac{1}{\alpha}, -\frac{\beta^i}{\alpha}\right).$$

On each hypersurface, the *spatial metric* γ_{ij} is simply defined as the metric induced on each hypersurface by the *full spacetime metric* $g_{\mu\nu}$ as

$$\gamma_{\mu\nu} = g_{\mu\nu} + n_\mu n_\nu, \quad \gamma^{\mu\nu} = g^{\mu\nu} - n^\mu n^\nu.$$

In terms of $\{\alpha, \beta^i, \gamma_{ij}\}$, the metric takes the following form:

$$ds^2 = (-\alpha^2 + \beta_i \beta^i) dt^2 + 2\beta_i dt dx^i + \gamma_{ij} dx^i dx^j. \quad (2.3)$$

More explicitly, the components of the spatial metric are found to be

$$\gamma_{ij} = \begin{pmatrix} -\alpha^2 + \beta_m \beta^m & \beta_i \\ \beta_j & \gamma_{ij} \end{pmatrix}, \quad \gamma^{ij} = \begin{pmatrix} -1/\alpha^2 & \beta^j/\alpha^2 \\ -\beta^i/\alpha^2 & \gamma^{ij} - \beta^i \beta^j/\alpha^2 \end{pmatrix}. \quad (2.4)$$

After we have the above definitions, we are now ready to reformulate the EFE.

2.4 From EFE to CCZ4 formalism

In this section, we will illustrate how we reconstruct the EFE to the CCZ4 formulation that we use for numerical evolutions. We start with the ADM equations, which is the first and most popular way to reformulate the EFE to be conformal and traceless. To reformulate it to the $d+1$ ADM equations, we need to write the Einstein equations in $d+1$ language. First, we need to rewrite the EFE in terms of the extrinsic curvature and the d -dimensional Riemann curvature of the hypersurface, before we can derive from ADM to CCZ4 formalism.

The *extrinsic curvature* $K_{\mu\nu}$ is defined as

$$K_{\mu\nu} := -\perp_\mu^\alpha \nabla_\alpha n_\nu = -(\nabla_\mu n_\nu + n_\mu n^\alpha \nabla_\alpha n_\nu). \quad (2.5)$$

where \perp_β^α is the projection operator onto the spatial hypersurface, i.e. $\perp_\beta^\alpha := \delta_\beta^\alpha + n^\alpha n_\beta$.

The full projection of the Riemann tensor onto the hypersurfaces is given by the *Gauss-Codazzi* equations

$$\perp_\alpha^\delta \perp_\beta^\kappa \perp_\mu^\lambda \perp_\nu^\sigma R_{\delta\kappa\lambda\sigma} = {}^{(d)} R_{\alpha\beta\mu\nu} + K_{\alpha\mu} K_{\beta\nu} - K_{\alpha\nu} K_{\beta\mu}. \quad (2.6)$$

The projection of the Riemann tensor onto the hypersurfaces contracted with the normal vector is given by the *Codazzi-Mainardi* equations

$$\perp_\alpha^\delta \perp_\beta^\kappa \perp_\mu^\lambda n^\nu R_{\delta\kappa\lambda\sigma} = D_\beta K_{\alpha\mu} - D_\alpha K_{\beta\mu}, \quad (2.7)$$

where D_i is the d -dimensional covariant derivative. It is in fact the projection of the full D -dimensional covariant derivative: $D_\mu = \perp_\mu^\alpha \nabla_\alpha$. The full derivation can be found in [99].

2.4.1 The ADM formulation

After we have the definitions in the previous section, the Einstein equations can then be decomposed into evolution equations and constraint equations, which gives rise to the *Arnold-Deser-Misner* (ADM) formulation [85]. Let K denote the *trace* of the extrinsic curvature and ${}^{(d)}R_{\nu\rho\sigma}^\mu$ is the d -dimensional Riemann tensor. The ADM formulation is given below (with i, j running over spatial dimensions only):

$$\begin{aligned} \partial_t \gamma_{ij} - \mathcal{L}_\beta \gamma_{ij} &= -2\alpha K_{ij} \\ \partial_t K_{ij} - \mathcal{L}_\beta K_{ij} &= -D_i D_j \alpha + \alpha \left({}^{(d)}R_{ij} + K K_{ij} - 2K_{ik} K_j^k \right) \\ {}^{(d)}R + K^2 - K_{ij} K^{ij} &= 16\pi\rho \\ D_j \left(K^{ij} - \gamma^{ij} K \right) &= 8\pi j^i \end{aligned} \quad (2.8)$$

where $\rho := T_{ij} n^i n^j$, $j_i := -T_{jk} n^j \gamma_i^k$, $S_{ij} := T_{kl} \gamma_i^k \gamma_j^l$. It is a system of evolution equations for the spatial metric γ_{ij} , the extrinsic curvature K_{ij} and equations for energy and momentum constraints. The evolution equation of the metric γ_{ij} is derived from the definition of the extrinsic curvature and the evolution equation of the extrinsic curvature is derived from the Ricci equation, an equivalent form of EFE. The Hamiltonian constraint is derived from the *Gauss-Codazzi* equation and the momentum constraint is derived from the *Codazzi-Mainardi* equation. This construction of evolution equations are by no means unique as we can always add arbitrary constraints to obtain new equations. Since the ADM formulation was later proven to be unstable in long-term numerical simulations, alternative formulations such BSSN which are more robust have been proposed. The crucial difference of BSSN from AMD is the introduction of the auxiliary variable. Beyond that, CCZ4 formulation has been presented in [89] which leads to a better behavior of the constraint equations. It combines the advantages of the conformal decomposition used in BSSN formulation and the advantages of the constraint-damped formulation.

It was shown to have better control of the constraint violations than BSSN. The derivation of CCZ4 formulation is presented in the next section.

2.4.2 The ADM version of Z4 system

The CCZ4 formalism is derived from Z4 formulation, a covariant extension of the field equations [100]:

$$R_{\mu\nu} + \nabla_\mu Z_\nu + \nabla_\nu Z_\mu = 8\pi T_{\mu\nu}, \quad (2.9)$$

where Z_μ measures the derivation from EFE, $T_{\mu\nu}$ is the stress-energy tensor. The solutions to the Einstein equations thus can be extracted from the extended solution set $\{g_{\mu\nu}, Z_\mu\}$ where $Z_\mu = 0$ according to the energy-momentum constraints. Therefore, the damping terms are added into the covariant extension of the Einstein equation in order to control the constraints, yielding the Z4 damped formalism:

$$R_{\mu\nu} + \nabla_\mu Z_\nu + \nabla_\nu Z_\mu + \kappa_1 [n_\mu Z_\nu + n_\nu Z_\mu - (1 + \kappa_2)g_{\mu\nu}n_\sigma Z^\sigma] = 8\pi \left(T_{\mu\nu} - \frac{1}{D-2}g_{\mu\nu}T \right). \quad (2.10)$$

where n_μ is the timelike unit normal to the slice and κ_1 and κ_2 are free *damping parameters*. Note that $Z^\mu = 0$ reduces (2.10) to the Einstein equations. In order to use *Gauss-Codazzi-Mainardi* equations, we need to get rid of the trace reversal of the Z4 damped formalism by Contracting (2.10) with $g^{\mu\nu}$, which gives

$$R + 2\nabla^\mu Z_\mu + \kappa_1 [2n^\mu Z_\mu + (1 + \kappa_2)Dn_\mu Z^\mu] = -\frac{16\pi T}{D-2}. \quad (2.11)$$

Recall that Bianchi identities gives

$$\nabla^a R_{ab} = \frac{1}{2}\nabla_b R. \quad (2.12)$$

The Bianchi identities leads to the following constraint-propagation system by assuming the conservation of the energy momentum,

$$\nabla^\nu \nabla_\nu Z_\mu + R_{\mu\nu} Z_\nu = -\kappa_1 \nabla^\nu [n_\mu Z_\nu + n_\nu Z_\mu + \kappa_2 g_{\mu\nu} n_\sigma Z^\sigma]. \quad (2.13)$$

where the free parameters are found to have the constraints $\kappa_1 > 0$ and $\kappa_2 > -1$ for all the constraint-related modes to be damped [101, 89].

In order to express the equations in $d+1$ language, we need to consider the decomposition of the Z4 vector Z^μ . Let us define the time and spatial projections of Z4 vector as

$$\Theta := n_\mu Z^\mu, \quad \Theta_\mu := \perp Z_\mu := \perp_\mu^\rho Z_\rho \quad \Leftrightarrow \quad Z^\mu = \Theta n^\mu + \Theta^\mu \quad (2.14)$$

where Θ is the projection of the Z_4 vector along the normal direction. Combining the results with (2.4), it is not hard to find that the components of Z_4 vector are

$$Z_\mu = (-\alpha\Theta + \beta_j\Theta^j, \Theta_i), \quad Z^\mu = \left(\frac{\Theta}{\alpha}, \Theta^i - \frac{\beta^i}{\alpha}\Theta\right). \quad (2.15)$$

The evolution equation for the spatial metric γ_{ij} remains unchanged as in the original ADM formalism. The equation for K_{ij} is derived from the projection of the Riemann tensor and the projection of the energy momentum tensor, as well as the *Gauss-Codazzi-Mainardi* equations. The evolution equation for Θ can be obtained from (2.9) and (2.11), along with the decomposition of the covariant derivative of the Z_4 vector. The equation for Θ_i is derived from (2.9) and the *Codazzi-Mainardi* equations. The ADM version of Z_4 equations is summarised as below.

$$(\partial_t - \mathcal{L}_\beta)\gamma_{ij} = -2\alpha K_{ij}, \quad (2.16)$$

$$\begin{aligned} (\partial_t - \mathcal{L}_\beta)K_{ij} = & -D_i\partial_j\alpha + \alpha \left\{ \mathcal{R}_{ij} + K_{ij}(K - 2\Theta) - 2K_{ik}K_j^k + D_i\Theta_j + D_j\Theta_i \right. \\ & \left. - \kappa_1(1 + \kappa_2)\gamma_{ij}\Theta - 8\pi \left[S_{ij} - \frac{1}{\mathcal{D}-2}\gamma_{ij}(S - \rho) \right] \right\}, \end{aligned} \quad (2.17)$$

$$\begin{aligned} (\partial_t - \mathcal{L}_\beta)\Theta = & \frac{\alpha}{2} \left\{ \mathcal{R} + K(K - 2\Theta) - K_{\mu\nu}K^{\mu\nu} - 2\gamma^{ij}\Theta_i\frac{\partial_j\alpha}{\alpha} - \kappa_1[\mathcal{D} + (\mathcal{D}-2)\kappa_2]\Theta \right. \\ & \left. + 2D^m\Theta_m - 16\pi\rho \right\}, \end{aligned} \quad (2.18)$$

$$(\partial_t - \mathcal{L}_\beta)\Theta_i = \alpha \left(D_j K_i^j - D_i K - 2K_{ij}\Theta^j + D_i\Theta - \Theta a_i - \kappa_1\Theta_i - 8\pi j_i \right). \quad (2.19)$$

This $d+1$ decomposition of the Z_4 formulation with the damping terms must be complemented with suitable gauge conditions. The $1 + \log$ slicing and Gamma-Driver shift condition are typically used to determine the coordinate system during the evolution in the numerical simulations in 4 dimensions. The choice of gauge conditions will be discussed later.

After we obtain the ADM version of the Z_4 system, conformal decomposition is applied to separate the potential singular terms in the conformal factor. Combined with the two gauge choices, it can help eliminate the need for excision. The metric

is first transformed by a *conformal factor* χ as

$$\tilde{\gamma}_{ij} := \chi \gamma_{ij} \quad \Leftrightarrow \quad \tilde{\gamma}^{ij} := \frac{1}{\chi} \gamma^{ij} \quad (2.20)$$

where the conformal factor is defined as $\chi = \gamma^{-1/d}$. The extrinsic curvature is then decomposed into its trace-free part and then transformed as

$$A_{ij} := K_{ij} - \frac{K}{d} \gamma_{ij}, \quad \tilde{A}_{ij} := \chi A_{ij} \quad \Leftrightarrow \quad K_{ij} := \frac{1}{\chi} \left(\tilde{A}_{ij} + \frac{K}{d} \gamma_{ij} \right). \quad (2.21)$$

The *auxiliary variables* are introduced as

$$\tilde{\Gamma}^i := \tilde{\gamma}^{jk} \tilde{\Gamma}_{jk}^i = \tilde{\gamma}^{ij} \tilde{\gamma}^{kl} \partial_l \tilde{\gamma}_{jk}, \quad (2.22)$$

where $\tilde{\Gamma}_{jk}^i$ is the conformal Christoffel symbol computed from $\tilde{\gamma}_{ij}$. Then, the d -dimensional Ricci tensor can be splitted into two parts:

$$\mathcal{R}_{ij} = \tilde{\mathcal{R}}_{ij} + \mathcal{R}_{ij}^\chi \quad (2.23)$$

where $\tilde{\mathcal{R}}_{ij} = \partial_k \tilde{\Gamma}_{ij}^k + \tilde{\Gamma}_{ij}^m \tilde{\Gamma}_{mk}^k - \tilde{\Gamma}_{ik}^m \tilde{\Gamma}_{mj}^k$. It is a bit lengthy to find the following expressions.

$$\tilde{\mathcal{R}}_{ij} = -\frac{1}{2} \tilde{\gamma}^{km} \partial_k \partial_m \tilde{\gamma}_{ij} + \tilde{\gamma}_{m(i} \partial_{j)} \tilde{\Gamma}^m + \tilde{\Gamma}^m \tilde{\Gamma}_{(ij)m} + \tilde{\gamma}^{mn} \left[2 \tilde{\Gamma}_{m(i}^k \tilde{\Gamma}_{j)kn} + \tilde{\Gamma}_{im}^k \tilde{\Gamma}_{kjn} \right], \quad (2.24)$$

$$\mathcal{R}_{ij}^\chi = \frac{D-3}{2\chi} \left[\tilde{D}_i \partial_j \chi - \frac{1}{2\chi} \partial_i \chi \partial_j \chi \right] + \frac{\tilde{\gamma}_{ij}}{2\chi} \left[\tilde{\gamma}^{mn} \tilde{D}_m \partial_n \chi - \frac{D-1}{2\chi} \tilde{\gamma}^{mn} \partial_m \chi \partial_n \chi \right], \quad (2.25)$$

Therefore, the evolution equations for CCZ4 system under $d+1$ decomposition can be found as the following:

$$\partial_t \chi = \beta^k \partial_k \chi + \frac{2}{d} \chi (\alpha K - \partial_k \beta^k), \quad (2.26)$$

$$\partial_t \tilde{\gamma}_{ij} = \beta^k \partial_k \tilde{\gamma}_{ij} - 2\alpha \tilde{A}_{ij} - \frac{2}{d} \tilde{\gamma}_{ij} \partial_k \beta^k + 2 \tilde{\gamma}_{k(i} \partial_{j)} \beta^k, \quad (2.27)$$

$$\begin{aligned} \partial_t \tilde{A}_{ij} = & \beta^k \partial_k \tilde{A}_{ij} + \tilde{A}_{ij} \left(\alpha (K - 2\Theta) - \frac{2}{d} \partial_k \beta^k \right) \\ & + \chi \left(-\nabla_i \nabla_j \alpha + \alpha (R_{ij} - 8\pi S_{ij} + 2 D_{(i} \Theta_{j)}) \right)^{TF} - 2\alpha \tilde{A}_i^l \tilde{A}_j^l + 2 \tilde{A}_{k(i} \partial_{j)} \beta^k \end{aligned} \quad (2.28)$$

$$\partial_t K = \beta^k \partial_k K - \nabla^i \nabla_i \alpha + \alpha \left(R + 2 \nabla_i Z^i + K(K - 2\Theta) - \kappa_1 d(1 + \kappa_2) \Theta + \frac{8\pi}{d-1} (S - d\rho) \right), \quad (2.29)$$

$$\begin{aligned} \partial_t \Theta = & \beta^k \partial_k \Theta + \frac{1}{2} \alpha \left(\mathcal{R} + 2 D_i \Theta^i - \tilde{A}_{ij} \tilde{A}^{ij} + \frac{d-1}{d} K^2 - 2\Theta K - \Theta \kappa_1 (D + \kappa_2 (d-1)) - 16\pi \rho \right) \\ & - \Theta^i \partial_i \alpha, \end{aligned} \quad (2.30)$$

$$\begin{aligned} \partial_t \hat{\Gamma}^i = & \beta^k \partial_k \hat{\Gamma}^i + \frac{2}{d} \left(\partial_k \beta^k (\tilde{\Gamma}^i + 2\kappa_3 \frac{Z^i}{\chi}) - 2\alpha \kappa_1 \frac{Z^i}{\chi} \right) + 2\tilde{\gamma}^{ij} (\alpha \partial_j \Theta - \Theta \partial_j \alpha) - 2\tilde{A}_{ij} \partial_j \alpha \\ & + \tilde{\gamma}^{jk} \partial_j \partial_k \beta^i - (\tilde{\Gamma}^j + 2\kappa_3 \frac{Z^j}{\chi}) \partial_j \beta^i - \alpha \left(\frac{2(d-1)}{d} \tilde{\gamma}^{ij} \partial_j K - d\tilde{\gamma}^{ij} \frac{\partial_j \chi}{\chi} \right) + 2\alpha \tilde{\Gamma}_{jk}^i \tilde{A}^{jk} \\ & + \frac{d-2}{d} \tilde{\gamma}^{ij} \partial_j \partial_k \beta^k - 16\pi \alpha \tilde{\gamma}^{im} j_m, \end{aligned} \quad (2.31)$$

$$\partial_t \alpha = -2\alpha(K - 2\Theta) + \beta^k \partial_k \alpha, \quad (2.32)$$

$$\partial_t \beta^i = f B^i + \beta^k \partial_k \beta^i, \quad (2.33)$$

$$\partial_t B^i = \partial_t \hat{\Gamma}^i + \beta^k \partial_k B^i - \beta^k \partial_k \hat{\Gamma}^i - \eta B^i. \quad (2.34)$$

where $\Theta := n_\mu Z^\mu = \alpha Z^0$ and $\hat{\Gamma}^i := \tilde{\Gamma}^i + 2\tilde{\gamma}^{ij} Z_j$ and Z_j is the spatial component of the Z4 vector. Noted if we set Z^μ and κ_1 to zeros, the system will reduce to the standard BSSN system. The last three equations are gauge conditions corresponding to the $1 + \log$ slicing condition and the original gamma-driver shift condition used in [96]. The generic gauge parameter f is an arbitrary positive function of α and $K_0 = K(t=0)$ as introduced in [92] and η is typically set to be $2/M$ [92, 96]. Moreover, κ_3 is introduced to stabilize the simulation and the constraints are added to the evolution equation for $\tilde{\Gamma}^i$ in CCZ4. In four-dimensional spacetimes, with f chosen to be 0.75 and κ_3 chosen to be 0.5, stable simulations of binary black holes have been obtained. It has been shown that $\kappa_1 > 0, \kappa_2 > -1$ all the constraint-related modes are damped. In our study of higher-dimensional black holes, we use a modified gamma-driver shift condition. In higher dimensional cases, the values and gradients due to the existence of the singularity could be more extreme. Hence in our code we have introduced a lower bound on α and χ so that their existences in the denominators will not cause problem. The *dynamical variables* for evolution are therefore

$$\{\chi, \tilde{\gamma}_{ij}, \tilde{A}_{ij}, K, \Theta, \hat{\Gamma}^i, \alpha, \beta^i, B^i\},$$

and so far the free parameters in the evolution equations are

$$\{\kappa_1, \kappa_2, \kappa_3, f\}.$$

Additionally, following the notations in d+1 decomposition, the *constraint violations* introduced in numerical evolution in vacuum case can be computed by

$$\mathcal{H} = {}^{(d)}R + \frac{d-1}{d}K^2 - \tilde{A}_{ij}\tilde{A}^{ij} \quad (2.35)$$

$$\mathcal{M}_i = \partial_j \tilde{A}^{ij} + \tilde{\Gamma}_{jk}^i \tilde{A}^{jk} - \frac{d-1}{d} \tilde{\gamma}^{ij} \partial_j K - \frac{d}{2} \frac{\partial_j \chi}{\chi} \tilde{A}^{ij}. \quad (2.36)$$

During the evolution, we monitor the values of both constraints and check whether they remain zero outside the horizon.

2.5 Evolving with GRChombo

In our study, we carry out simulations by using our own GRCHOMBO code, which is a new numerical relativity code designed for gravitational simulations [47, 48]. It is an open source C++ library and featured by the fully adaptive mesh refinement and the standardised output for visualisation. This section gives an introduction to the code and its main features.

2.5.1 Code design

The underlying code of GRCHOMBO is the CHOMBO code, which are developed for solving general partial differential equations with the finite difference method [49]. On top of it, GRCHOMBO specifies more common actions to GR relevant problems. Within GRCHOMBO, there are more specific examples, which contain more specific functions to work with particular problems. Provided suitable initial conditions, GRCHOMBO solves the Einstein equations of general relativity in terms of the time evolution of the metric components. It evolves the Einstein equations with the standard BSSN formalism, with an option to turn on CCZ4 constraint damping if required.

The CCZ4 system is a set of coupled PDEs with first order in time and up to second order in space. It is integrated in GRCHOMBO by discretising the time based on explicit 4th order Runge-Kutta method. The values in spatial direction are stored as cell-centred. The time intervals of the evolution depends on the resolution and the Courant factor as

$$\frac{\Delta t}{\Delta x} \leq C_{max}$$

where C_{max} is the maximum stable Courant factor. Time steps has to be small enough to ensure stable simulations. In fact, the Courant factor largely depends on

numerical experiments. In our study, we initially set C_{max} to be 0.04 and reduce it to 0.01 at the later stage of the evolution to guarantee that the time step is small enough to resolve the rapid dynamics.

2.5.2 Mesh refinement

Mesh refinement is usually required in simulations to improve the computational efficiency. There are several ways to refine the mesh in NR. For example, the moving box refinement is to increase the resolution around specified points which are moving dynamically [2, 83]. It has been particularly successful applied in simulating gravitational waveforms to provide templates for GW detections [18, 102–105]. In GRCHOMBO we use fully adaptive mesh refinement, which is more practical for the topology of the system we want to evolve. The advantage of AMR is that it can help increase the resolution in the regions which are selected by user specified criteria. There is no restrictions to the shape of the regions, i.e. the regions can be of arbitrary shape and topology.

The AMR used in GRCHOMBO is based on the mesh refinement algorithm from CHOMBO. Initially, grid points are on level 0 everywhere. The mesh can be refined by putting another level of higher solution grid with smaller spacing on the regions where require the refinement. Then, the finer level would overwrite the data of the coarse level. In GRCHOMBO, Different parts on the mesh are labeled with levels according to their resolutions and one level can only be adjacent by one level higher or lower. Each level is processing in serial. There could be more than one level evolving at the same time, but the coarser levels have to wait for the computation on the finer ones to finish.

2.5.3 Tagging Criteria

Cells are tagged before regridding happens on a given level. It has its own advantages and disadvantages. On the one hand, AMR can be applied to regions of almost arbitrary shape or size, at any point in time and anywhere is box. As a result, small emergent features of the evolving system can be captured and well-solved. It cost little unnecessary regridding. The grid spacing between levels in GRCHOMBO is 2. However, on the other hand, interpolation error can be introduced where adding one more level. Reflections at refinement boundary. Hence, we need to keep in mind that we always keep the refinement boundaries away from the regions of physical interest.

The mesh hierarchy is set up according to the tagged cells by tagging criteria. In our simulations, we used a tagging criterion based on the gradient of χ^{-1} :

$$\Delta x \frac{\sqrt{\delta^{ij} \partial_i \chi \partial_j \chi}}{\chi^2} > \sigma_\chi,$$

where Δx is the spatial grid spacing and σ_χ is the refinement threshold. In order to take derivatives at the boundary of each region, *ghost cells* are added to the edges. These ghost cells are not evolved over time, but are given certain values according to the position. If the cell is at the boundary of the computational domain, the value of it is give by the user-specified boundary conditions. If the cell is covered by another level, then it takes value from that level or from interpolation.

GRCHOMBO generates checkpoint files at regular spaces. When all the levels are synchronised, the data including the level structure will be written into a checkpoint file, so that it is easy to restart the simulation from any checkpoint file. However, sometimes it takes a large amount of time for levels to be synchronised. In order to maximise the information stored and to restart calculation at any step without information lost, GRCHOMBO stores extra coefficients to compute on any levels behind in order until all levels are synchronised again. The outputs are stored in **hdf5** files, which can be easily read and visualised by an academic visualisation software, *VisIt* ¹.

Numerical simulations of higher-dimensional black holes can be really costly. If N mesh points are needed in each dimension, the minimum computational resources required is of the scale N^D . As pointed out in [46], the corresponding computational requirements for simulations in four dimensions could be of order $\mathcal{O}(10^2)$ cores and $\mathcal{O}(10^2)$ Gb memory. With the addition of the extra dimension, it could multiple with another factor of order $\mathcal{O}(10^2)$ or more. There is impossible to solve the black string instability problems with current computer clusters. This could put a barrier for further achievements. A solution to this is to reduce the dimensions by imposing symmetries. For $SO(n)$ symmetry, this can be done by applying *Cartoon method* [45]. The modification of Cartoon is presented in [46].

¹<https://visit-dav.github.io/visit-website/>

2.6 Dimension reduction in numerical relativity

Numerical simulations can be really expensive, especially for higher dimensions where more resources are required. The cost of the numerical simulation depends on the complexity of the problem. If there are N points on each direction of the computational domain, then the complexity of the problem in D dimension can be proportional to N^D without any symmetry assumption of the problem. For code with adaptive mesh refinement, the cost grows exponentially with the number of finer levels. One way to reduce the cost is to apply dimension reduction. Fortunately, in the problem we want to solve, there are usually different symmetries. With the symmetric nature of the problem, the computation can be compressed. The most commonly seen symmetry is spherical symmetry and axial symmetry. For example, in the case of a simple Schwarzschild BH where $SO(3)$ applies. Due to the spherical symmetric of the problem, as long as we know the solution on one ray, we can deduct the full solution on the whole sphere. Therefore, the evolution of the spacetimes can be simplified from $3 + 1$ to $1 + 1$. Likewise, for an axially symmetric problem, the problem can be simplified to the revolution surface. And thus the computation can be compressed from $d + 1$ to $2 + 1$ as well. In the following sections, we will introduce how the dimension is reduced by different symmetries.

2.6.1 Dimension reduction by $SO(D - 1)$ symmetry

Let us start with a D -dimensional system with $SO(D - 1)$ symmetry. Assume it consists of a manifold \mathcal{M} with metric $g_{\mu\nu}$, where $\mu, \nu = 0, 1, \dots, d$. Consider the Cartesian coordinates system in a $(D - 1)$ -dimensional space with $SO(D - 1)$ symmetry

$$X^\mu = (t, x^1, \dots, x^{D-1}) =: (t, x^a) = (t, \mathbf{x}),$$

where $\mathbf{x} = x^a$ and a, b, c are indices ranging over $1, \dots, d$.

For a scalar function $\Phi(\mathbf{x})$ to satisfy $SO(D - 1)$ symmetry, it must satisfy $\Phi = \Phi(r)$, where $r = \sqrt{\sum (x^a)^2}$. For a vector field $\mathbf{v}(\mathbf{x})$ to satisfy $SO(D - 1)$ symmetry, it must only have components in the radial direction. It cannot have components that are orthogonal to the radial direction, because the vector field need to be invariant when it rotates along the radial direction, i.e. the line passing through the origin and \mathbf{x} . Given such a D -dimensional system, we only need to know the vector field along the half of one axis, e.g. the non-negative part of x_i axis, in the Cartesian coordinates. For a symmetric tensor $(T_{\mathbf{x}})_{ij}$ to satisfy $SO(d)$ symmetry, it must be

invariant for all rotations around the origin. If we fix \mathbf{x} then again we can rotate the system along the line passing through the origin and \mathbf{x} . After some calculation, it turns out that $(T_{\mathbf{x}})_{ij}$ is of the form $\text{diag}(b, \dots, b, a)$.

Without loss of generality, in a 3-dimensional system, we only need to know the scalar field and vector field along the half of one axis, e.g. the non-negative part of z axis, in the Cartesian coordinates, as shown in Fig. 2.2. The components of any tensor at any point in the spacetime can be obtained by rotating the data from the non-negative part of x_i axis.

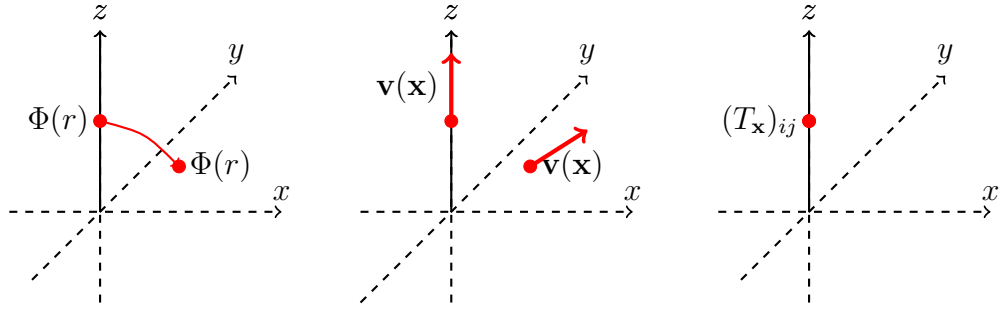


Fig. 2.2 Imposing $SO(3)$ to a scalar field $\mathbf{v}(r)$, vector field $\mathbf{v}(\mathbf{x})$ and tensor $(T_{\mathbf{x}})_{ij}$ in Cartesian coordinates.

2.6.2 Dimension reduction by $SO(D - n)$ symmetry

Now let us consider a D -dimensional spacetime with $SO(D - n)$ symmetry. Assume it consists of a manifold with metric $g_{\mu\nu}$, where $\mu, \nu = 0, 1, \dots, d - 1$. Consider the coordinate system in a $(D - 1)$ -dimensional space

$$X^A = (x^1, x^2, \dots, x^{n-1}, z, w^{n+1}, w^{n+2}, \dots, w^{D-1}) =: (x^i, z, w^a),$$

where $D - n \geq 3$ with $SO(D - n)$ symmetry in the last $D - n$ components, i.e. in (z, w^a) . Here we use capital letters A, B, C, \dots for the full dimension ranging over $1, 2, \dots, D - 1$, i, j, k, \dots for indices ranging over $1, 2, \dots, n - 1$ and a, b, c, \dots for indices ranging over $n + 1, \dots, D - 1$.

As discussed above in D -dimensional space with $SO(D)$ symmetry, the whole space can be generated by symmetry if we know the system at one single ray. Similarly, here it is sufficient to know the system on the plane satisfying $(x^i, z, 0)$ and $z \geq 0$ to generate the whole space. A vector must have the form $(x^i, z, 0)$, and a tensor

T_{AB} must have the form (2.37).

$$T_{AB} = \begin{pmatrix} T_{xx} & T_{xz} & 0 & 0 \\ T_{zx} & T_{zz} & 0 & 0 \\ 0 & 0 & T_{ww} & 0 \\ 0 & 0 & 0 & T_{ww} \end{pmatrix}. \quad (2.37)$$

For simplicity we assume it is a 4×4 matrix, as the general form will be likewise.

To compute the derivatives of these scalar, vectors and tensors are straightforward since we only need to compare points on the plane $(x^i, z, 0)$ and $z \geq 0$ and partially differentiate the expressions for the scalars, vectors and tensors on the plane. By symmetry, a scalar field satisfies $\partial_a \Psi = 0$ on the plane $(x^i, z, 0)$ and $z \geq 0$. For vectors, we have $\partial_a V^A = \delta_a^A \frac{V^z}{z}$, i.e. $\partial_a V^i = 0$ and $\partial_a V^b = \delta_a^b \frac{V^z}{z}$.

In summary, the expressions for an arbitrary scalar and its derivatives are

$$\partial_a \Psi = \partial_i \partial_a \Psi = 0, \quad \partial_a \partial_b \Psi = \delta_{ab} \frac{\partial_z \Psi}{z}. \quad (2.38)$$

The expressions for an arbitrary vector field and its derivatives are

$$V^a = \partial_i V^a = \partial_a V^i = \partial_a \partial_b V^c = 0, \quad \partial_a V^b = \delta_a^b \frac{V^z}{z} \quad (2.39)$$

$$\partial_i \partial_a V^b = \delta_a^b \left(\frac{\partial_i V^z}{z} - \delta_{iz} \frac{V^z}{z^2} \right), \quad \partial_a \partial_b V^i = \delta_{ab} \left(\frac{\partial_z V^i}{z} - \delta_z^i \frac{V^z}{z^2} \right). \quad (2.40)$$

Furthermore, the expressions for an arbitrary tensor and its derivatives are

$$T_{ia} = \partial_a T_{bc} = \partial_i \partial_a T_{bc} = \partial_a T_{ij} = \partial_i \partial_a T_{jk} = 0, \quad (2.41)$$

$$T_{ab} = \delta_{ab} T_{ww}, \quad \partial_a \partial_b T_{cd} = (\delta_{ac} \delta_{bd} + \delta_{ad} \delta_{bc}) \frac{T_{zz} - T_{ww}}{z} + \delta_{ab} \delta_{cd} \frac{\partial_z T_{ww}}{z}, \quad (2.42)$$

$$\partial_a T_{ib} = \delta_{ab} \frac{T_{iz} - \delta_{iz} T_{ww}}{z} \quad (2.43)$$

$$\partial_i \partial_a T_{ib} = \delta_{ab} \left(\partial_i \frac{T_{jz} - \delta_{jz} \partial_i T_{ww}}{z} - \delta_{iz} \frac{T_{jz} - \delta_{jz} T_{ww}}{z^2} \right). \quad (2.44)$$

$$\partial_a \partial_b T_{ib} = \delta_{ab} \left(\frac{\partial_z T_{ij}}{z} - \frac{\delta_{iz} T_{jz} + \delta_{jz} T_{iz} - 2\delta_{iz} \delta_{jz} T_{ww}}{z^2} \right). \quad (2.45)$$

We apply the above expressions to the problem of black string which has $SO(3)$ symmetry. Then the $3 + 1$ dimensionality of the problem can be reduced to $1 + 1$ dimension. In the evolution we have Cartesian coordinates (t, x, z, w) so that we

only need to solve the problem in $x - z$ plane. We use the Cartoon expressions for derivatives from the last section to derive the dimension reduction version of the CCZ4 equations. In our code, the CCZ4 equations have been modified to include the extra symmetry reduction terms. As an example, the spatial derivative term $\partial_k \beta^k$ becomes $\partial_I \beta^I + N \frac{\beta^z}{z}$, where I runs over the simulated spatial dimensions, i.e. $I = 1, 2, \dots, n$ and N is the number of the rest spatial dimensions, i.e. $N = D - n - 1$. The additional term to the evolution equation of the conformal factor comes from the spatial derivative term $\partial_k \beta^k$. As a results, the evolution equation is modified to

$$\partial_t \chi = \beta^I \partial_I \chi + \frac{2}{d} \chi (\alpha K - \partial_I \beta^I - N \frac{\beta^z}{z}), \quad (2.46)$$

The full list of the additional terms added to the right hand side of the CCZ4 equations can be found in [Appendix A](#).

Chapter 3

Analysis Methods for Higher Dimensional Black Holes

Most studies of black holes have restricted their focus to four dimensions, i.e. 3+1 dimensions. It is indeed intuitive to think that the world we live in has four dimensions. However, the form that the EFE takes makes it possible to be generalised to arbitrary number of dimensions. This makes people wonder whether the properties of black hole solutions in four dimensions are characteristics in general or they are just results of four dimensions. Back to 1920s, Kaluza and Klein first attempted to unify general relativity and electromagnetism [31, 32]. More recently, increasing interests have also risen on black holes in higher dimensions from the development of other theories in the field. For example, ideas from brane-world suggest that our familiar three spatial dimensions might just be a surface of a higher-dimensional space. Black holes extended into the extra dimensions forms the point of view that gravity is higher dimensional in these theories. Furthermore, on the way to find a quantum theory of gravity, string theory predicts that there are more than four dimensions for spacetime. It incorporates the idea that extra dimensions are curled up into a small ball from the older ideas of unification. Therefore, higher-dimensional black holes must be considered in string theory. Furthermore, gauge/gravity duality, merged from string theory, relates certain strongly coupled non-gravitational theories to higher-dimensional theories with gravity [106–108]. Under this duality thermal equilibrium in some $(3+1)$ -dimensional non-gravitational systems is described by a higher-dimensional black hole. In addition, the study of the GL instability and its possible endpoints, together with the discovery of the

asymptotically flat black ring in five dimensions were largely responsible for the intrinsic interest in understanding the physics of higher dimensional black holes.

This chapter begins with an overview of black holes in higher dimensions in Sec. 3.1. Then it presents the numerical methods and techniques designed for simulations of higher dimensional BHs. Sec. 3.3 introduces the numerical methods for finding the apparent horizon. Sec. 3.4 and Sec. 3.5 present the embedding diagram and curvature invariant that we track during the evolution. Black hole thermodynamics are introduced in Sec. 3.6.

3.1 Black holes in higher dimensions

In higher dimensions, black holes could have much richer characteristics. They are not necessary to be spherical and stable, or uniquely determined by mass and angular momentum as they are in four dimensions. In 4+1 dimensions, we have the asymptotic solutions, such as Myers-Perry S^3 and black rings [109, 110]. Multi-black holes also exist, such as black Saturn [111]. For 4+1 dimensions, there is a failure of rigidity, which implies there exist multiple explicit families of stationary, asymptotically flat black hole solutions. Some of them has analogue in 3+1 dimensions, such as Schwarzschild solution and Myers-Perry solution. The latter is the high-dimensional analogue of the Kerr family of BH [10]. Some of them are dynamically unstable to gravitational waves. The rest of this section will focus more on vacuum solutions in KK theory. Without loss of generality, let us start with black hole solutions in five dimensions, i.e. the usual four dimensions plus one extra spatial dimension.

The vacuum EFE in four dimensions is simply

$$R_{ab} = 0, \quad (3.1)$$

where $a, b = 0, 1, 2, 3$. The only possible solution to it in four dimensions must be spherically symmetric. The Schwarzschild solution, one of the simplest solutions to EFE, has the following form

$$ds^2 = -f(r)dt^2 + f(r)^{-1}dr^2 + r^2d\Omega_2^2, \quad f(r) = 1 - \frac{2M}{r}. \quad (3.2)$$

where $r = 2M$ is the Schwarzschild radius.

To extend to higher dimensions, we usually assume the extra dimensions to be spatial. In higher dimensions, we just need to solve the same equations,

$$R_{\mu\nu} = 0. \quad (3.3)$$

where $\mu, \nu = 0, 1, 2, \dots, d$, and d is the number of spatial dimensions.

We first consider adding one extra dimension. Starting from the Schwarzschild solution, there are a few ways to add the extra dimension. By treating the extra dimension the same as the usual three space dimensions, we obtain the hyperspherically symmetric solution in five dimensions,

$$ds^2 = -f_4(r)dt^2 + f_4(r)^{-1}dr^2 + r^2d\Omega_3^2, \quad f_4(r) = 1 - \frac{r_h^2}{r^2}. \quad (3.4)$$

where r_h is the Schwarzschild radius.

3.1.1 The Schwarzschild-Tangherlini solution

A simple generalisation of the Schwarzschild solution into D dimensions gives rise to a hyperspherically symmetric solution:

$$ds^2 = -f_d(r)dt^2 + f_d(r)^{-1}dr^2 + r^2d\Omega_{d-1}^2, \quad f_d(r) = 1 - \left(\frac{r_h}{r}\right)^{d-2}. \quad (3.5)$$

where r_h is the Schwarzschild radius, $f_d(r)$ is the generalisation of the four-dimensional Schwarzschild potential and $d\Omega_{d-1}^2$ is the line element of the d -dimensional unit sphere. The numerical study for five-dimensional Schwarzschild solution has been done in [112] by using BSSN formulation.

3.1.2 The Black string solution

Another simple solution can be obtained by adding one extra dimension to the Schwarzschild solution, assuming the components corresponding to the extra dimension of the Riemann tensor are zeros. This solution is known as the black string. The black string solution is obtained by extending the 4-dimensional Schwarzschild solution into the extra dimension in a uniform way, assuming that the Riemann tensor does not depend on the extra dimension. It is distinguished from the five-dimensional Schwarzschild solution (which has a hyperspherical symmetry) that

the black string solution takes the following form

$$ds^2 = - \left(1 - \frac{2M}{r}\right) dt^2 + \left(1 - \frac{2M}{r}\right)^{-1} dr^2 + r^2 d\Omega_2^2 + dx^2, \quad (3.6)$$

where M is the total mass in units, r is the radial coordinate, x is the extra dimension corresponding to a coordinate on an S^1 and $d\Omega_2^2$ is the standard metric on a unit radius 2-sphere. If the extra dimension is compact with length L , the black string has finite mass and corresponds to the basic Kaluza-Klein black hole. Black holes in four dimensions are unique and are always spherical. However, in higher dimensions they can have totally different horizon topology. While the generalised Schwarzschild solution has spherical horizon, black string has a cylindrical horizon. It is much less constrained so that some stationary black holes can be unstable, leading to interesting dynamics.

If the extra dimension is compact with length L , the black string will have finite mass, corresponding to the basic Kaluza-Klein black hole. When introducing a small perturbation in the x direction (string-like direction), the black string are proven to be unstable [33]. This instability results in a pinch-off of the horizon in finite time and produces a singularity that is visible from infinity, i.e. a naked singularity. This phenomenon has only been discovered in higher dimension, while in four dimensions, evidence suggests that a naked singularity are not likely to form generically although it has not been fully proven yet. If the mass of such BH increases further and it no longer fit in the extra dimension, we can obtain caged BHs [33].

Generalised to arbitrary D dimensions, the black string solution has the line element:

$$ds^2 = - \left(1 - \frac{2m}{r^{d-3}}\right) dt^2 + \left(1 - \frac{2m}{r^{d-3}}\right)^{-1} dr^2 + r^2 d\Omega_{d-2}^2 + dx^2, \quad (3.7)$$

where $d = D - 1$, m is a constant that fixes the black hole mass, and Ω_{d-2}^2 denotes the line element of the unit $(d-2)$ -sphere. The first three terms form the generalised d -dimensional Schwarzschild solution. Black hole dynamics can be really different in higher dimensional settings. In our study we focus on the five-dimensional black string with the extra dimension of compact length.

3.2 Initial conditions

In this section, we introduce the initial conditions of the black hole spacetime to evolve with CCZ4 formalism without excising any region from the computational domain.

3.2.1 The Schwarzschild-Tangherlini solution

For the D -dimensional Schwarzschild solution, the isotropic metric is typically used as the initial conditions for its spacetime evolution. The isotropic coordinates were adopted to deal with the coordinate singularity at 0 (in the non-string like coordinate). Let $r = \rho(1 + \frac{m}{2\rho^{D-3}})^{\frac{2}{D-3}}$. Then the metric becomes

$$ds^2 = - \left(1 - \frac{2m}{\rho^{D-3}(1 + \frac{m}{2\rho^{D-3}})^2} \right) dt^2 + \left(1 + \frac{m}{2\rho^{D-3}} \right)^{\frac{4}{D-3}} (dx^2 + dy^2 + dz^2).$$

Compared with $(d+1)$ -decomposition of spacetime, the spatial metric γ_{ij} is an $d \times d$ matrix:

$$\gamma_{ij} = \begin{pmatrix} (1 + \frac{m}{2\rho^{D-3}})^{\frac{4}{D-3}} & 0 & 0 \\ 0 & \ddots & 0 \\ 0 & 0 & (1 + \frac{m}{2\rho^{D-3}})^{\frac{4}{D-3}} \end{pmatrix}. \quad (3.8)$$

Let $\chi = \gamma^{-1/d} = (1 + \frac{m}{2\rho^{D-3}})^{-\frac{4}{D-3}}$. The *conformal metric* $\tilde{\gamma}_{ij}$ is therefore

$$\tilde{\gamma}_{ij} = \begin{pmatrix} 1 & 0 & 0 & 0 \\ 0 & 1 & 0 & 0 \\ 0 & 0 & \ddots & 0 \\ 0 & 0 & 0 & 1 \end{pmatrix}. \quad (3.9)$$

With this initial condition, the black hole spacetime can be evolved by CCZ4 formalism without excising any region from the computational domain.

3.2.2 The black string solution

For black strings, one naturally would first think of writing it in isotropic coordinates. Because of this extra dimension here, the coordinates is cannot be exactly isotropic. We can only call it isotropic-like coordinates.

$$ds^2 = -\left(1 - \frac{2m}{r}\right)dt^2 + 2\sqrt{\frac{2m}{r}}dtdr + dr^2 + r^2d\Omega_2^2 + dx^2. \quad (3.10)$$

However, due to the compact extra direction, we find that the conformal factor cannot fully absorb the singularity from the metric. No matter how we write the conformal factor, there is still singular terms in the spatial metric. There are two ways to deal with the singularity. One is turducken and the other is excision. With turducken method, we smooth out the quantities around the singularity. With excision, we first need to locate the horizon and then excise a small region inside the horizon, which covers the singularity, with suitable boundary condition. In practice we are not able to achieve stable simulations with this coordinates. Moreover implementing excision would lose the point of using CCZ4. We hope by using CCZ4 we can evolve the whole domain with out excision. To achieve this, we need horizon-penetrating coordinates.

Therefore, for black string evolution, we instead consider *Gullstrand–Painlevé coordinates* (GP coordinates) in four dimensions plus one extra dimension:

$$ds^2 = -\left(1 - \frac{2m}{r}\right)dt^2 + 2\sqrt{\frac{2m}{r}}dtdr + dr^2 + r^2d\Omega_2^2 + dx^2. \quad (3.11)$$

As we can see, the spatial dimensions are totally isotropic. Re-writing it in Cartesian coordinates and comparing with the d+1 decomposition gives:

$$ds^2 = -\left(1 - \frac{2m}{r}\right)dt^2 + 2\sqrt{\frac{2m}{r^3}}ydt dy + 2\sqrt{\frac{2m}{r^3}}zdt dz + 2\sqrt{\frac{2m}{r^3}}wdt dw + dx^2 + dy^2 + dz^2 + dw^2 \quad (3.12)$$

where r is supposed as $\sqrt{y^2 + z^2 + w^2}$.

We find $\alpha = 1$ and $\beta_a = \beta^a = (0, \sqrt{\frac{2m}{r^3}}y, \sqrt{\frac{2m}{r^3}}z, \sqrt{\frac{2m}{r^3}}w)$. The *conformal factor* is just 1 and the *conformal metric* is simply an 4×4 identity matrix, i.e.

$$\chi = 1, \quad \tilde{\gamma}_{ij} = \begin{pmatrix} 1 & 0 & 0 & 0 \\ 0 & 1 & 0 & 0 \\ 0 & 0 & 1 & 0 \\ 0 & 0 & 0 & 1 \end{pmatrix}.$$

In GP coordinates, $\tilde{\Gamma}^i$ is also found to be trivial. The only non-trivial parts contain in the extrinsic curvature K_{ij} . A_{ij} is found to be

$$\begin{pmatrix} -\frac{3\sqrt{\frac{m}{r}}}{4\sqrt{2}r} & 0 & 0 & 0 \\ 0 & \frac{\sqrt{\frac{m}{r}}(5w^2-7y^2+5z^2)}{4\sqrt{2}r^3} & -\frac{3\sqrt{\frac{m}{r}}yz}{\sqrt{2}r^3} & -\frac{3\sqrt{\frac{m}{r}}wy}{\sqrt{2}r^3} \\ 0 & -\frac{3\sqrt{\frac{m}{r}}yz}{\sqrt{2}r^3} & \frac{\sqrt{\frac{m}{r}}(5w^2+5y^2-7z^2)}{4\sqrt{2}r^3} & -\frac{3\sqrt{\frac{m}{r}}wz}{\sqrt{2}r^3} \\ 0 & -\frac{3\sqrt{\frac{m}{r}}wy}{\sqrt{2}r^3} & -\frac{3\sqrt{\frac{m}{r}}wz}{\sqrt{2}r^3} & \frac{\sqrt{\frac{m}{r}}(-7w^2+5y^2+5z^2)}{4\sqrt{2}r^3} \end{pmatrix}. \quad (3.13)$$

One advantage of using GP coordinate is that the spatial metric γ_{ij} and conformal factor now become non-singular and the four spatial dimensions are treated equally. In addition, the perturbation can be added to the conformal factor, while the other terms remained unchanged. This can make it easy to construct the perturbed initial data and minimise the initial constraint violations. In isotropic-Schwarzschild coordinates, the extrinsic curvature is just zero. In GP coordinates the non-trivial terms contain in the extrinsic curvature. It becomes singular when r goes to 0. The initial data is regularised by turducken method as introduced in [113, 114].

3.3 Apparent Horizon

Being able to achieve stable evolution of the black string spacetime is not enough for us to locate where the black string is and understand the dynamics of the horizon. *Apparent horizon* (AH) is defined locally as the outmost surface on a spacial hypersurface such that the expansion of outgoing null geodesic is zero. It can be found on each spatial hypersurface during the evolution. Thus, it can be used as an ideal indicator of the existence and location of an evolving black hole. In some numerical approaches such as the GH coordinates where singularity excision is needed, locating the apparent horizon is essential.

3.3.1 Introduction

To find the apparent horizon, we need to derive the equation that characterises it. In a $(D-1)$ dimensional spatial hypersurface Σ , the apparent horizon is a $(D-2)$ dimensional surface S immersed in it. Let \vec{s} denotes the outwards unit normal vector to S , and \vec{n} be the future-pointing unit normal to Σ . Therefore, the induced metric $h_{\mu\nu}$ on the $(D-2)$ dimensional surface S can be written as

$$h_{\mu\nu} = g_{\mu\nu} + n_\mu n_\nu - s_\mu s_\nu \quad (3.14)$$

Then, the outgoing null vector \vec{l} can be constructed as

$$\vec{l} = \vec{n} + \vec{s} \quad (3.15)$$

The expansion H of the outgoing null geodesic is defined as

$$H = -\frac{1}{2}h^{\mu\nu}\mathcal{L}_{\vec{l}}h_{\mu\nu} = -\frac{1}{2}h^{\mu\nu}(\mathcal{L}_{\vec{n}}h_{\mu\nu} + \mathcal{L}_{\vec{s}}h_{\mu\nu}) \quad (3.16)$$

By definition, the extrinsic curvature $X_{\mu\nu}$ of the $(D-2)$ dimensional surface S is $X_{\mu\nu} = -\frac{1}{2}\mathcal{L}_{\vec{s}}h_{\mu\nu}$, and the extrinsic curvature $K_{\mu\nu}$ of Σ is $K_{\mu\nu} = -\frac{1}{2}\mathcal{L}_{\vec{n}}g_{\mu\nu}$, the expansion is then

$$\begin{aligned} H &= -\frac{1}{2}h^{\mu\nu}(\mathcal{L}_{\vec{n}}h_{\mu\nu} + \mathcal{L}_{\vec{s}}(g_{\mu\nu} + n_{\mu}n_{\nu} - s_{\mu}s_{\nu})) \\ &= -\frac{1}{2}h^{\mu\nu}\mathcal{L}_{\vec{n}}h_{\mu\nu} - \frac{1}{2}h^{\mu\nu}\mathcal{L}_{\vec{s}}g_{\mu\nu} - \frac{1}{2}h^{\mu\nu}\mathcal{L}_{\vec{s}}n_{\mu}n_{\nu} + \frac{1}{2}h^{\mu\nu}\mathcal{L}_{\vec{s}}s_{\mu}s_{\nu} \end{aligned} \quad (3.17)$$

Here, the last two terms are both zeros due to the fact that $n_{\mu}n^{\mu} = -1$, $s_{\mu}s^{\mu} = 1$ and $s_{\mu}n^{\mu} = 0$. Hence,

$$H = -D_ms^m + K - K_{mn}s^ms^n = -(\gamma^{mn} - s^ms^n)(D_ms_n - K_{mn}) \quad (3.18)$$

where $X = -D_ms^m$, D is the $(D-1)$ dimensional covariant derivative in Σ , X and K are the traces of $X_{\mu\nu}$ and $K_{\mu\nu}$.

For convenience, the apparent horizon is parameterised as a level set of some scalar function F such that:

$$F(x^i) = 0. \quad (3.19)$$

Then the unit normal vector s^i can be written as

$$s^i = \frac{D^i F}{u}, \quad (3.20)$$

where $u := |DF| = (\gamma^{mn}D_m F D_n F)^{1/2}$. Substituting this into the expansion equation (3.18).

$$H = -(\gamma^{mn} - \frac{D^m F D^n F}{u^2})(\frac{D_m D_n F}{u} - K_{mn}) = 0. \quad (3.21)$$

In the case of black string spacetime and the dynamical variables of the evolution, we need to work out the equation in Cartesian coordinates, where the apparent

horizon can be parameterised as a level set of some scalar function F :

$$F(x, y) = y - h(x). \quad (3.22)$$

This is by no means the general parameterisation, but it has been typically used as a simplification when finding apparent horizons. This means apparent horizon with very complicated form will not be found. According to the results from both theoretical analysis [33] and numerical work [3], the horizon should be well-defined by such function.

Therefore, the expansion becomes

$$\begin{aligned} H &= -D_m \left(\frac{\partial^m F}{u} \right) + K - \frac{1}{u^2} \partial^m F \partial^n F K_{mn} \\ &= -\partial_m \left(\frac{\partial^m F}{u} \right) - \Gamma_{mn}^m \frac{\partial^n F}{u} + K - \frac{1}{u^2} \partial^m F \partial^n F K_{mn} \\ &= -\frac{\partial_m \partial^m F}{u} + \frac{\partial^m F \partial^n F \partial_m \partial_n F}{u^3} + \frac{\partial^m F \partial_n F \partial_k F \partial_m \gamma^{kn}}{2u^3} - \frac{1}{2} \gamma^{mk} \partial_n \gamma_{mk} \frac{\partial^n F}{u} \end{aligned} \quad (3.23)$$

$$+ K - \frac{\partial^m F \partial^n F}{u^2} K_{mn} \quad (3.24)$$

According to modified Cartoon method [46], for $i, j = x, y, a, b, c = z, w$

$$\begin{aligned} \partial_a \partial^a F &= \delta_a^a \frac{\partial_y F}{y} = (D-3) \frac{\partial_y F}{y}, \quad \partial_a F = \partial_a \partial_i F = 0, \\ \gamma_{ia} &= \partial_a \gamma_{bc} = \partial_a \gamma_{ij} = 0, \quad \gamma_{ab} = \delta_{ab} \gamma_{ww}. \end{aligned} \quad (3.25)$$

Hence, the expansion can be written as

$$H = -\frac{\partial_i \partial^i F}{u} - (D-3) \frac{\partial_y F}{yu} + \frac{\partial^i F \partial^j F \partial_i \partial_j F}{u^3} + \frac{\partial^i F \partial_j F \partial_k F \partial_i \gamma^{kj}}{2u^3} \quad (3.26)$$

$$- \frac{\partial^i F}{2u} \left(\gamma^{jk} \partial_i \gamma_{jk} + (D-3) \partial_i \ln \gamma_{ww} \right) + K - \frac{\partial^i F \partial^j F}{u^2} K_{ij} \quad (3.27)$$

By the definition of having an apparent horizon, we set $H = 0$.

3.3.2 Numerical methods

In the previous study by Lehner and Pretorius [3], they have used *flow* method to find the apparent horizon numerically. They restricted their research on simply

connected apparent horizons that are periodic in the string direction x , which means such an apparent horizon can be described by a function $R(x)$.

3.3.3 Flow method

In order to implement flow method, let us define the level surface $F = 0$ of the function

$$F(x, y) = y - R(x).$$

By constructing the outgoing null geodesic \vec{l} and the expansion H , they solved the equation of zero expansion, i.e. $H = 0$, by point-wise relaxation method (or flow method) to determine $R(x)$. Given an initial guess $R_0(x)$ for the unknown function $R(x)$, then keep iterating the following equation until the norm of the expansion function is below some desired threshold (in our runs we have typically set it to $10^{-3}h$, where h is the basic scale of discretization):

$$\Delta R_n(x) := R_{n+1}(x) - R_n(x) = -H(x)\Delta\tau, \quad (3.28)$$

where $R_n(z)$ is the solution after the n^{th} iteration.

Given suitable initial conditions, the solution $R_n(x)$ will flow to the true solution, i.e. the apparent horizon. If $R_n(x)$ is outside the apparent horizon, the expansion H will be positive so that the value of $R_{n+1}(x)$ will be reduced according to (3.28). On the other hand, if $R_n(x)$ is inside the apparent horizon, the expansion H will be negative so that the value of $R_{n+1}(x)$ will be increasing.

We have the flow method implemented in *Mathematica*. According to [3], the apparent horizon finder will become extremely time-consuming at the later time of evolution due to thousands of iterations are needed for unstable black string. In consideration of this, we write a new code with Newton-Raphson method to find the apparent horizon more efficiently.

3.3.4 Newton-Raphson method

Newton-Raphson method is a root-finding algorithm which successively produces better approximations to the roots. Given an initial guess x_0 that is close to the root of a function $g(x)$, then it generates a better approximation by computing the x intercept of its tangent. That is, x_1 will be obtained by $x_1 = x_0 - g(x_0)/g'(x_1)$.

The process will be repeated by

$$x_{n+1} = x_n - \frac{g(x_n)}{g'(x_n)}, \quad (3.29)$$

until it finds an approximation that is close enough to the root. Given appropriate initial guess that is close enough to the unknown solution, this method usually has a quadratic convergence. Generalised to higher dimensions, to find the zeros for a function g on \mathbb{R}^n , we repeat the iteration process by

$$\mathbf{x}_{n+1} = \mathbf{x}_n - [\mathbf{J}(\mathbf{x}_n)]^{-1} g(\mathbf{x}_n), \quad (3.30)$$

where $x \in \mathbb{R}^n$ and $\mathbf{J}(\mathbf{x}_n)$ is the Jacobian matrix. Given a differential equation $D(\mathbf{x}, g(\mathbf{x}), \partial g(\mathbf{x}), \dots)$. A better approximation can be obtained by

$$g_{n+1}(\mathbf{x}) = g_n(\mathbf{x}) - [D'(\mathbf{x}, g(\mathbf{x}), \partial g(\mathbf{x}), \dots)]^{-1} D(\mathbf{x}, g(\mathbf{x}), \partial g(\mathbf{x}), \dots). \quad (3.31)$$

Therefore, it can be written as

$$D'(\mathbf{x}, g(\mathbf{x}), \partial g(\mathbf{x}), \dots) \delta g_n = -D(\mathbf{x}, g(\mathbf{x}), \partial g(\mathbf{x}), \dots), \quad (3.32)$$

where $\delta g_n = g_{n+1}(\mathbf{x}) - g_n(\mathbf{x})$.

In order to use Newton-Raphson method, we need to derive the equation of the second derivative of h . Substituting these definitions into (3.21), the non-linear second order differential equation for h can be obtained as

$$\frac{d^2 h}{dx^2} = \frac{-1}{\gamma^{xx}\gamma^{yy} - (\gamma^{xy})^2} \left(u^2 \gamma^{mn} - \partial^m F \partial^n F \right) \left(\Gamma_{mn}^k \partial_k F + u K_{mn} \right) \quad (3.33)$$

where $u = (\gamma^{mn} D_m F D_n F)^{1/2}$, thus $u^2 = \gamma^{xx} \left(\frac{dh}{dx} \right)^2 - 2\gamma^{xy} \frac{dh}{dx} + \gamma^{yy}$, and

$$\partial_i F = \left(-\frac{dh}{dx}, 1, 0, 0 \right), \quad \partial^i F = \gamma^{ij} \partial_j F = -\gamma^{xx} \frac{dh}{dx} + \gamma^{xy}$$

Substituting the definitions of $\partial_i F$ and $\partial^i F$, and after some algebra, by the definition of having the apparent horizon, i.e. setting $H = 0$, it gives

$$\frac{d^2 h}{dx^2} = \frac{-1}{\gamma^{xx}\gamma^{yy} - (\gamma^{xy})^2} \left(u^2 \gamma^{mn} \Gamma_{mn}^k \partial_k F + u^3 \gamma^{mn} K_{mn} - \partial^m F \partial^n F \Gamma_{mn}^k \partial_k F - u \partial^m F \partial^n F K_{mn} \right).$$

In terms of dynamical variables $\{\chi, \tilde{\gamma}_{ij}, \tilde{A}_{ij}, K, \Theta, \hat{\Gamma}^i\}$, the equation becomes

$$\frac{d^2 h}{dx^2} = \frac{-1}{\chi^2(\tilde{\gamma}^{xx}\tilde{\gamma}^{yy} - (\tilde{\gamma}^{xy})^2)} \left(u^2 \partial_k F (\chi \tilde{\Gamma}^k + \frac{D-3}{2} \tilde{\gamma}^{kj} \partial_j \chi) + u^3 (\tilde{\gamma}^{mn} \tilde{A}_{mn} + K) \right. \\ \left. - \partial^m F \partial^n F \partial_k F (\tilde{\Gamma}_{mn}^k - \frac{1}{2\chi} (\delta_n^k \partial_m \chi + \delta_m^k \partial_n \chi - \tilde{\gamma}_{mn} \tilde{\gamma}^{ki} \partial_i \chi)) - u \partial^m F \partial^n F \frac{1}{\chi} (\tilde{A}_{mn} + \frac{1}{D-1} \tilde{\gamma}_{mn} K) \right)$$

where $\tilde{\Gamma}_{mn}^k = \frac{1}{2} \tilde{\gamma}^{kl} (\partial_n \tilde{\gamma}_{lm} + \partial_m \tilde{\gamma}_{ln} - \partial_l \tilde{\gamma}_{mn})$.

According to modified Cartoon method, in the case of $SO(D-d)$ symmetry, the expressions for a scalar, vector and tensor Ψ, V^a, T_{ab} are

$$0 = \partial_a \Psi, 0 = V^a = \partial_i V^a = \partial_a V^i, 0 = T_{ia} = \partial_a T_{bc} = \partial_a T_{ij}$$

$$T_{ab} = \delta_{ab} T_{ww}, \partial_a T_{ib} = \delta_{ab} \frac{T_{iz} - \delta_{iz} T_{ww}}{z}$$

where $a, b = d+1, \dots, D-1$ and $i, j = 1, \dots, d$.

Hence the equation becomes,

$$\frac{d^2 h}{dx^2} = \frac{-1}{\chi^2(\tilde{\gamma}^{xx}\tilde{\gamma}^{yy} - (\tilde{\gamma}^{xy})^2)} \left(u^2 \partial_k F (\chi \tilde{\Gamma}^k + \frac{D-3}{2} \partial_l \chi \tilde{\gamma}^{kl}) + u^3 (\tilde{\gamma}^{mn} \tilde{A}_{mn} + (D-3) \tilde{\gamma}^{ww} \tilde{A}_{ww} \right. \\ \left. + K) - \partial^m F \partial^n F \partial_k F (\frac{1}{2} \tilde{\gamma}^{kl} (\partial_n \tilde{\gamma}_{lm} + \partial_m \tilde{\gamma}_{ln} - \partial_l \tilde{\gamma}_{mn})) \right. \\ \left. - \frac{1}{2\chi} (\delta_n^k \partial_m \chi + \delta_m^k \partial_n \chi - \tilde{\gamma}_{mn} \tilde{\gamma}^{kl} \partial_l \chi) - u \partial^m F \partial^n F \frac{1}{\chi} (\tilde{A}_{mn} + \frac{1}{D-1} \tilde{\gamma}_{mn} K) \right)$$

where $k, l, m, n = x, y$.

$$\frac{d^2 h}{dx^2} = \frac{-1}{\chi^2 \det \tilde{\gamma}^{xy}} \left(\chi D^2 F \partial_k F \tilde{\Gamma}^k + \chi \frac{D-3}{2} D^2 F \partial^m F \partial_m \ln \chi + (D^2 F)^{3/2} K \right. \\ \left. - \partial^m F \partial^n F \partial^l F \frac{1}{\chi} (\partial_n \tilde{\gamma}_{lm} - \frac{1}{2} \partial_l \tilde{\gamma}_{mn}) - D^2 F \partial^m F (\partial_m \ln \chi - \frac{1}{2} \partial_m \ln \chi) \right. \\ \left. - (D^2 F)^{1/2} \partial^m F \partial^n F \frac{1}{\chi} (\tilde{A}_{mn} + \frac{1}{D-1} \tilde{\gamma}_{mn} K) \right)$$

where $k, l, m, n = x, y$ and $D^2 F = \partial_k \partial^k F$.

$$\frac{d^2 h}{dx^2} = \frac{-1}{\det \tilde{\gamma}^{xy}} \left(D^2 F (\frac{1}{\chi} \partial_k F \tilde{\Gamma}^k + \frac{1}{\chi^2} \frac{D-2}{2} \partial^m F \partial_m \ln \chi) - \frac{1}{\chi} \frac{D-2}{D-1} (D^2 F)^{3/2} K \right)$$

$$- \partial^m F \partial^n F \partial^l F \frac{1}{2\chi^3} \partial_l \tilde{\gamma}_{mn} + (D^2 F)^{1/2} \partial^m F \partial^n F \frac{1}{\chi^3} \tilde{A}_{mn} \Big) \quad (3.34)$$

where $k, l, m, n = x, y$ and $D^2 F = \partial_k \partial^k F$.

The equations are implemented in the code and are solved by PETSc libraries [115]. At the beginning of the evolution, we use the solution of the uniform black string as the initial guess for the AH of the initial slightly-perturbed string. During the evolution, we typically use the previous solution as the initial guess for finding the AH at every full time step of the coarsest level. In later stage of the evolution when there are rapid dynamics, we had to keep the time step small enough so that the AH can be tracked.

3.4 Embedding diagram

To obtain some intuitive idea about the shape of the AH during the evolution, we define the embedding diagram of the horizon. After we solve the equation for the zero expansion, the embedding diagram can be found as following. The metric can be written in terms of the dynamical variables as,

$$ds_H^2 = \tilde{\gamma}_{zz} dz^2 + 2\tilde{\gamma}_{zx} dz dx + \tilde{\gamma}_{xx} dx^2 + \tilde{\gamma}_{ww} z^2 dw^2 \quad (3.35)$$

where w denotes any of the Cartesian cartoon directions along the S^2 .

By the definition of the apparent horizon $x = h(z)$, we can write $\tilde{\gamma}_{zz} = \tilde{\gamma}_{zz}(y, h(z))$. Substituting back into (3.35) gives

$$ds_H^2 = (\tilde{\gamma}_{zz} + 2\tilde{\gamma}_{zx} h'(z) + \tilde{\gamma}_{xx} h'(z)^2) dz^2 + \tilde{\gamma}_{ww} z^2 dw^2. \quad (3.36)$$

Since in flat space, it can be written as

$$ds_H^2 = dR^2 + dZ^2 + R^2 d\Omega_{(2)}^2 \quad (3.37)$$

where $Z = Z(z)$ and $R = R(z)$. As a result,

$$ds_H^2 = (R'^2 + Z'^2) dz^2 + R^2 d\Omega_{(2)}^2, \quad (3.38)$$

Comparing it with (3.36), it is not hard to find that

$$R(z) = \sqrt{\tilde{\gamma}_{ww}} h(z). \quad (3.39)$$

For the embedding diagram, coordinate R is the areal radius $R(z) = \sqrt{\tilde{\gamma}_{ww}}h(z)$, and coordinate Z is defined to satisfy that the proper length in the string direction z is the same as the Euclidean length of $R(Z)$ in the embedding diagram, i.e.

$$Z(z) = \int_0^z d\bar{z} \frac{\sqrt{\tilde{\gamma}_{zz} + 2\tilde{\gamma}_{zx}h'(\bar{z}) + \tilde{\gamma}_{xx}h'(\bar{z})^2}}{\sqrt{h'(\bar{z})^2 + 1}}. \quad (3.40)$$

3.5 Curvature invariant

The Kretschmann scalar is invariant for different coordinates. It is an important quantity to verify whether the spacetimes contains a real singularity. The Kretschmann should be finite. If there is a singularity, the Kretschmann scalar is not defined there. The Kretschmann scalar is defined as

$$\bar{\mathcal{K}}_s = {}^{(D)}R_{abcd} {}^{(D)}R^{abcd}, \quad (3.41)$$

where R_{abcd} is Riemann curvature tensor. It can be obtained by calculating the "square" of the Riemann curvature tensor. It is useful to normalize it as the induced Kretschmann invariant as

$$\bar{\mathcal{K}}_s = \frac{1}{12} R_{abcd} R^{abcd} R_{\text{AH}}^4. \quad (3.42)$$

where R_{AH} is the areal radius of the string. The invariant kretschmann evaluates to be 1 for an exact black string, and 6 for an asymptotically flat 5D Schwarzschild black hole.

3.6 Black hole thermodynamics

The other quantities that are useful to monitor the dynamics of the system are the mass and the horizon area.

The mass of a 5D BH is

$$M_{bh} = \frac{3\pi r_5^2}{8}, \quad (3.43)$$

and its horizon area is

$$A_{bh} = 2\pi^2 r_5^3. \quad (3.44)$$

The mass of a 5D black string is

$$M_{bs} = \frac{r_0}{2}L \quad (3.45)$$

and its horizon area is

$$A_{bs} = 4\pi r_0^2 L, \quad (3.46)$$

where L is the length of the compact dimension.

For 5D BH with the same mass of a black string

$$M_{bh} = \frac{3\pi r_5^2}{8} = \frac{r_0}{2}L, \quad (3.47)$$

it has radius

$$r_5 = \sqrt{\frac{4r_0 L}{3\pi}}. \quad (3.48)$$

Therefore, the area becomes

$$A_{bs} = 2\pi^2 r_5^3 = 16r_0 L \sqrt{\frac{r_0 L \pi}{27}}. \quad (3.49)$$

The horizon area ratio between them is

$$\frac{A_{bh}}{A_{bs}} = \frac{16r_0 L \sqrt{\frac{r_0 L \pi}{27}}}{4\pi r_0^2 L} = \sqrt{\frac{16L}{27\pi r_0}} \quad (3.50)$$

In our study, we monitor this ratio over time to check how close the evolution of the black string is to a 5D BH.

3.6.1 The corrected thermodynamics

In this section, we present the corrected thermodynamics in first order.

The corrected mass M and area S on d -dimensional cylinder $\mathbb{R}^{D-1} \times S^1$ to first order in the total mass are [4]

$$M = \frac{(d-1)\Omega_{d-1}}{16\pi G_N} \rho_0^{d-2} \left(1 + \frac{\zeta(d-2)}{2(2\pi)^{d-2}} \rho_0^{d-2} + \mathcal{O}(\rho^{2(d-2)}) \right), \quad (3.51)$$

$$S = \frac{\Omega_{d-1}}{4G_N} \rho_0^{d-1} \left(1 + \frac{(d-1)\zeta(d-2)}{(d-2)(2\pi)^{d-2}} \rho_0^{d-2} + \mathcal{O}(\rho^{2(d-2)}) \right) \quad (3.52)$$

According to [5], the entropy S for multi-black holes is

$$S(\mu; \kappa) = S_1(\mu; \kappa) + S_1(\mu; -\kappa) \quad (3.53)$$

$$\begin{aligned} S(\mu; \kappa) = & \frac{(2\pi)^{d-1}}{4\Omega_{d-1}^{\frac{1}{d-2}}(d-1)^{\frac{d-1}{d-2}}G_N} \left[\left(\frac{1}{2} + \kappa \right) \mu \right]^{\frac{d-1}{d-2}} \\ & \times \left[1 + \frac{\zeta(d-2)}{(d-2)\Omega_{d-1}} \left(2^{d-4} + 2\kappa(1-\kappa)(1-2^{d-3}) \right) \mu + \mathcal{O}(\mu^2) \right] \end{aligned} \quad (3.54)$$

where S_1 and S_2 are entropies for two black holes, and

$$S_2(\mu; \kappa) = S_1(\mu; -\kappa). \quad (3.55)$$

We use this expression to calculate the total entropy of the first and second generations of the blobs in black string evolution.

Chapter 4

Endpoint of Black String Instability

The seminal paper [3] about the endpoint of the GL instability on the five-dimensional black string is an important piece of work in the field. Its numerical results from the fully nonlinear evolution of the black string constitutes a violation to the WCCC, which has tuned our understanding of the conjecture. The simulation in the paper is the only full numerical study about black strings at present. The simulation results are more than ten years old and have not been independently reproduced or verified in the literature. Moreover, it seems that the late-time dynamics of the evolution might be affected by the accumulating numerical errors. Higher quality numerics are needed in the late stage of the simulations. Therefore, the first goal of our study is to re-conduct the simulation with a different method, and reproduce the GL instability on 5D black strings by using completely independent methods and a different code. In particular, simulations by [3] used harmonic coordinates with the PAMR/AMRD libraries to solve the EFEs and used excision to get rid of the singularities. In our study, we use a different formulation, the CCZ4 formulation [89, 96], to conduct the simulations, with singularity avoiding coordinates and by using our own GRCHOMBO code [47, 48]. We reproduce the main results of [3] and confirm the late-time development of the GL instability of an unstable black string is a sequence of black holes connected by black strings in different scales. This process results in a pinch off of the horizon in finite asymptotic time, and thus yielding a naked singularity. However, our numerical results do not support for a global timescale that relates two subsequent generations, like what was stated in [3]. Therefore, the pinch off time is not simply determined by a

geometric series as stated in [3]. In fact, the late-time dynamics depends on two factors: the local dynamics of the bulges and the local GL instability. This leads to a faster approach to the singularity according to our simulation results. Our study provides further evidence against the WCCC.

This chapter starts with an overview of the weak cosmic censorship conjecture, the Gregory-Laflamme instability and a summary of the main results of the previous numerical study on the five-dimensional black strings in [3]. Then, we demonstrate the numerical approach and technical details that we adapt to achieve stable evolution of the black string spacetimes in our study in Sec. 4.2. In Sec. 4.3, we present the particular analysis methods we developed for black string simulations. In Sec. 4.4, we present our simulation results and its numerical interpretations about the GL instability of the black strings, as well as a comparison of our results with [3]. We improve simulation results with higher resolutions and extend the evolution further to get closer to the singularity of the GL instability. We analyse and give interpretations of our results and discuss the possible reasons that cause the differences between our results with [3]. Results from numerical tests are presented in Sec. 4.5. To obtain a more general picture of the evolution, we explore black strings with different lengths in Chapter 5.

4.1 Introduction

The existence of the singularities limits the predictive power of GR. The reason is simply that the theory does not apply at the spacetime singularities. However, to date there is no potential candidate found for the singularities in four-dimensional astrophysical settings. It seems that singularities resulting from the gravitational collapse are always hidden inside black holes. Based on the fact that no information can escape a black hole, it seems to be possible to formulate a global existence result for the spacetime outside of black holes. Motivated by this, in 1969, Penrose proposed the weak cosmic censorship conjecture [26] to address this issue, where singularities are conjectured to be always cloaked by black hole horizons. As long as no information can escape from black holes, it is safe. Later the theory has been formulated more precisely by [27, 28, 116]. The validity of the conjecture remains an important open question in the field for decades and until now. It has only been proven for some special cases. A rigorous mathematical proof or disproof to it still lacks. Thus, it remains as one of the biggest open questions in GR. In next section,

we introduce this conjecture and give an overview of the relevant studies in the way towards proof or disproof the weak cosmic censorship conjecture [26, 28, 29, 99].

4.1.1 The weak cosmic censorship conjecture

The *Weak cosmic censorship conjecture* (WCCC) says that

No singularity is visible from future null infinity and singularities must be cloaked by an event horizon from an observer at infinity.

It basically tells us that singularities must be hidden inside the black hole horizon and cannot be visible. In other words, there does not exist naked singularities. Whether the conjecture stands or not remains open for decades, and until now a rigorous mathematical proof is still lacking. If WCCC is true, naked singularities do not form generically from smooth initial data so that general relativity is sufficient to describe all gravitational phenomena outside the black holes. The physics near a singularity is now governed by quantum gravity but not by general relativity any more. In particular, quantum gravity effects are restricted to the region inside the black holes. If WCCC fails, then it is possible to observe the effects of quantum gravity directly.

There have been many attempts to prove or disprove the conjecture. The effort to prove or disprove the conjecture evolves both theoretical and numerical work. In four dimensions, there does not seem to have any counterexamples in astrophysical settings so far. Choptuik has proven that a naked singularity would form at the gravitational collapse of a spherical body when it has sufficiently large initial amplitude [30]. However, Choptuik's critical collapse is non-generic. Christodoulou has shown that within the Einstein-Scalar model, a singularity has to contain inside a BH or it does not exist for spherically symmetric case in four-dimensional asymptotically flat spacetimes [29]. In their work, a zero mass singularity, which could have been a potential counterexample to the conjecture, has been constructed numerically, but it turns out to be unstable and non-generic. Moreover, there has been works on constructing a trapped surface in full generality with generic initial data [117]. In four dimensions, the WCCC has been partially proven for the spherically symmetric case [29], but the proof to the general case are still open. The general proof without symmetry assumptions or counterexamples which are generic is still lacking. Recent progress about it can be found in [118].

However, in higher dimensions, there have been some evidence found against the WCCC. The first counterexample was found in the case of the five-dimensional black strings in 1993 [33]. Gregory and Laflamme (GL) found that the black string can be unstable to the long wavelength perturbations and it develops into ripples along the compact direction, which would possibly lead to a singularity in the end [33]. The endpoint of the GL instability of black strings was determined by Lehner and Pretorius [3] by carrying out the full numerical evolution of the unstable black string. The horizon of the black string would pinch off in finite asymptotic time, thus yielding a naked singularity. The numerical results from the endpoint of the instability indicates the formation of a naked singularity. More recently, a family of counterexamples to the WCCC have been found from numerical studies on the endpoint of the Gregory-Laflamme instability in similar scenarios in higher dimensions, such as black rings [34], ultra-spinning black holes [35] and black hole collisions [36, 48], as well as in the large D limit of GR [57, 89, 96]. There are also potential counterexamples in AdS [119, 120]. The discovery of the GL instability point us new directions towards verifying the WCCC.

4.1.2 The Gregory-Laflamme instability

In this session, we introduce the Gregory-Laflamme (GL) instability and summarise the results from previous studies about the endpoint of the GL instability which constitutes a violation to the WCCC.

As the most important solutions of the EFE, BHs are known to be stable in four dimensions and can only have spherically symmetric geometry. However, the situation can be very different in higher dimensions where black holes can have different kinds of topology and can be unstable to gravitational perturbations. For example, black strings are found to be unstable to linear perturbations when it is thin enough. The discovery of the GL instability point us new directions towards verifying the WCCC. It was first shown by Gregory and Laflamme that the black string solution is unstable to small perturbations in 1993 [33]. They found that if there is a linear perturbation of the black string solution, it will grow exponentially in time and the horizon will begin to ripple (see Fig. 4.1). Moreover, they predicted that the endpoint of the instability would be a 5D localised BH. As by the theory of entropy, a BH would have the largest entropy among all. The singularity that forms at the endpoint of the black string instability potentially constitutes a violation to the WCCC. It takes years for the initial numerical simulations to run. In 2003, the

first numerical study was carried out on the black string confirms the ripples in the GL instability [121].



Fig. 4.1 A demonstration of the unstable black string that induces ripples along the compact string direction.

However, the development of the instability is not determined, until the seminal study of full evolution of black string was carried out by Lehner and Pretorius in 2010 [3]. The study shows that the unstable black string develops into a fractal structure. The late-time development of the horizon can be described by a sequence of spherical BHs connected by shrinking string segments in different scales. Each string segment itself is unstable, subject to the GL instability. They argued that the dynamics of the GL instability is (global) self-similar so that the pinch off time can be estimated by a geometry series and thus finite. According to Proposition 9.2.5 in [122], horizon cannot bifurcate smoothly. Therefore, the horizon would finally pinch off somewhere on the string in finite asymptotic time, yielding a naked singularity. Their simulation results support this point as the curvature invariant would blow up at the horizon when the development of the instability is close to the pinch off. They also predict that the endpoint of the black string instability is a 5D Schwarzschild BH as this is an entropy-favoured solution. Since no fine tuning is needed for the simulation, their results constitute to a generic counterexample to the WCCC.

More recently, there has been a family of further studies that also suffer from the GL instability on black rings, ultra-spinning BHs and BH collisions [34–36]. The results from these numerical studies contribution to concrete counterexamples of the WCCC from the perspective of numerical relativity.

4.1.3 Previous numerical evolution on the black string

The existence of the black string instability in five dimensions has been proven by Gregory and Laflamme in 1993 [33]. They concluded that when the horizon pinches off there will form a naked singularity, suggesting a violation to the WCCC. However, it took twenty years for the first numerical evolution of black string to run, which confirms the ripples of the unstable black string [121]. The full numerical evolution of black string spacetime was successfully carried out by Lehner and Pretorius in 2011, where the endpoint of the perturbed black string was determined [3]. In their numerical study, the spacetime was evolved by Generalised Harmonic (GH) formulation of the Einstein equations. Constraint damping terms have been added to the Harmonic Decomposition of EFE to cure the problem causing by the truncation errors. It has been found that the development of black string instability develops to *self-similar* structure where the black string keeps shrinking over time, increasing number of the segments of it turns to various sizes of hyper-spherical black holes. This shrinking process will continue until a zero-mass naked singularity is formed within a finite amount of time. Their numerical study provides a concrete evidence against the WCCC. In this section, we summarise the key results from the previous study [3].

In [3], the simulation was carried out on a computational domain with dimension $(r, w) \in ([0, 320M] \times [0, L])$, where r refers to the radial direction and w refers to the compact string direction in the computational coordinates. Each direction initially has $(N_r, N_w) = (1025, 9)$ points on the grid that uniformly covers the entire domain. They started the simulation of an initial black string which has compact length $L = 20M$ and radius at $r_0 = 2M$. The perturbation in [3] was introduced to the physical metric along the string direction x by

$$\gamma_\Omega = 1 + A \sin\left(x \frac{2\pi q}{L}\right) e^{-(r-r_0)^2/\delta_r^2}. \quad (4.1)$$

where A is a parameter that determines the amplitude of the perturbation, q controls the spatial frequency of the perturbation, and r_0 and δ_r control the region of the perturbation in the radial direction. In their simulation, they used $A = 0.1$, $q = 1$, $r_0 = 2.5$ and $\delta_r = 0.5$. The other variables are then found numerically by solving the Hamiltonian and momentum constraints. The spacing is $0.3/M$ at the coarsest level in the low resolution run. The simulation starts with 3 additional levels and ends up with 16 additional levels, which are added by AMR algorithm that based on their specific maximum truncation error tolerance [3].

The shape of the initial perturbed black string and the evolution of the horizon can be found in Fig. 4.2 (or Fig.1.2 in [4.2]). The excision region was chosen to follow the shape of the AH, but 10 and 50% smaller in radius [3]. In the first 200M in time, the perturbation added has been growing over time and the first generation is gradually forming. By time 220-220M, we can clearly see there has formed the second generation the the middle of the string segment. In the later time of evolution, from $t = 220 - 226M$, the horizon can be described as black holes connected by black string segments. This is also supported from the evolution of the intrinsic geometry over time (Fig.1.3 in [3]). The invariant Kretschmann along the string segment is nearly 1 which corresponds to the value for an exact black string, and is nearly 6 near each generation, which corresponds to an exact spherical black hole.

$$\Delta T \approx T_0 + \sum_{i=0}^{\infty} T_1 X^i = T_0 + \frac{T_1}{1 - X}. \quad (4.2)$$

Moreover, they pointed out that the time scale that relates the formation time of the subsequent generations is $X \approx 1/4$ times that of the preceding one. They think that the time scale is expected to be proportional to the string radius if the local instability is qualitatively like the GL instability of an exact black string. As a result of (4.2), they concluded that the time to pinch off is $\Delta T/M \approx 231$. At this time, the string segment will have zero radius so that the self-similar cascade will terminate. This indicates the formation of a naked singularity and therefore constitutes a violation to the WCCC.

They found more evidence to support the above conclusion based on the following observations. Firstly, the simulation results support that the radius of the some selected position on the AH is decreasing linearly over shifted-logarithmic time (Fig.1.4 in [3]). It is consistent with the self-similar scaling to zero radius at the corresponding finite asymptotic time. This observation is qualitatively the same as that observed in the case of fluids, where the scaling law is known as [123, 124]

$$R \propto (t_c - t). \quad (4.3)$$

where R is the radius of the fluid column, which decreases with time t linearly until the breakup time t_c . Secondly, they claimed that the self-similar nature of the instability will give rise to a fractal structure before the pinch-off. This implies

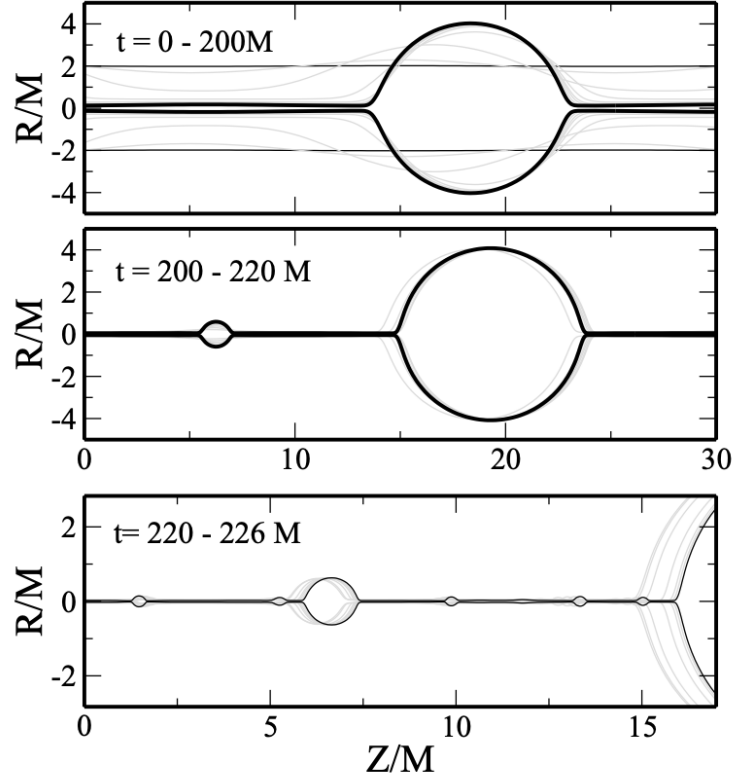


Fig. 4.2 The embedding diagram of the apparent horizon from [3].

that the proper length $L_p(t)$ of the string will grow with the development of each subsequent generation. By assuming that the scaling law takes the form of 4.25 and the properties of the string radius follows the scaling suggested by Table 1.1 in [3]), they measured the slope in the logarithmic plot of the evolution of the proper length (Fig. 1.5 in [3]) by

$$L_p(t) \propto (t_c - t)^{(1-d)}, \quad (4.4)$$

They found the slope of the linear fit to the late-time dynamics is ~ 0.048 . As a result, the Hausdorff dimension $d \simeq 1.05$, which is greater than 1 as expected.

To quantitatively understand the late-time behaviour of the horizon, [3] analyse the mode behaviour of the string segment by decompose the horizon $R_{AH}(t, w)$ between $w \in [0, 10M]$ from $t \in (175M, 205M)$ by the following expansion

$$R_{AH}(t, w) = c_0 - \sum_{l=1}^{\infty} c_l \sin(l\pi w), \quad (4.5)$$

where up to $l = 6$ coefficients c_l have been extracted. They found that only the $l = 1$ mode displays the growing behaviour (see Fig.1.6 in [3]), which is somehow expected as at this stage of the highly dynamical evolution.

The numerical study on the black string, as the most studied case in higher dimensions, provides us an insight into the dynamics of higher-dimensional black holes. However, many aspects of the simulation can be improved and there are still many questions and concerns about the black string instability. In their study, excision technique is necessary to remove the geometric singularity inside the horizon from the computational domain. As a result, the apparent horizon has to be found periodically during the simulation. However, in their study finding the apparent horizon became rather costly in the later time of the evolution. One reason is that the algorithm, i.e. flow method, to find the apparent horizon in their study is not very efficient. On the other hand, in the case of GH formulation, the apparent horizon needs to be found periodically for excision purpose. Particularly in the later time when the dynamics of the horizon becomes rapid and vivid, it has to be found more frequently, which makes the time for the overall evolution extremely increased. Moreover, the rules governing the evolution of the horizon remain unclear and more details are desired about the dynamics of the spacetime in the later time of evolution. Therefore, in our study we use a different formulation, i.e. CCZ4 formulation, in order to verify whether the development of horizon follows a self-similar structure and to discover the rules governing it. With CCZ4 formulation, it is possible to evolve the spacetime without excision. Another advantage of using this formulation is that we can separate the process of finding the horizon from evolving the spacetime. As a starting point, we focus on the black string solution in five dimensions with the same settings as [3]. Based on that, we will be able to investigate black strings with different lengths in higher dimensions.

4.2 Numerical methods

In our study, we conduct the fully non-linear numerical evolution of the black string in five dimensions. In this section, we present the numerical methods we use to achieve stable evolution of black string spacetimes, including the initial data, gauge conditions and singularity diffusion. In particular, we show the specific grid hierarchy we choose. We give in detail our simulation results and its numerical interpretation. In addition, we present the results from numerical tests.

We start with the black string which has the same radius and length ratio as in [3], so that we can directly compare our simulation results with theirs. We aim to push the evolution as close to the singularity as possible. In our work, we follow the conventions $G = c = 1$.

The five-dimensional black string we work on takes the following metric:

$$ds^2 = -\left(1 - \frac{r_0}{r}\right) dt^2 + \left(1 - \frac{r_0}{r}\right)^{-1} dr^2 + r^2 d\Omega_{(2)}^2 + dz^2, \quad (4.6)$$

where r is the Schwarzschild radius, r_0 is the mass parameter of the black string and $d\Omega_{(2)}^2$ is the line element of the 2-dimensional unit sphere. With the extra dimension of compact length L , the mass of a black string is hence

$$M_{BS} = \frac{1}{2} L r_0. \quad (4.7)$$

When $L = 10$, the black string has the same radius and length ratio as in [3], where this specific ratio was chosen as it corresponds to the fastest growth rate of the instability. With $L = 10$, in theory, our simulation results should be quantitatively the same as [3].

4.2.1 The evolution

For the evolution, we solve the vacuum EFE in 4+1 dimensions with $U(1) \times SO(3)$ isometry imposed. We employ the CCZ4 formulation [89, 96] on a Cartesian grid by using our own GRCHOMBO code [47, 48]. The symmetry are reduced by the modified cartoon method [46]. We set the whole computational domain to be $[z, x] = [0, 10] \times [0, 256]$. That is to say, the string direction z has length $L = 10$, where we apply periodic boundary. And the outer boundary is at $256r_0$ in the Minkowski directions. We apply either Sommerfeld or periodic boundary conditions at the outer boundary. Note that it does not really matter which boundary condition to use. As long as the outer boundary is put far away from the region, it will not have any causal contact with the black string physics. Typically we set the grid spacing to be $dx = 0.25r_0$ at the coarsest level. In total there are 13 levels of refinement that we have on the computational domain, with a refinement ratio of $2 : 1$. This means the resolution at the finest level is $\sim 6 \times 10^{-5} r_0$. We evolve the lapse and shift vector by the CCZ4 ($1 + \log$) slicing with an advection term and the modified Gamma-Driver shift condition. We reduce the dimension of the problem

to 2+1 by applying the modified cartoon method [46]. The generalised equations of CCZ4 formulation can be found in Chapter 2.

To discretise the spatial derivatives, we use 6th order finite differences method. As for time derivatives, we use the standard RK4 time integrator. Since the overall convergence order is not greater than four, we use 6th order Kreiss-Oliger dissipation. In Sec. 4.5, we show that the order of convergence in our simulation is roughly three. This is what one would expect for a typical AMR code like GRCHOMBO. Similar to [34–36], we add diffusion terms to the right hand side of the equations well inside the apparent horizon, which helps to control the gradients near the coordinate singularity in the computational domain inside the black hole. We only add those terms to the variables which have second order spatial derivative terms. To achieve stable simulation of the black string spacetimes, we redefine the constraint damping parameter $\kappa_1 \rightarrow \kappa_1/\alpha$ as in [89], where α is the lapse function. For the damping parameters we use $\kappa_1 = 0.37$, $\kappa_2 = -0.8$, and $\kappa_3 = 1.0$.

4.2.2 Gauge conditions

The lapse function we use is the standard $1 + \log$ slicing condition,

$$(\partial_t - \beta^i \partial_i) \alpha = c_\alpha \alpha (K - 2\Theta), \quad (4.8)$$

where we set $c_\alpha = 1.3$, K is the trace of the extrinsic curvature and Θ is one of the CCZ4 evolution variables. The shift condition we use is the integrated Gamma-driver,

$$(\partial_t - \beta^j \partial_j) \beta^i = c_\beta \hat{\Gamma}^i - \eta \beta^i, \quad (4.9)$$

where $c_\beta = 0.6$ and $\hat{\Gamma}^i$ is the CCZ4 evolution variable. Note that the extra term that relates to the constructed Christoffel symbols of the conformally rescaled initial spatial metric as in [34–36] are not included here. The particular reason is that those terms are vanished according to our initial conditions.

4.2.3 Modified Gamma-Driver

We evolve the shift by following the condition in [35] that

$$\partial_t \beta^i = F(\Gamma^i - f(t)\Gamma_{t=0}^i) - \eta(\beta^i - \beta_{t=0}^i) + \beta^k \partial_k \beta^i, \quad (4.10)$$

where $f(t)$ is a function decays in time, F and η are free gauge parameters. The gauge parameters c_α and c_β are typically chosen to be $c_\alpha = 2$ and $c_\beta = 0.75$ in other cases such as black holes binary mergers in astrophysical settings. In our simulation, we choose $F = 0.6$ and $\eta = 1$. In the case of black string evolution, since in GP coordinates $\Gamma_{t=0}^i = 0$, the conditions we actually implement in the code are

$$\partial_t \beta^0 = F * \Gamma^0 - \eta_d \beta^0 + \mu_\beta \beta^k \partial_k \beta^0, \quad (4.11)$$

$$\partial_t \beta^1 = F * \Gamma^1 - \eta_d(\beta^1 - \beta_{Ref}^1) + \mu_\beta \beta^k \partial_k \beta^1, \quad (4.12)$$

where β_{Ref}^1 is chosen to be half value of the initial shift, that is $\beta_{Ref}^1 = 0.5 * \beta_{t=0}^1 = 0.5\sqrt{1/y}$, μ_β is 1, and η_d is 1 for $y < 10^{12}$ and it decays when $y > 10^{12}$.

4.2.4 Initial data

We start the evolution with the unperturbed black string solution in five dimensions in Gullstrand-Painleve coordinates [125, 126],

$$ds^2 = -\left(1 - \frac{r_0}{r}\right) dt^2 + 2\sqrt{\frac{r_0}{r}} dr^2 + dr^2 + r^2 d\Omega_{(2)}^2 + dz^2. \quad (4.13)$$

where r_0 is the usual Schwarzschild mass parameter, $z \sim z + L$ is the compact direction with period length L , and $d\Omega_{(2)}^2$ is the standard metric on the unit round two-sphere. The ADM mass of the metric in our case is therefore

$$M = \frac{1}{2} L r_0. \quad (4.14)$$

The advantage of using this coordinate is that it is horizon-penetrating and in GP coordinates, the spatial metric is flat. The only non-trivial part contains in the conformal factor χ . Therefore, it makes it particularly convenient to construct perturbed initial data. The only physical singularity can be removed by turducken method [113, 114]. We cut off by hand the range of in the radial direction. That is, we let $r = \epsilon$ and evolve the initial data quantities of (4.13) for $r < \epsilon$. We typically use $\epsilon = 0.1r_0$. Note that we only employ this regularisation procedure at the level of

the initial data; at the later stages in the evolution, the x coordinates takes values in $0 < x < x_{max}$. Note that in [3], they use $M_{Schw} = r_0/2 = 1$ so that our results are related to theirs by a rescaling factor of $1/2$. Then, we can read off the $4 + 1$ quantities from the initial data (4.13). In Cartesian coordinates $\det \gamma = 1$ and hence the unperturbed conformal factor satisfies $\chi \equiv (\det \gamma)^{\frac{1}{4}} = 1$. Furthermore, the Christoffel symbols associated to the spatial conformal metric $\tilde{\gamma}_{ij}$ trivially vanish. To trigger the GL instability, the perturbation is added to the conformal factor χ by

$$\chi = \chi \left[1 + \epsilon \sin \left(\frac{2\pi q z}{L} \right) \right] e^{-\left(\frac{x}{r_0} - \frac{r_0}{x} \right)^2}, \quad (4.15)$$

where ϵ is the amplitude of the perturbation and $q \in \mathbb{N}$ is the frequency that selects which GL harmonic to be excited. This is constraint-violating. The exponential part ensures that the perturbation is added only to the region near the horizon. In our simulations, we set ϵ to be 0.01 and n to be 1. During the simulation, we keep track of the constraint violations introduced by our perturbation and ensure that for they are exponentially suppressed by the damping terms. The remaining $4 + 1$ quantities are left unperturbed; for the initial lapse α and the shift vector β^i , we set $\alpha = 1$ and $\beta^i = 0$. Our choice of the lapse and shift implies that there is a strong initial gauge adjustment superposed with the physical evolution of the GL instability. This period of gauge adjustment happens at the beginning of the evolution and typically lasts for $t/r_0 \sim 10$. On the contrast, the GL instability appears at time $t/r_0 \sim 70 - 100$ or even later in our simulations with the initial perturbed data we choose.

4.2.5 Singularity Diffusion

In higher dimensions, the gradients can be really steep near the singularity. These large gradients comes from the coordinate singularity in the conformal metric as the conformal factor cannot fully absorb the singularity. The diffusion terms introduced in [35] was inspired from the techniques in dealing with the shock problem in the context of computational fluid dynamics [127–129]. Based on the diffusion terms in [35], we add a term in addition to the evolution equation for $\tilde{\gamma}_{ij}$. It is of the form

$$c_L \Delta x^2 g(\chi, |\partial \tilde{\gamma}_{ij}| (\nabla^2 \tilde{\gamma}_{ij})^{TF}) \quad (4.16)$$

where c_L is a dimensionless parameter, Δx is the grid spacing and $g(\chi, |\partial\tilde{\gamma}_{ij}|)$ is a function to ensure this term is only added to the inside of the horizon and is nonzero when the gradients in $\tilde{\gamma}_{ij}$ becomes large. It is in the form

$$g(\chi, |\partial\tilde{\gamma}_{ij}|) = H(\chi_c - \chi) \sqrt{\frac{2}{D(D-1)} \sum_{i,j,k} (\partial_k \tilde{\gamma}_{ij})^2}, \quad (4.17)$$

where H is the Heaviside step function, χ_c is the cut-off value to ensure that the diffusion term stays inside the apparent horizon.

4.2.6 Localised perturbation

It is also possible to introduce a small perturbation to χ after achieving stable simulations for the unperturbed black string. The perturbation can be added only locally to the region near the horizon:

$$\chi \rightarrow \chi \left(1 + A \sin \left(\frac{2\pi q x}{L} \right) \right) \psi(x, y).$$

where we set $A = 0.25$, the frequency $q = 1$ and $\psi(x, y)$ is a function to localise the perturbation. It is defined as $\psi(x, y) = \psi_1(y)\psi_2(y)\psi_3(x)\psi_4(x)$, where

$$\begin{aligned} \psi_1(y) &= \begin{cases} 0 & y \leq y_1 \\ \frac{e^{-\frac{y_2-y_1}{y-y_1}}}{e^{-\frac{y_2-y_1}{y-y_1}} + e^{-\frac{y_2-y_1}{y_2-y}}} & y_1 < y < y_2, \\ 1 & y \geq y_2 \end{cases} & \psi_2(y) &= \begin{cases} 1 & y \leq y_3 \\ \frac{e^{-\frac{y_4-y_3}{y_4-y}}}{e^{-\frac{y_4-y_3}{y-y_3}} + e^{-\frac{y_4-y_3}{y_4-y}}} & y_3 < y < y_4 \\ 0 & y \geq y_4 \end{cases} \\ \psi_3(x) &= \begin{cases} 0 & x \leq x_1 \\ \frac{e^{-\frac{x_2-x_1}{x-x_1}}}{e^{-\frac{x_2-x_1}{x-x_1}} + e^{-\frac{x_2-x_1}{x_2-x}}} & x_1 < x < x_2, \\ 1 & x \geq x_2 \end{cases} & \psi_4(x) &= \begin{cases} 1 & x \leq x_3 \\ \frac{e^{-\frac{x_4-x_3}{x_4-x}}}{e^{-\frac{x_4-x_3}{x-x_3}} + e^{-\frac{x_4-x_3}{x_4-x}}} & x_3 < x < x_4 \\ 0 & x \geq x_4 \end{cases} \end{aligned}$$

where $x_1, x_2, x_3, x_4, y_1, y_2, y_3, y_4$ are parameters to help localize the perturbation. Therefore, the function $\psi(x, y)$ is well-defined on the (x, y) plane and the perturbation is smoothly localized to a region near the horizon and centered in the string direction.

4.2.7 Grid hierarchy

The location where the first generation would form along the string depends on the initial conditions. Apart from that, the problem should respect \mathbb{Z}_2 symmetry about the centre of the first generation, since the initial data which has zero momentum as in our case and in [3]. This is because the $n = 1$ GL harmonic governs the subsequent universal evolution of the strings has this symmetry. So in perfect conditions, we should expect to see the subsequent generations to appear symmetrically about the first generation along the string. However, in [3] the generation beyond the third one is not symmetric any more. We believe it is due to the accumulating numerical errors that have different impacts on different sides of the string segments that eventually affects the development of the instability. This effect can be visible from the third generation onwards during the evolution of the instability shown in Fig. 2 of [3]. This also happens in our simulations, that when the finer levels are automatically added as the evolution of the instability unfolds, it becomes problematic. The asymmetry of various refinement levels can subtly add truncation errors to the whole system, which could accumulate over time and break the physical symmetry of the problem in the end. In this section, we provide details of the grid hierarchy that we use in our simulations to ensure that our numerical method respects the \mathbb{Z}_2 symmetry.

There are several ways to control the grid hierarchy during the evolution. Previously, the usual refinement criterion is based on the gradients of the conformal factor χ , as the χ could be a good estimate of location of the horizon. So χ tagging χ is used in similar problems using GRCHOMBO [34–36, 130]. This type of criterion thus provides a level hierarchy that roughly follows the shape of the horizon. Hence it can potentially save the computational cost of the simulations. Whereas, there is no underlying symmetry is assumed in the previous problems considered in [34–36, 130], so that one does not have to worry about any potential symmetries that might be affected by the numerical method one uses. Therefore, using χ tagging χ is the most convenient and efficient choice in the above cases. However, in our case, we do not find an efficient way to enforce the \mathbb{Z}_2 symmetry on the levels dynamically based on the conformal factor χ or something similar. There are mainly two reasons. First, the dynamical variables such as the conformal factor χ could change dynamically during the evolution (especially when a new generation is forming), so that the levels could not well capture the shape of the horizon based on the conformal factor χ . Figure 4.3 gives an example that using this criterion, extra levels are added to the region above the horizon. Thus, the finer level does not well capture the shape

of the horizon as we want. Moreover, the truncation error would lead to asymmetric levels as well (see Fig 4.3). At the boundary value we set to decide to whether add a box or not, tiny numerical errors could lead to opposite answers. This is almost unavoidable due to the way we add the boxes in numerical simulations. In one simulation we run using chi criterion, we get asymmetric horizon at the two side of the big blob in Fig 4.3. Hence, criterion based on the chi are not stable, as it would be hard to enforce \mathbb{Z}_2 symmetry based on the chi.

The left one in Fig. 4.3 gives an example of the hierarchy of the innermost refinement levels that result from using the χ tagging criterion. As we can see from this figure, the levels are not fully symmetric about the first generation. This leads to accumulating errors from the level boundaries that causes unphysical effects in the late time. In our simulations, the effects typically show up beyond the third generation, unless very high resolution is used. Another issue about using chi criterion in the black string simulation is that, the finest levels inside the big blob (Fig 4.3) take a large portion of the total computational resources. It seems to a huge waste to compute the inside with so much resolution. We have tried to remove or minimise the finest levels inside, but the numerical error from the inside and from the extra level boundaries accumulates and could grow out of control and contaminate the evolution in practice. Furthermore, when there are lots of dynamics e.g. when new generations appear, the variable χ changes very rapidly in some regions so that more regridding is needed. This could not only add potential burden to the computational costs, but also causes higher levels of numerical errors due to the need of highly frequent regridding. In addition, we also tried other dynamical refinement criteria based on the trace of the extrinsic curvature trK or the CCZ4 variable Γ^i but the results were qualitatively the same as the χ tagging criterion.

Therefore, we use a rather simple criteria, rectangular levels. With this criterion we can ensure that the truncation errors do not interfere with the dynamics of the unstable black strings, we enforce that all refinement levels are rectangular-shaped. The right figure in Fig 4.3 gives an example of the innermost levels of such level hierarchy. In this case, \mathbb{Z}_2 symmetry is fully respected, and we only need to ensure enough resolution at the thinnest part of the horizon. Note that this shape of the refinement levels ensures that our numerical method respect the symmetry but does not enforce it. As a result, the not-so-thin part of the horizon are overly resolved. The consequence is it would potentially cost more computational resources, but on the other hand, the finest levels inside the big blob are much smaller than that using

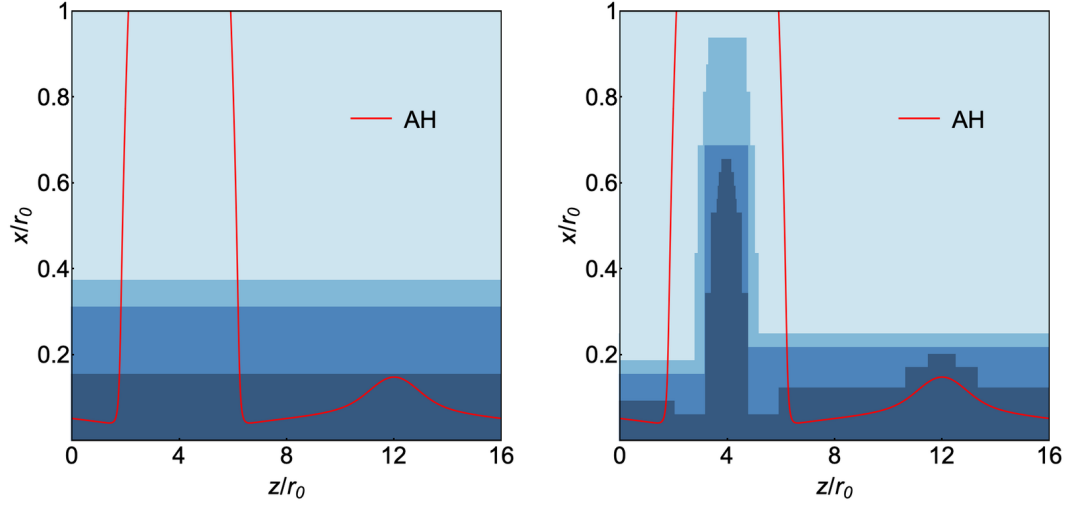


Fig. 4.3 Examples of the grid hierarchy from two different refinement criteria from a black string with length $L = 16$. Left: grid hierarchy from χ tagging criterion. The grid structure is dynamically changing with the evolution based on the gradients of the evolution variable χ ; Right: grid hierarchy from rectangular tagging criterion. The location of each level depends on the resolution at the AH. The actual location of the AH is depicted in a red curve.

chi criterion. Furthermore, the levels are fixed once they have been added. Thus, no regridding is required using this criterion. This could reduce the numerical errors from regridding. Therefore, the computational cost of the simulations with this criteria is comparable to that with $|\partial\chi|$ -based refinement criterion. The thinnest parts of the AH of the black string determine the necessary resolution of the finest level, which in turn essentially determines the computational cost of the simulation.

In our simulations, we require at the apparent horizon is covered by as least 40 grid points. (Note that because of the reflection symmetry about $x = 0$, our criterion actually ensures that the apparent horizon is covered by at least 80 points). In practice, we typically have more than 60 grid points covering it. (This corresponds to 120 points covering the apparent horizon). Whenever there is not enough grid points during the evolution, we add another finer level. With rectangular refinement levels, there are some of the not-so-thin parts of the AH that are overly resolved. However, since the finest refinement level only covers a small portion of the interior of the big blob, it will not add much extra computational cost in all. Furthermore, once a new level is added, we fix it and we do not regrid anymore. This could in turn reduce the frequent interpolation and extrapolation process that are required by the other criteria at the level boundaries. Therefore, it can help save some

computational cost, as well as control the numerical errors and speeds up the overall simulation.

4.3 Analysis methods

We monitor several quantities during the evolution to have a better insight of the dynamics: the overall geometry of the apparent horizon and its embedding, the curvature invariant and the horizon area.

4.3.1 Apparent horizon

The apparent horizon is tracked by the apparent horizon finder in GRCHOMBO which applies Newton method. We assume that the AH can be found by a level set $F = 0$ of the function

$$F(x, z) = x - h(z). \quad (4.18)$$

Following [3, 121], we produce the embedding diagrams of the geometry into \mathbb{R}^4 :

$$ds^2 = dR^2 + R^2 d\Omega_{(2)}^2 + dZ^2, \quad (4.19)$$

This could help us to obtain some intuitive idea about the shape of the AH during the evolution. In the equation above, Z is periodic. For the embedding diagram, coordinate R is the areal radius of the horizon S^2 . In GRCHOMBO coordinates, it is,

$$R(z) = \sqrt{g_{ww}} h(z), \quad (4.20)$$

and coordinate Z is defined to satisfy that the proper length in the string direction z is the same as the Euclidean length of $R(Z)$ in the embedding.

$$Z(z) = \int_0^z d\bar{z} \frac{\sqrt{g_{zz} + 2g_{zx}h'(\bar{z}) + g_{xx}h'(\bar{z})^2}}{\sqrt{h'^2(\bar{z}) + 1}}, \quad (4.21)$$

In addition, we also monitor the normalised spacetime Kretschmann invariant, which is evaluated on the AH by

$$\mathcal{K} = \frac{1}{12} R_{abcd} R^{abcd} R_{\text{AH}}^4, \quad (4.22)$$

where R_{AH} is the location of the apparent horizon. The normalisation has been chosen so that $\mathcal{K} = 1$ at the horizon of a stationary uniform black string, and $\mathcal{K} = 6$ at the horizon of an asymptotically flat 5D Schwarzschild black hole. The horizon area can be found by

$$A = \int_0^z dz' \sqrt{g_{zz} + 2g_{zx}h'(z') + g_{xx}h'(z')^2} \sqrt{g_{ww}} h(z'). \quad (4.23)$$

which should be non-decreasing during the evolution.

4.4 Results

In our simulations, we fix the mass parameter of the parent 4D Schwarzschild black hole to $r_0 = 1$ and the asymptotic length of the compact circle $L = 10r_0 = 10$. We evolve the black string with the same mass/length ratio as [3] so that we can directly compare our results with theirs. We aim at pushing the run as long as possible. Note that [3] present their results in units of initial 4D Schwarzschild mass $M_{\text{Schw}} = r_0/2 = 1$ so that their results are related by an overall rescaling of factor 2 with ours. In the simulation, we fix the mass parameter of the parent 4D Schwarzschild black hole to $r_0 = 1$ and the length of the compact circle $L = 10$. This corresponds to the same mass length ratio in [3] and it is chosen because it leads to approximately the fastest growth rate for the shortest wavelength instability. We evolve on the perturbed black string and aim at evolving the system as far as possible. Similar to [3], we find that the GL instability of a uniform black string develops into a fractal structure. That is the system can be described by a sequence of spherical BHs connected by string segments on different scales. In the following, we present our results in detail for the $L = 10$ run.

4.4.1 The geometry of the AH

In Fig 4.4, we display the embedding diagram from the last stage of our simulations for $L = 10$. We superpose the normalised Kretschmann invariant K imposed on the horizon as in the red curves. Our values of Kretschmann are similar to [3]. As already described in [3], the blobs has Kretschmann value close to 6 which corresponds to a 5D BH, and the string has value close to 1 which corresponds to a black string. Indeed, the horizon can be described by black holes connected by black strings in various scales. It is clear from Fig 4.4 that the distribution of the

bulges are fully symmetric about the first generation. This is due to the initial data we chose.

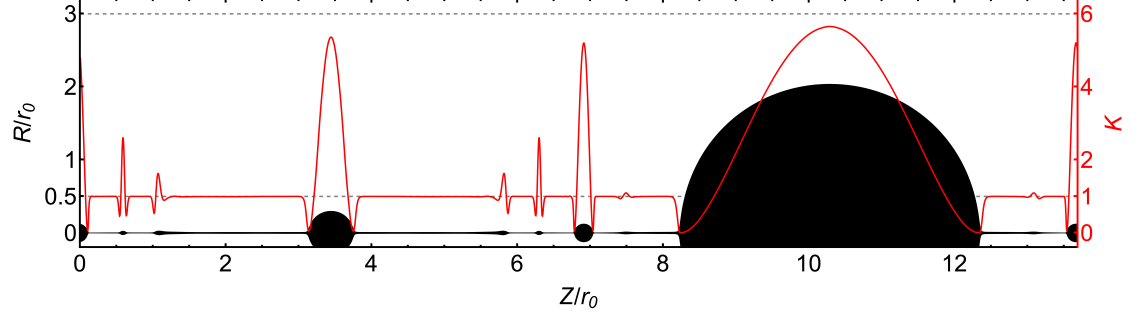


Fig. 4.4 Embedding of the AH, with induced Kretschmann invariant (in red curve) imposed on the AH.

Near the third generation, the fourth generation has already formed on one side of the third generation and it is still accreting mass from the string segments near it. The fifth and the sixth generation are also forming on different string parts. And we can see that the string segments connecting different generations are non-uniform at the late stage of the evolution. The thinnest part of the string is at somewhere between the third generation and the fourth one (see Fig 4.5).

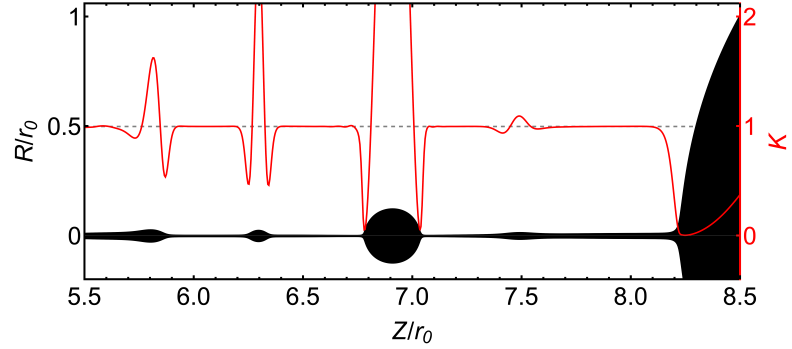


Fig. 4.5 Zoom-in of the region near the 3rd generation on the embedding of the AH. The induced Kretschmann invariant is imposed on the AH in red curve.

4.4.2 Horizon dynamics

To have a better idea of how the horizon develops over time, we plot the snapshots of the horizons at several times on the same plot in Fig. 4.6. The first three panels in Fig. 4.6 correspond to Fig. 4.2 in [3]. It has been deliberately plotted in a similar

style as that in [3] (see Fig. 4.2), so that we can directly compare our results of the AHs at different stages of the evolution with theirs.

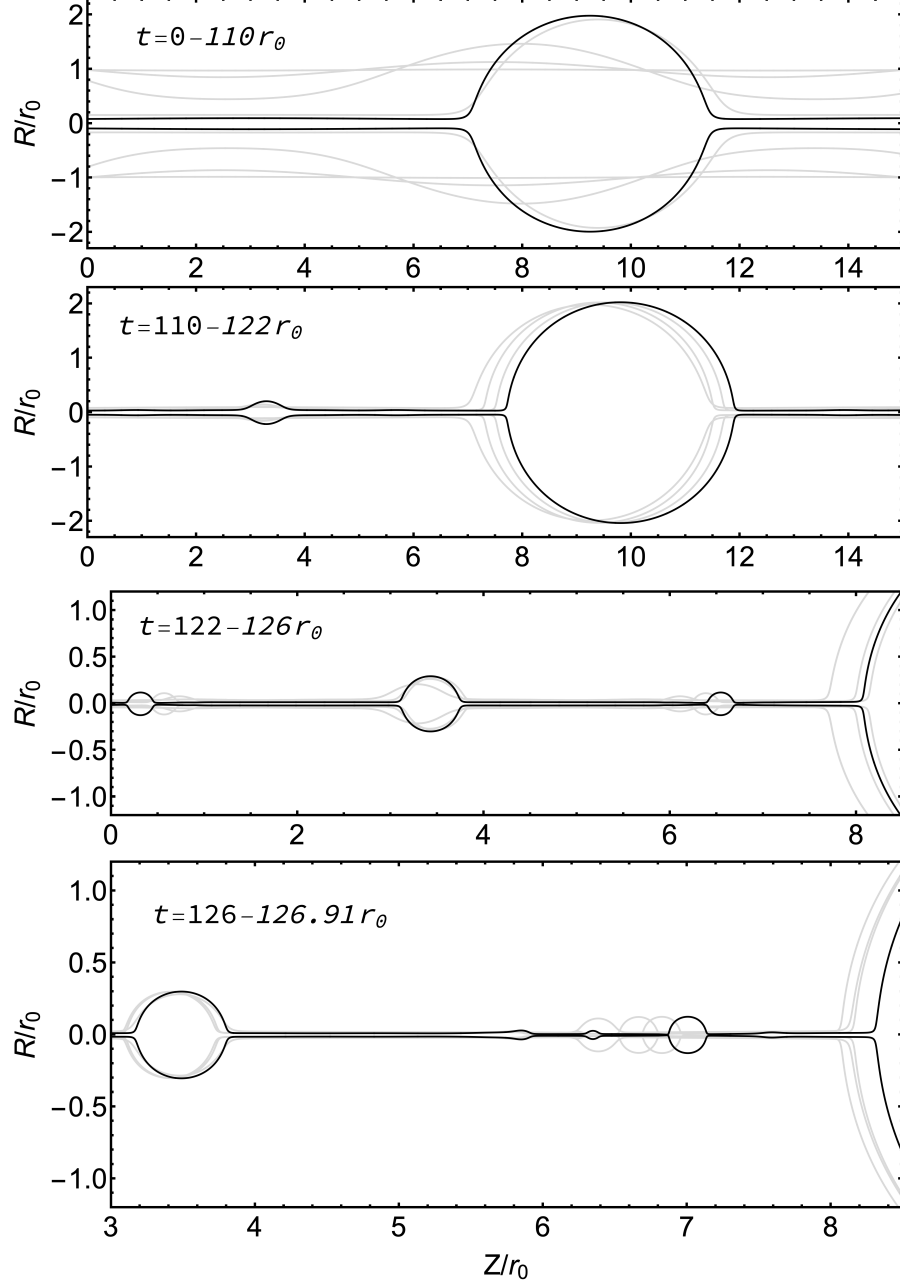


Fig. 4.6 Snapshots of the embedding diagrams of the AHs in our simulation at different stages. The length in the Z direction extends to 13.69 in the $L = 10$ case.

From our simulation results, we confirm that the black string instability develops into a series of hyperspherical black holes of various sizes connected by string segments in different scales. Each string segment itself, as it is sufficient long and thin, is unstable to the GL instability. This determines the fate of the subsequent

development of the instability. Up until $t = 122r_0$, our evolution results agree with [3] very well. The second generation forms exactly at the middle of the string segment. Furthermore, in our case we also see the satellite black holes beyond the third generation are moving towards the former generation, stretching the string segments connecting them. This is consistent with [3] that the satellites have some non-zero velocity in the string direction so that they will merge eventually.

However, the generations beyond the third one are not fully symmetric any more in [3] (see the third panel in Fig. 4.2), whilst in our case we can see clearly the third generations are symmetric about the first and the second generations (see last panel in Fig. 4.6). In particular, in the third generation, there is only one satellite black hole forming on each piece of the string segment connecting the first and the second generations in our case. The dynamics beyond the third generation becomes more chaotic. As we can see from the last panel in Fig. 4.6, the formation of the fourth generation and beyond are not at the centre of the corresponding string segment any more. Moreover, the movement of the satellites increase the non-uniformness of the string segment and thus speed up the dynamical process at the late stage of the evolution (see last panel in Fig. 4.6).

4.4.3 Dynamics beyond the third generation

In each of the first three generation, there is only one satellite black hole forming at each string segment. However, the dynamics beyond the third generation are more chaotic.

In Fig. 4.7, we plot the embedding diagrams of the AH where the second and the third generation form. As we can see, the second generation forms at exactly the middle of the string segment. When the second generation has formed, the string segment connecting it and the first generation are not uniform. This non-uniformness of the string triggers the formation of the next generation.

Fig. 4.8 shows the formation of the third generation and beyond. Each string segment in the top panel has formed one third generation. In the beginning, the third generation is forming at the middle of the string segment. Then it is moving towards the first generation and this movement continues and speeds up after it has formed. The same thing happens to the following generations as well. At late time, the local GL instability and the movement of the generation together control the future development of the dynamics. Therefore, the dynamics beyond the third generation are more chaotic.

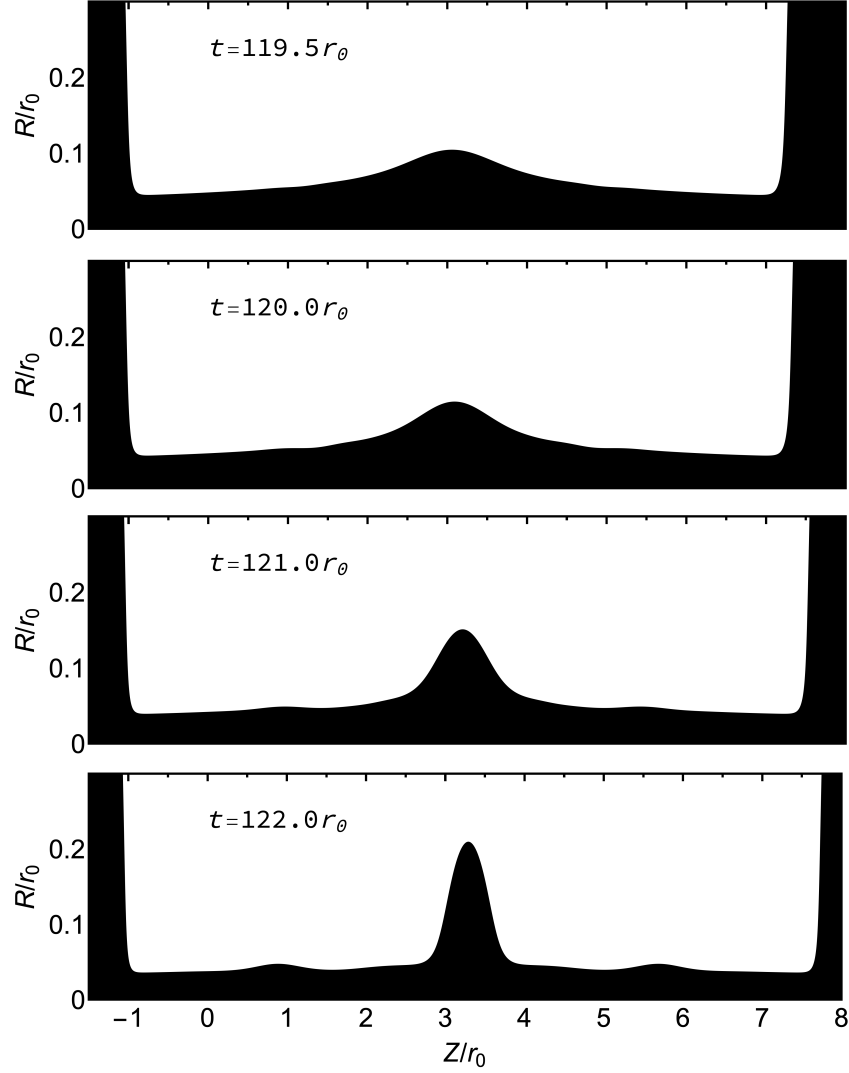


Fig. 4.7 Embedding diagrams of the AH. After the second generation has formed, the string connecting the first and the second generations become non-uniform, which triggers the formation of the third generation.

As we can see from the last panel in Fig. 4.8, the formation of the generations beyond the third are not symmetric about any former generation at all. Moreover, due to the asymmetry of the string segments near both sides of the third generation, the fourth generation has only formed on one side the third generation, but not on the other side. It is also the case that only one satellite is forming for the fifth and the sixth generation. The fifth generation is only forming at the segment between the first generation and the third generation. And the sixth generation is forming at the segment between the second generation and the fourth generation. It is not clear which one will be fully formed at the last stage of our simulation. They are

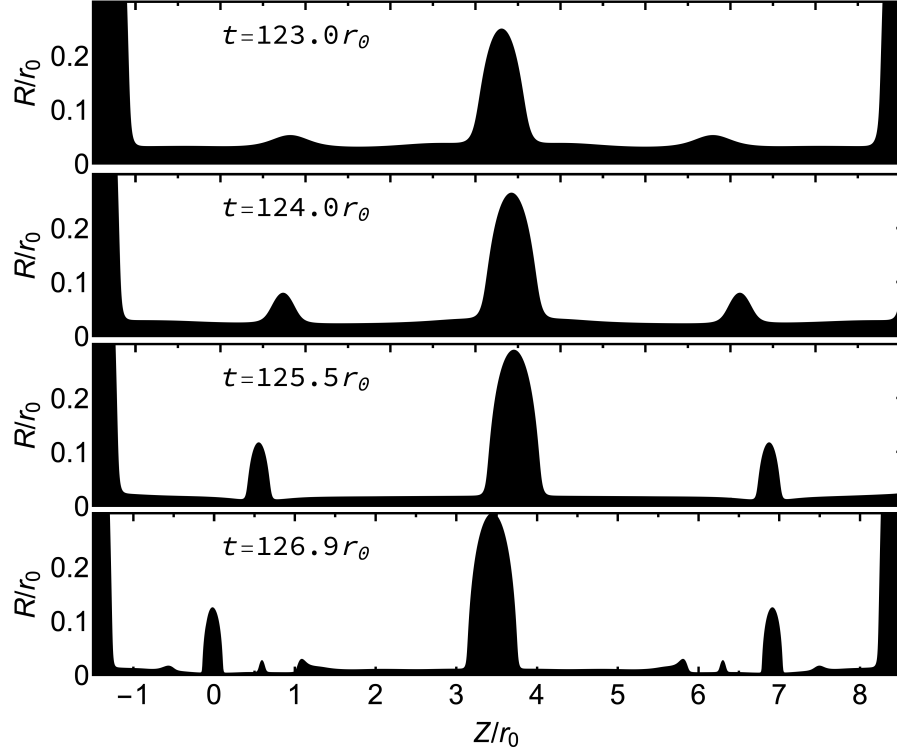


Fig. 4.8 Embedding diagrams of the AH at the late stages. We can see the third generations has fully formed, and the fourth and fifth one are coming up.

all moving towards one of the former generation, which depends on their relative locations. Hence, we can foresee that the satellites will eventually merge with each other.

4.4.4 The evolution of horizon area

It is claimed in [3] that the evolution of the total AH area can be seen as a reasonable approximation to the event horizon and it is non-decreasing over time. By the end of their simulation, the final area $A = 1.369A_0$ saturates the value of an exact 5D BH of the same mass $1.374A_0$, where A_0 is the initial area of the black string. (We recalculate and find that the value of an exact 5D BH of the same mass is actually $1.373A_0$). The horizon area of the unstable black string asymptotes to the area of an asymptotically flat 5D Schwarzschild black hole with the same initial mass. Since this is the entropically favoured solution, they claim that the endpoint of the GL instability is a 5D localised BH in the compact cylinder.

In Fig. 4.9 we display the evolution of the AH area of the $L = 10$ run, which is normalised by the horizon area of the initial unperturbed black string of the length

L and mass parameter r_0 . As we can see from the plot, the ratio is around 1 at the early stage of the simulation. Then it grows rapidly after $t = 80r_0$ when the instability kicks in. This is consistent with the evolution of the horizon in the first two panels of Fig. 4.6 where we observe the rapid expanding of the first blob in its size. After $t = 120r_0$, the growth in the area slows down. This is expected as the further development of the instability has a much smaller scale compared to the first blob. In our simulations, the final area we obtain at the end of our simulation is $A = 1.369A_0$. It seems to tend to the value of an exact 5D BH of the same mass, which is $1.373A_0$. However, we believe that the similarity in the two areas is just coincidence. The black dashed line in Fig. 4.9 is the horizon area for a 5D Schwarzschild BH. The red curve is the corrected area of a 5D Schwarzschild BH in KK space. It indicates the relative area of a slightly deformed single black hole on a circle with the same mass as the unperturbed black string with the same length L . The KK corrections are around 4%, which means it can not be neglected. The AH area is still far away from the corrected area (in red). This suggests that either there is a mass loss during the evolution process or there is a meta-state before it ultimately forms a spherical BH.

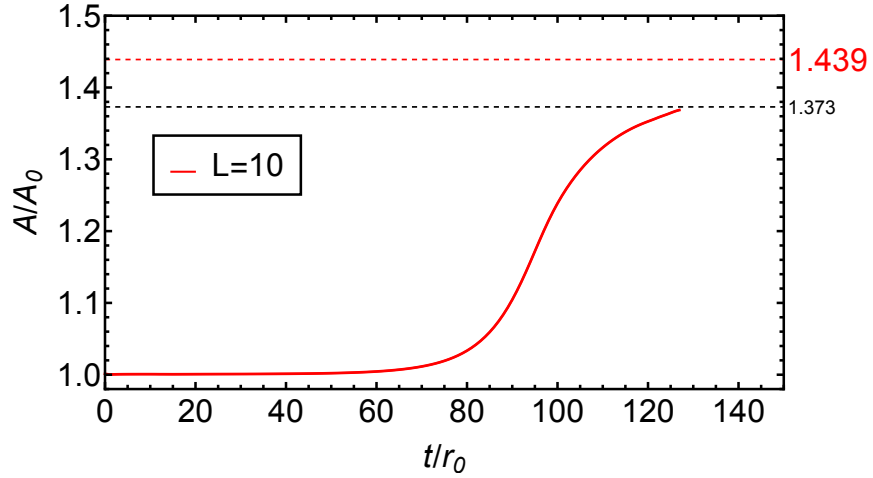


Fig. 4.9 Evolution of the AH area for the unstable black string in 5D with 4D mass parameter $r_0 = 1$ and $L = 10$. The black dashed line is the area for a 5D Schwarzschild BH. And the red dashed line is the corrected area for a 5D Schwarzschild BH in KK space.

From the embedding diagram in Fig 4.4, the 1st generation and 2nd generation are located at an opposite position on the string. The 3rd generations are beyond are moving towards the 1st or the 2nd generation. If the process continues, they will finally join the 1st or the 2nd generation. And it will reach an unstable equilibrium.

The horizon area of two BHs in equilibrium can be found by (3.6.1). By assuming the total mass does not change and approximating the mass ratio from the last stage of the simulation, we obtain $A/A_0 = 1.400$. As shown in Fig 4.4, this provides a better estimate of the final horizon area. There exists an meta-state where there are two BHs located at an opposite position on the cylinder. It is an unstable equilibrium, even A small perturbation would cause the two BHs to merge with each other.

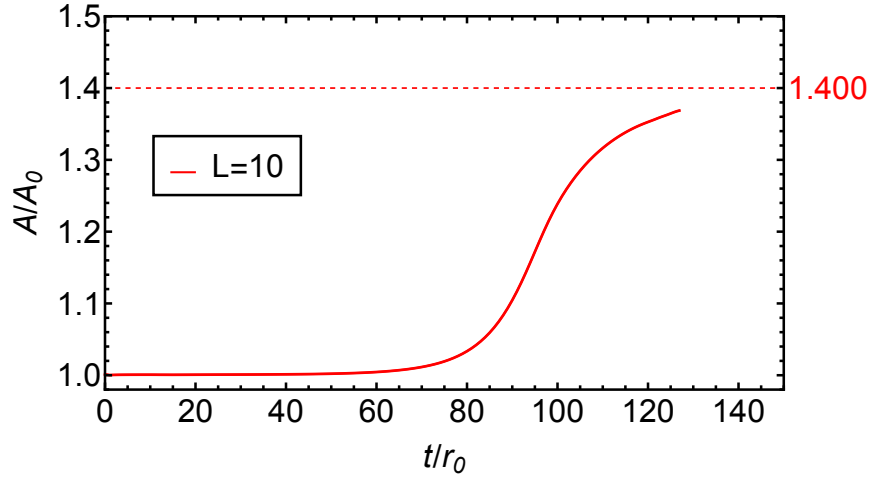


Fig. 4.10 Evolution of the AH area for the unstable black string in 5D with 4D mass parameter $r_0 = 1$ and $L = 10$. The red dashed line is the total area for two BHs.

4.4.5 Properties of the horizon

In this section, we consider in detail the dynamics of the formation of the various generations. The definition of when the various generations have formed is somewhat arbitrary because the unstable black string is continuing to evolve and no portion of the AH is genuinely stationary. Refs. [3] defined the formation of a new generation as the time when a newly forming bulge has a radius which is 1.5 times the radius of the surrounding string segment. In order to get the same table as Tab. 1.1 in [3], we track the following quantities as defined in [3]:

- t_i : the onset of the newly forming i^{th} generation when local instability has reached an "observable level", defined as the time when a nascent spherical region researches an areal radius 1.5 times the surrounding string radius;
- n_s : number of satellite black holes that form per string-segment;
- $R_{AH,f}$: the radii of the i^{th} black holes at the final stage of the simulation;

- $R_{s,i}$: the radii of the corresponding segments;
- $L_{s,i}$: lengths of the corresponding segments.

Using these definitions, we summarise the results from our simulation for the $L = 10$ case in Table 4.1. This table can be directly compared with Table I in [3]. We find our results have good agreement with [3] up to the second generation, although there is an apparent disagreement in the thickness of the string segment $R_{s,2}/r_0$. It may due to the ambiguous definition of $R_{s,2}$ since the string segment has slightly non-uniform thickness between the first generation and the second one (see Fig. 4.7). Beyond the second generation, our results have apparent discrepancies with those in [3]. One reason is that [3] mention large errors in their simulations at this point.

Gen	$t_{0,i}/r_0$	t_i/r_0	n_s	$R_{s,i}/r_0$	$R_{AH,f}/r_0$	$L_{s,i}/R_{s,i}$
1	0	69	1	1	2.04	10
2	98	117	1	0.0586	0.299	136
3	120	122.8	1	0.0343	0.124	109
4	125.95	126.47	≥ 1	0.01	?	264

Table 4.1 Properties of the black string apparent horizon (by 1.5 radius of the surrounding string segment)

With the above definitions of the generations and their data, [3] discovered a time scale between the subsequent generations of the instability beyond the second one, which is approximately $1/4$. However, in our data, we do not find evidence of such a global time scale relating the subsequent generations in Table 4.1 for the $L = 10$ run. Specifically, our results show that the time for the first generation to be observed is $T_0/r_0 \approx 69$. The time for the second generation and third generation to form is $T_1/r_0 \approx 48$, $T_2/r_0 \approx 6$, $T_3/r_0 \approx 3.7$, respectively. The time-scale for each subsequent instability to form varies. In fact, we believe that there can not be such a global time scale. The reason is that that the development of the instabilities beyond the second generation is a rather chaotic process, which we have already seen in previous section. Our simulation results indicate that the late-time dynamics is not only controlled by the GL instability but also the local dynamics of the bulges and the string segments.

To better discuss our results, we find it useful to define a set of different quantities. First, we plot the time derivative of the logarithm of the radius of the bulges

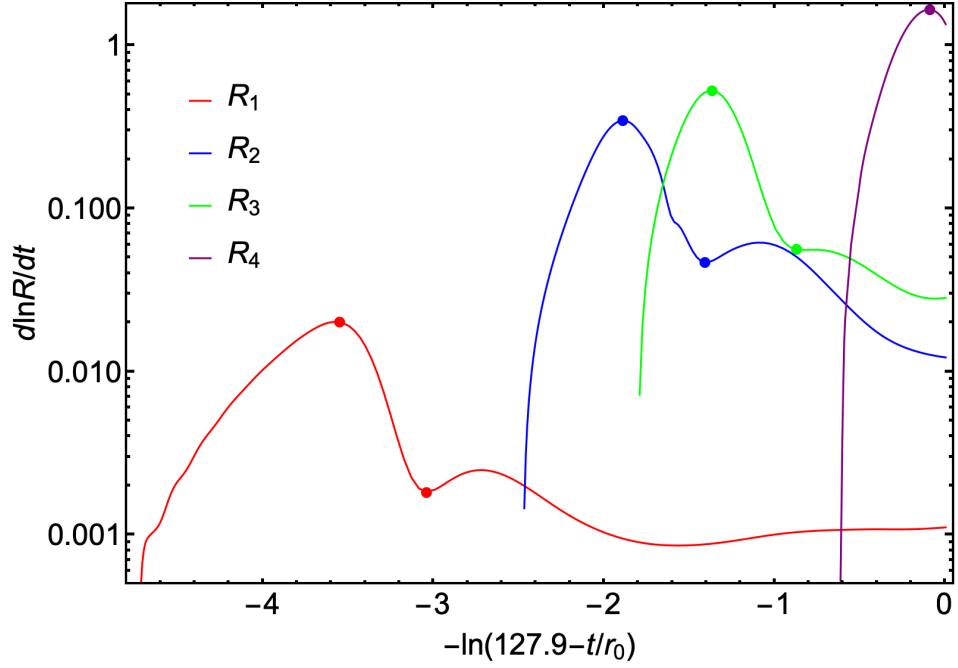


Fig. 4.11 Time derivative of the logarithm of the equatorial radius for each of the generations for the $L = 10$ case as a function of time.

corresponding to the first four generations as functions of time for the $L = 10$ black string in Fig. 4.11. We define the following quantities.

- $t_{p,i}$: time at which the growth of the i -th generation is the fastest compared to its size, corresponding to the absolute maxima in Fig. 4.11 (marked with a dot);
- $t_{n,i}$: time of formation of the i -th generation by the local minimum in Fig. 4.11 (also marked with a dot);
- $R_{AH,i}$: the radii of the i^{th} black holes by the end our simulation.
- $R_{s,i}$: the radii of the corresponding segments;

We summarise the properties of different generations that we have managed to observe from the above definitions for $L = 10$ run in Table 4.2.

With these new definitions, we find that the time for the each generation to be observed is $T_0/r_0 \approx 107$, $T_1/r_0 \approx 17$, $T_2/r_0 \approx 2$, $T_3/r_0 \approx 2$, respectively. There is no global time scale relating the subsequent generations. The formation time for each generation, i.e. $T_{f,i} \equiv t_{n,i} - t_{p,i}$, is approximately $T_{f,1}/r_0 \approx 14$, $T_{f,2}/r_0 \approx 2.5$ and $T_{f,3}/r_0 \approx 1.6$, respectively. The whole process is speeding up.

Gen.	$t_{p,i}/r_0$	$t_{n,i}/r_0$	n_s	$R_{s,i}/r_0$	$R_{AH,f}/r_0$	$R_{s,i}/L_{s,i}$
1	93	107	1	1	2.04	0.1
2	121.3	123.8	1	0.0162	0.299	0.023
3	124.0	125.6	1	0.0539	0.124	0.016
4	126.8	?	$\geq 1/1$	0.0185/0.0165	?	0.0076/0.012

Table 4.2 Properties of the black string apparent horizon (by first negative peak of the radial velocity)

The overall dynamics fully respects the \mathbb{Z}_2 symmetry of the problem. When the first generation has fully formed, the string segments surrounding it becomes uniform. This piece of uniform string segment is shrinking over time and eventually become unstable, resulting in the formation of the next generation of the GL instability. The location where the first bulge appears depends on the initial data we choose. Since the initial data we choose has no net momentum along the string direction, the second generation would form exactly at the centre of the string segment, which is indeed the case from our simulation results.

4.4.6 Velocity profile

To obtain a qualitative idea of the movement of different bulges, we consider a particular null ray that is comoving with the AH,

$$V = \partial_t + \dot{z}\partial_z + (\dot{x} + h'\dot{z})\partial_x, \quad (4.24)$$

where the dot $\dot{}$ denotes the derivative with respect to the parameter t and \dot{x} and \dot{z} correspond to the tangential velocity (v_{\parallel}) and orthogonal velocity (v_{\perp}) of the null ray with respect to asymptotic observers at rest.

We plot the tangential velocity and the orthogonal velocity at the last stage of our simulation in Fig. 4.12. The velocity profile provides us some measure of the motion of different portions on the AH with respect to a frame that is at rest with respect to asymptotic infinity. First, the velocity profile shows that the tangential velocities are much larger than the orthogonal ones. In addition, it also shows that the newly forming generations are accreting mass from the surrounding string segments. Meanwhile, they are moving towards one of the previous generations, as the orthogonal velocities are non-zero. These results are consistent with the local dynamics of the blobs described in previous section.

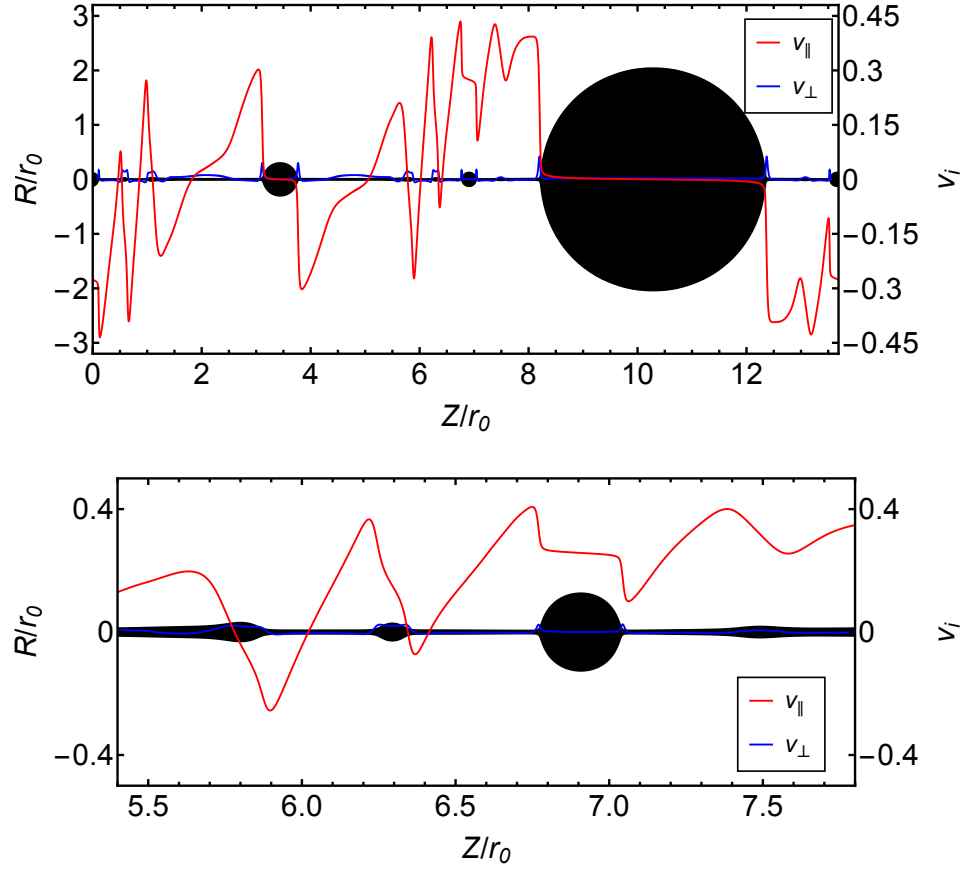


Fig. 4.12 The tangential velocity and radial velocity at the final stage of the evolution of the $L = 10$ run.

The development of the late-time dynamics is not only govern by the local thicknesses of the string segments but also affected by the motion and growth of the bulges. As a result, some string segment becomes thinner than the others, which means it has larger growth rate of the local GL instability. Therefore, the local motion of the bulges accelerates the approach to the pinch off in finite asymptotic time.

4.4.7 Approach to the singularity

In [3], it is demonstrated that the horizon of the black string will pinch off in finite asymptotic time. First, they claim that there exists a (global) time scale relating subsequent generations so that the time to endpoint can be found by (4.2). Second, the minimum of the areal radius of the black string follows an approximate scaling law (4.25) as described in previous section. Third, the slope of the evolution of the proper length in the logarithmic plot indicates that the late time dynamics develops into a fractal structure. This is a consequence from the self-similarity in

the horizon dynamics. Although we do not find such a global time scale supporting the self-similar nature of the instability, we do find the minimal radius of the string follows a similar scaling law and the proper length has a similar slope in the late time. Therefore, our simulation results support that the pinch off is governed by some scaling law. In this section, we present our results in detail about the horizon properties close to the pinch off.

By fitting our data into the scaling law,

$$R_{min} = \alpha(t_c - t), \quad (4.25)$$

we can extract the values of α and t_c/r_0 . For the $L = 10$ case, $\alpha = 0.0052$ and $t_c/r_0 = 127.9$. This is more or less consistent with the slope found in [3]. By using the values found for α and t_c , we display the minimum areal radius of the string in the logarithm plot in Fig. 4.13. This figure can be directly compared with Fig. 1.4 in [3].

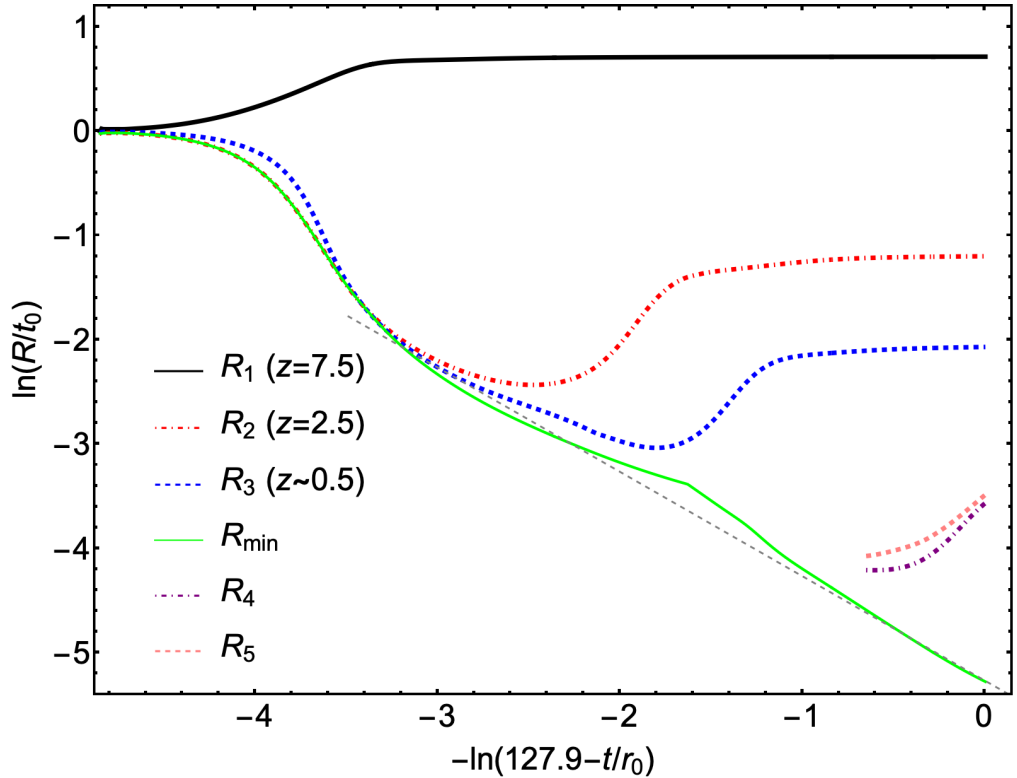


Fig. 4.13 Logarithm plot of the areal radius R of the AH vs the time to the pinch off for the $L = 10$ run. We also display the evolution of the radius of several generations and the minimal radius on the string.

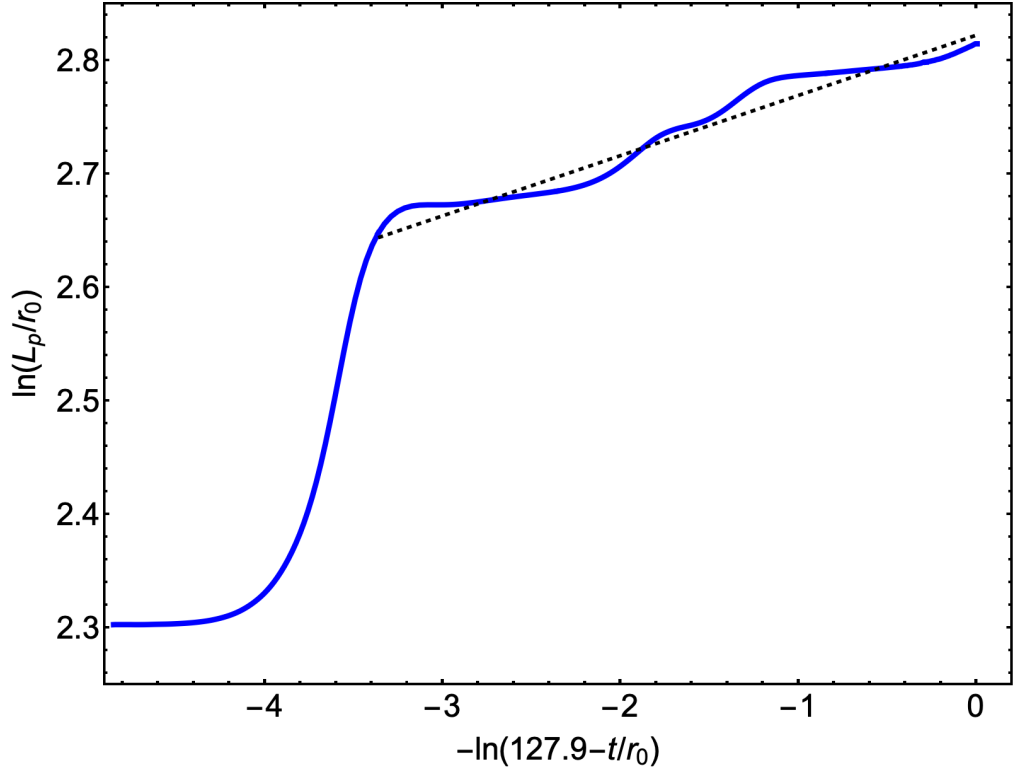


Fig. 4.14 Plot of the proper length vs. time in logarithmic coordinates for $L = 10$ run. The slope of the dotted line, which is a linear fit to the late-time data, is ~ 0.053 .

We also display the evolution of the proper length of the string on a logarithmic scale in Fig. 4.14, where the slope is ~ 0.053 at the late-time dynamics. This figure can be directly compared with Fig. 1.5 in [3].

4.4.8 Mode behaviour

To better understand what dominates the dynamics at different times, we analyse the mode behaviour of different string segments at the late stage of each generation. Following [3], we decompose the string radius $R_{AH}^i(t, x)$ around the i^{th} generation in the coordinate region covering the corresponding string segment for the $L = 10$ case by the following expansion

$$R_{AH}^i(t, z) = c_0 + \sum_{k=1}^{\infty} c_k \sin\left(\frac{k\pi z}{L_{s,i}}\right), \quad (4.26)$$

where $L_{s,i}$ is the length of the interested domain corresponding to the i^{th} generation. We extract the Fourier coefficients c_k that capture the "strength" of the various GL

harmonics. We display the values of c_k/c_0 as functions of time for $k = 1, 3, 5$ in Fig. 4.16, 4.18 and 4.20 for the different string segments between each generations. We only display the odd coefficients as the even coefficients are several orders smaller than the odd ones.

For the first generation, which is triggered by the initial data and numerical errors, we decompose the areal radius $R_{AH}^1(t, x)$ in the whole domain $x \in [0, 10M]$ at $t \in (0M, 68M)$. It is the period right before the first generation becomes distinguishable (see Fig. 4.15). We extract the coefficients c_k up to $k = 6$. In Fig. 4.16, we only plot the odd coefficients c_1, c_3, c_5 as the even ones are a couple of orders smaller. There is a tweak at the beginning resulting from the initial perturbation we use. As we can see from Fig. 4.16, the first coefficient dominates the other ones at the initial stage during the formation of the first generation.

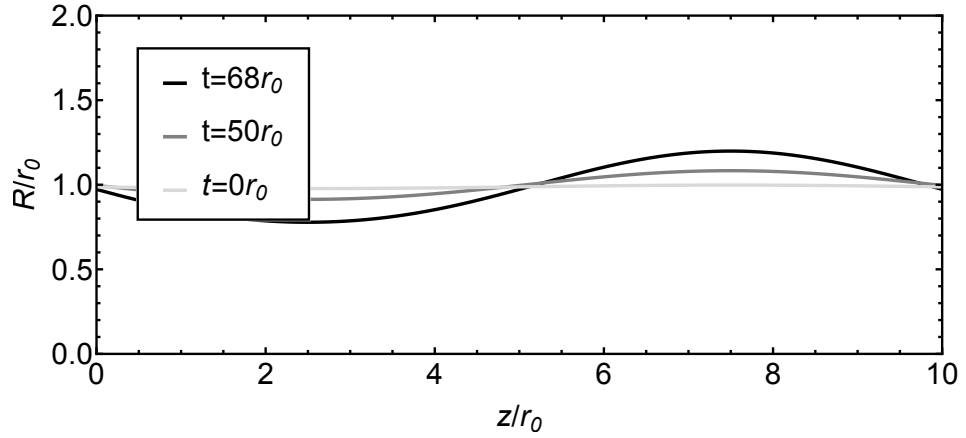


Fig. 4.15 The evolution of the AHs at $t=0, 50, 68$. This is the period before the first generation is about to form.

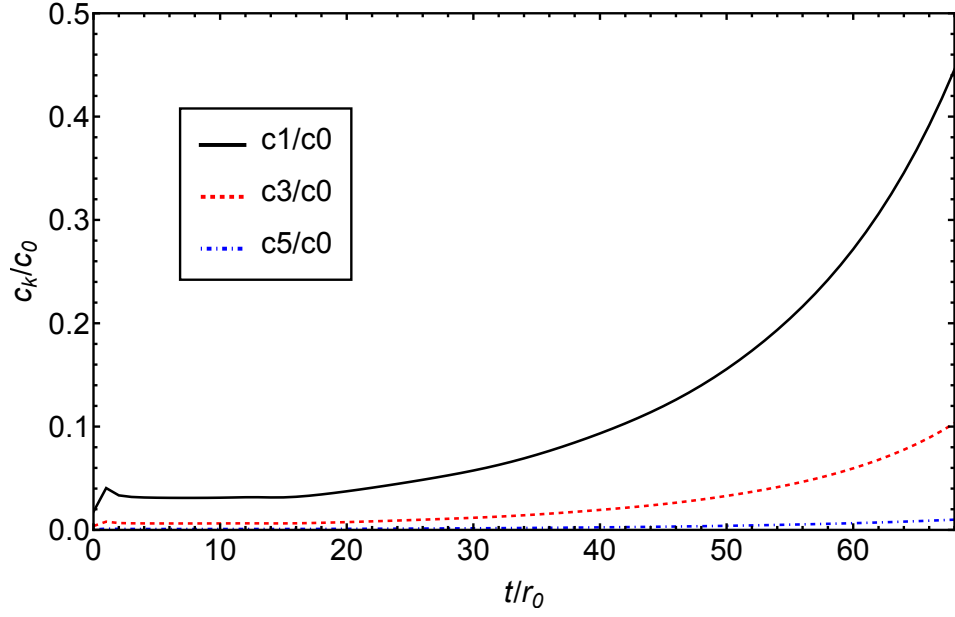


Fig. 4.16 Values of the expansion coefficients for the whole string.

For the second generation, we decompose $R_{AH}^2(t, x)$ in $z \in [0, 5r_0]$ which covers the second string segment and look at the areal radius at $t \in (100M, 117M)$ (see Fig. 4.17). We plot the odd coefficients $c1, c3, c5$ in Fig. 4.18. This figure can be compared with Fig. 1.6 in [3]. In this case, the first coefficient also dominates the other ones at the initial stage during the formation of the second generation.

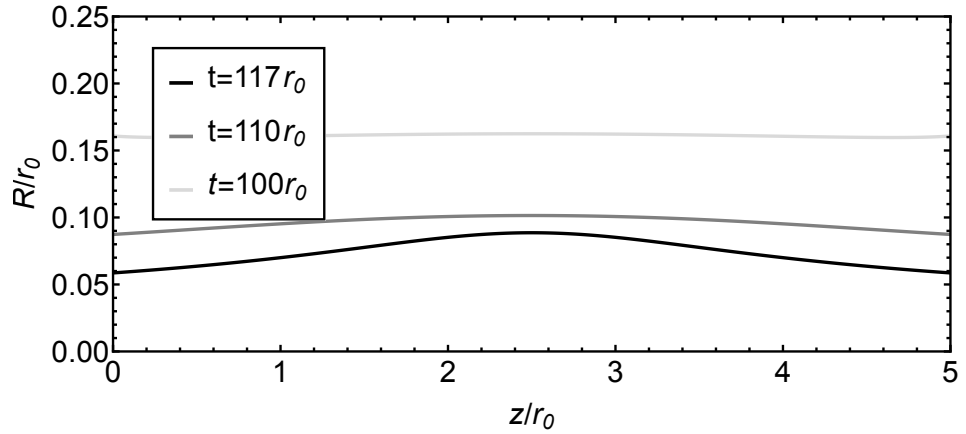


Fig. 4.17 The evolution of the AHs at $t=100, 110, 117$, when it is at last stage of the formation of the first generation, but before the second generation has fully formed.

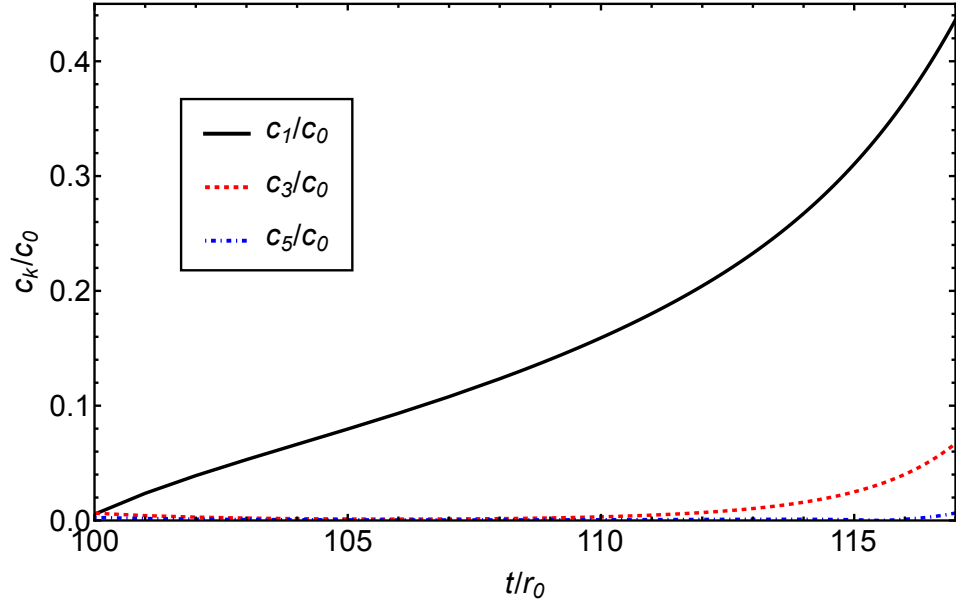


Fig. 4.18 Values of the expansion coefficients for the string segment corresponding to the 1st generation.

In late time dynamics, the string segments are not uniform any more. The fitting results are not as good as previous ones by expansion with sine series. We find it is better to decompose the string radius with cosine series (4.27).

$$R_{AH}^i(t, x) = c_0 + \sum_{k=1}^{\infty} c_k \cos\left(\frac{k\pi z}{L_{s,i}}\right), \quad (4.27)$$

Cosine series work quite well, especially when the string segments are non-uniform (see Fig. 4.19).

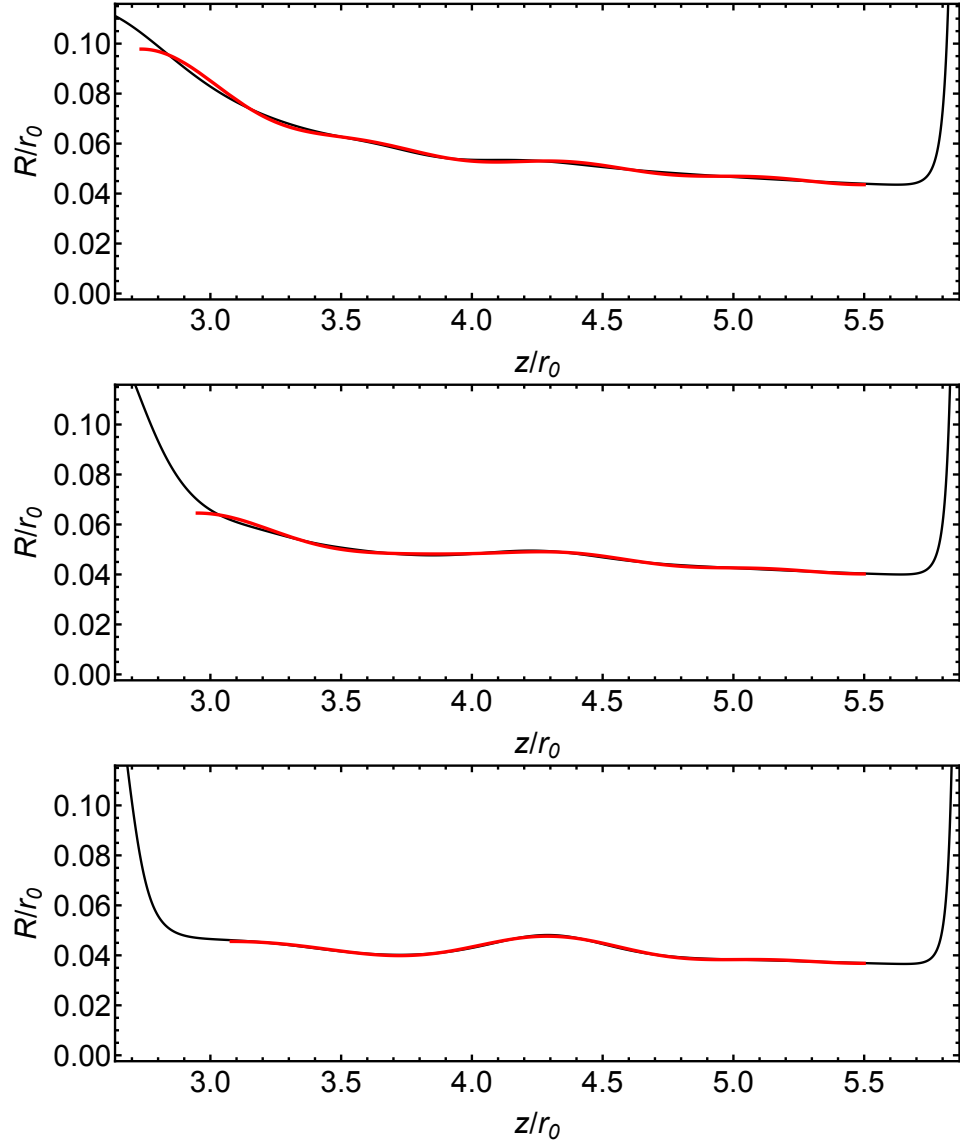


Fig. 4.19 The evolution of the AHs at $t=120, 121, 122$, when it is at last stage of the formation of the second generation, but before the third generation has fully formed. The fitted curves are plotted in red.

For the third generation, we decompose $R_{AH}^3(t, x)$ in the region around $z \in [3r_0, 5.5r_0]$ and extract the coefficients c_k up to $k = 7$. We plot the coefficients in $t \in (120M, 122.8M)$ in Fig. 4.18. The first coefficient also dominates the other ones at the initial stage during the formation of the third generation, but it soon drops below all the other coefficients. Meanwhile, the other coefficients, c_2 and c_4 in particular, are growing over time and the even modes become larger than the odd ones. Several modes are growing at the same time is what expected, as at this stage of the evolution, the dynamics become more chaotic.

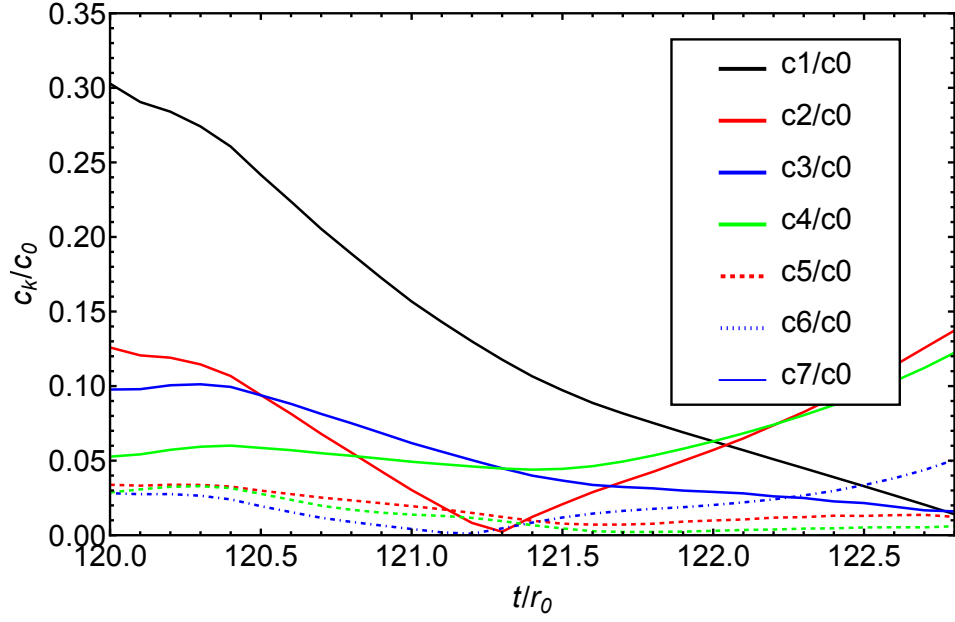


Fig. 4.20 Values of the expansion coefficients for the string segment corresponding to the 3rd generation.

When the third generation has formed, the string segments on the left and right of it are not symmetric any more (see Fig. 4.21). As a result, it is better to analyse them separately.

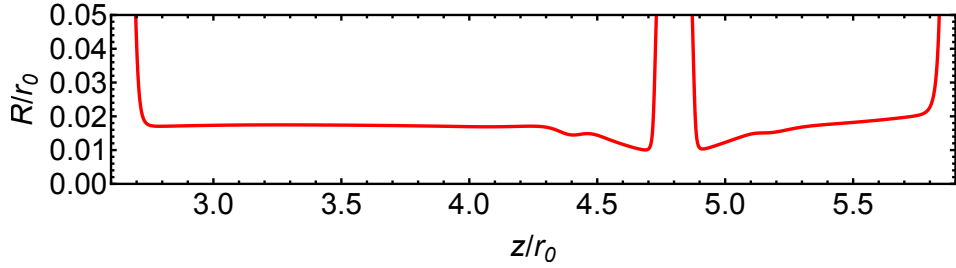


Fig. 4.21 The AH at $t=126$ (in red).

We decompose $R_{AH}^4(t, x)$ in $z \in [2.8r_0, 4.6r_0]$ with cosine series and plot the coefficients in $t \in (125.9M, 126.4M)$ in Fig. 4.23. The first coefficient also dominates the other ones at the initial stage during the formation of the fourth generation, but it soon drops while the other coefficients, c_2 , c_3 and c_4 in particular, are growing over time. At this stage of the evolution, several even and odd modes are growing at the same time. This is what expected, as at this stage of the evolution, the dynamics become even more chaotic.

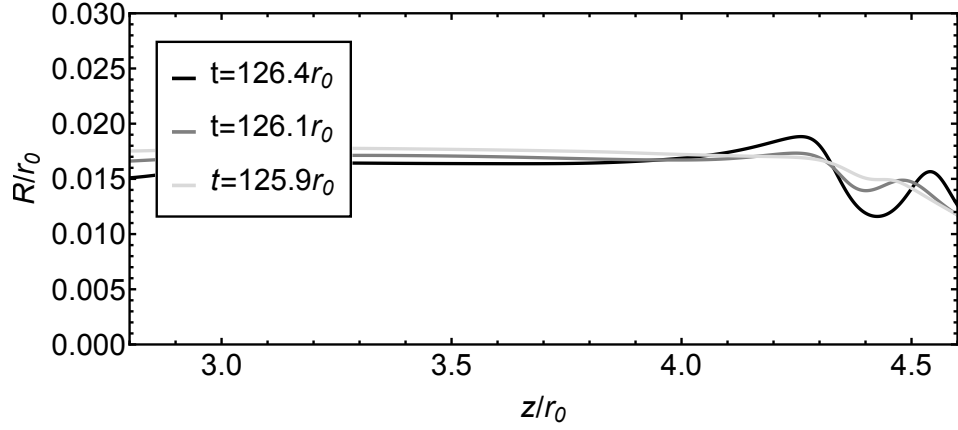


Fig. 4.22 The evolution of the AHs at $t=125.9$, 126.1 and 126.4 for z in $[2.8, 4.6]$.

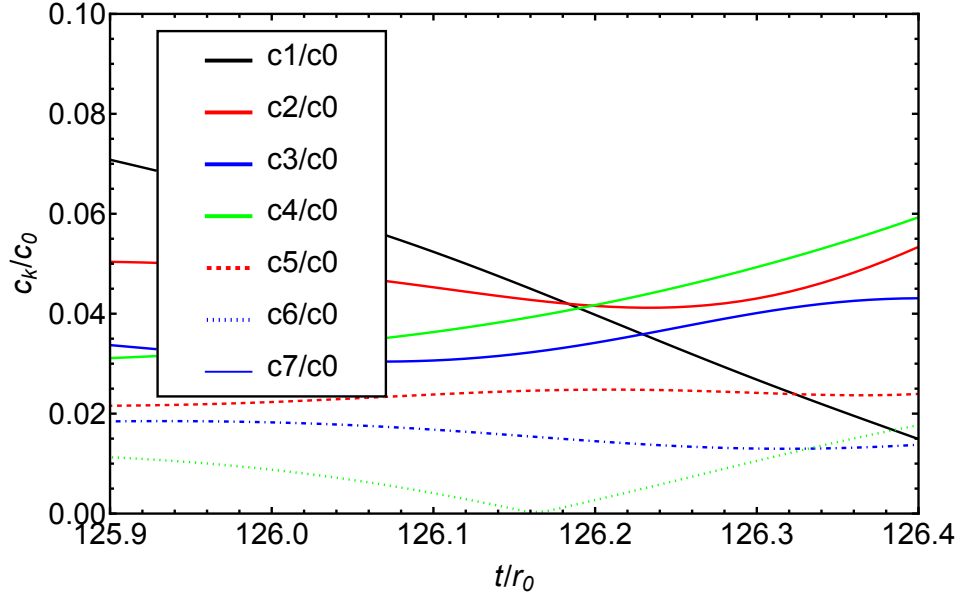


Fig. 4.23 Values of the expansion coefficients for the string segment on the left corresponding to the 4th generation.

We decompose $R_{AH}^4(t, x)$ in $z \in [5r_0, 5.7r_0]$ with cosine series as the segment is non-uniform. We plot the coefficients in $t \in (125.9M, 126.4M)$ in Fig. 4.25. The first coefficient also dominates the other ones and is growing over time. This is because the string segment becomes less uniform over time. The third coefficient is growing over time. This is expected as there is likely to form only one blob, i.e. the fifth generation, on this piece of string segment (see Fig 4.24).

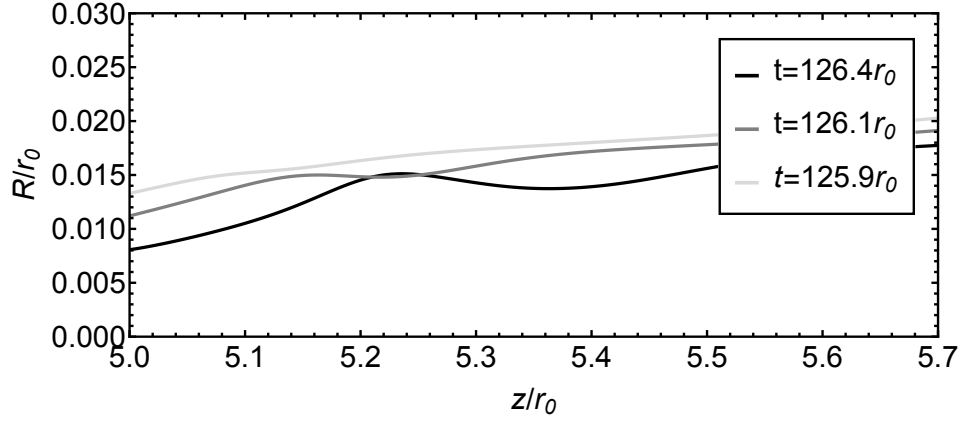


Fig. 4.24 The evolution of the AHs at $t=125.9$, 126.1 and 126.4 for z in $[5, 5.7]$.

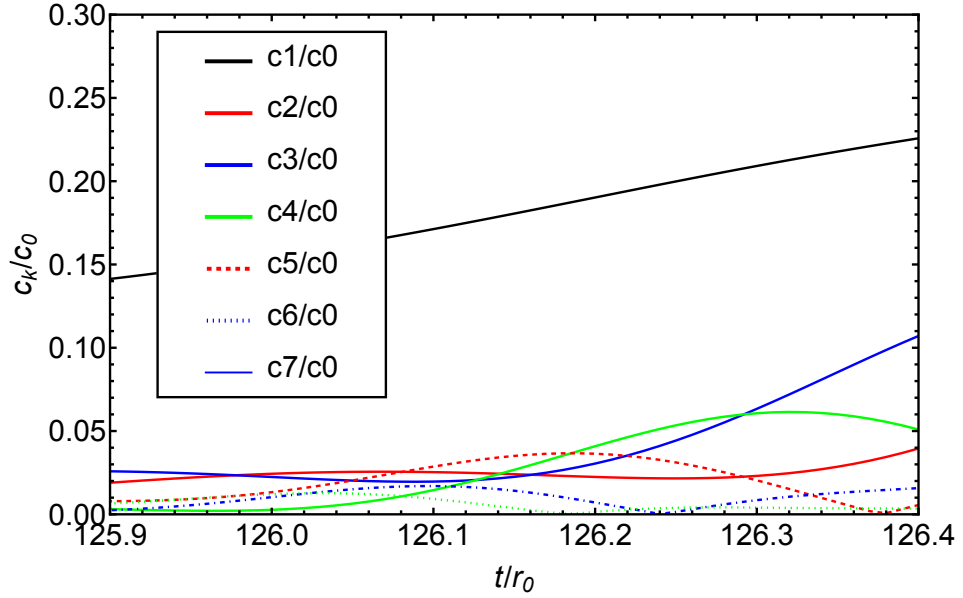


Fig. 4.25 Values of the expansion coefficients for the string segment on the right corresponding to the 4th generation.

4.5 Numerical tests

In this section we present the main test results that we have done in order to achieve stable simulations of the black strings.

First, we need to ensure that the outer boundary does not affect the inside physics. This is usually made possible by putting the outer boundary far away enough, with the consequence of increasing computational cost. We start by simulating the unperturbed black string on a domain that has lengths L_{outer} in the radial direction

and periodic length $L = 10r_0$. At the coarsest level the mesh spacing is $1/4$. This means we have 40 points in the string direction at the coarsest level initially. We use in total 5 additional levels initially, each of which is refined by $2 : 1$ ratio in both string and spatial direction. This is to guarantee that there are at least 40 grid points in the radial direction at the horizon. We keep the resolution while range L_{outer} from $80r_0$, $160r_0$ to $256r_0$ and run the simulations up to $t = 250r_0$. The simulation results indicate that for the $80r_0$ and $160r_0$ runs, the outer boundary would have some effects at $t \sim 80r_0$ and $t \sim 150r_0$. Whilst for the $256r_0$ run, the effects appears at $t \sim 240r_0$. Hence, $256r_0$ would be enough for our purposes, considering that the pinch off of the horizon happens before $t = 200r_0$.

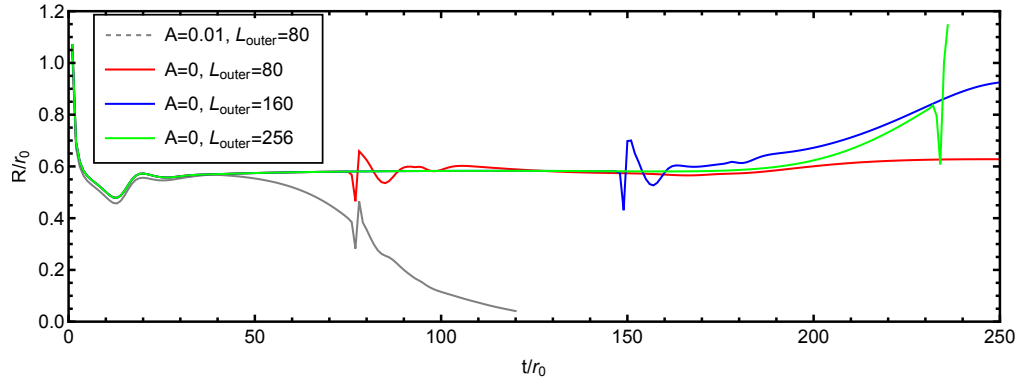


Fig. 4.26 Test results for the outer boundary at 80, 160 and 256, respectively. The glitch indicates that the outer boundary starts to have some effects on the inside physics.

Then, we test with medium and high resolutions with $L_{outer} = 80$. The glitch happens at the same time, which indicates that increasing the resolution does not change the time for the outer boundary to take effects in the above settings.

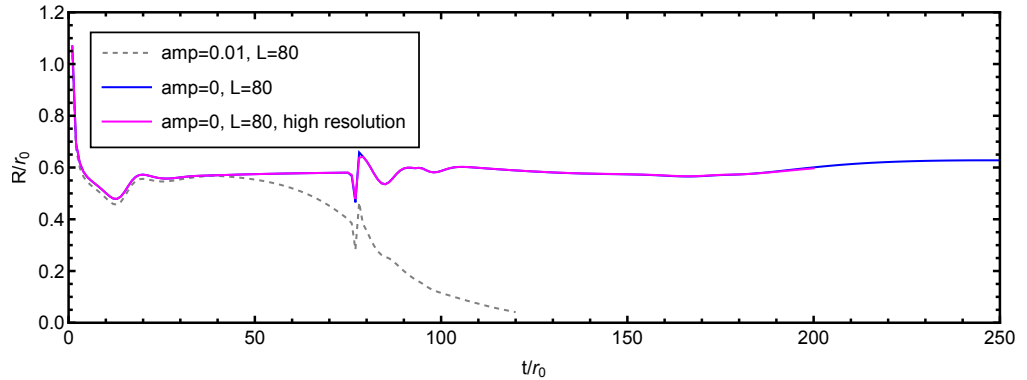


Fig. 4.27 Test results from the medium and high resolution respectively. The glitch indicates when the outer boundary starts to have some effects on the inside physics.

In theory, the horizon area should be non-decreasing. In our simulations, it turns out to be slight decreasing at the final stage of the evolution due to numerical error. To minimise this effect, we have test different combinations of parameters including dissipation factor (Sigma), the kappa's. We find two sets of parameters ($\sigma = 0.8, \kappa_1 = 0.1, \kappa_2 = 0$ and $\sigma = 1.5, \kappa_1 = 0.37, \kappa_2 = -0.8$) that has the minimal decrease in the horizon area, $\sim 0.05\%$ and $\sim 0.002\%$, which is within tolerance. We typically use the latter in our simulations.

For the $L = 10$ case, we carry out runs with different resolutions and monitor the AH area. In our simulation, we typically use the medium resolution which has coarsest grid spacing of $h = 0.25r_0$. Then we run two extra runs with lower and higher resolutions of $\Delta_{\text{low}} = \frac{10}{7}h$ and $\Delta_{\text{high}} = \frac{2}{3}h$, respectively. We have tried other even lower or higher resolutions. However, the higher ones, e.g. $\Delta_{\text{low}} = 1/2h$, could cost too much computational resources and thus is not feasible. The low resolution cannot be too low, e.g. $\Delta_{\text{low}} = 2h$, because the numerical error would be soon out of control and the simulation would crash shortly after the formation of the first generation.

The convergence test results are illustrated in Fig. 4.28. Due to the limitation of computational cost, we only evolve the low and the high resolution runs for a limited time. This plot shows that the order of convergence during the evolution is roughly 3. This is what we would expected.

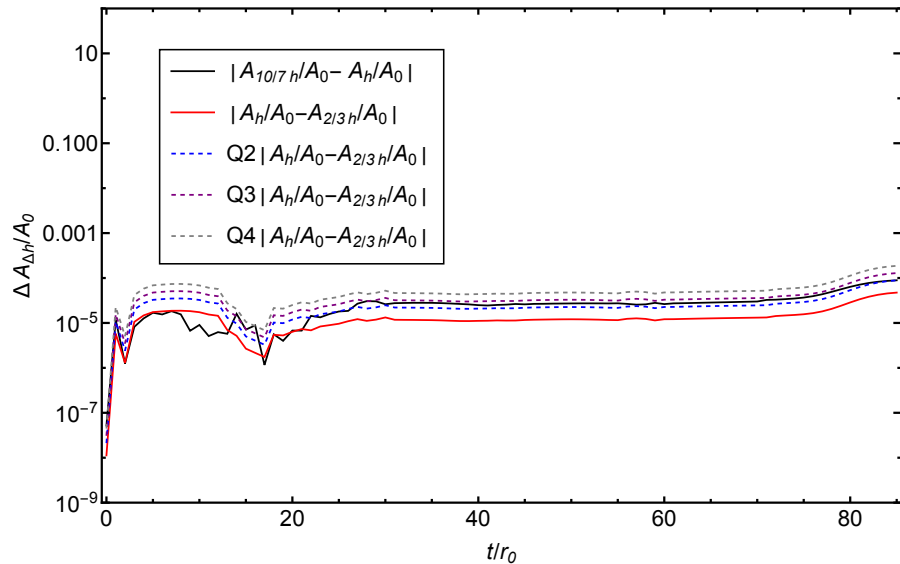


Fig. 4.28 Convergence test for the AH area for the $r_0 = 1$, $L = 10$ black string. The medium resolution run has spacing $h = 0.25r_0$ in the coarsest grid level. This plot shows that the order of convergence is roughly three. The computational cost of the high resolution run limited the time of the tests.

We will provide more detailed results of the numerical tests in the Appendix [B](#).

4.6 Discussion

In our study, we not only reproduce the main results of [3] with a different and independent formulation, but also extend the simulations further with better resolution. We confirm that in the development of the GL instability, the horizon at the late stage can be described by a sequence of black holes connected by string segments of various sizes. The string segment connecting two black holes is itself unstable to GL instability. Thus the process is repeating itself in different scales. Up to the second generation our results agree quite well with the results in [3]. Moreover, we improve the simulation results for the late-time dynamics. In particular, our results respect \mathbb{Z}_2 symmetry of the problem during the whole evolution. That is, the dynamics are fully symmetric about the first generation.

However, we do not find any evidence to support the global time scale that relates the subsequent generations as claimed in [3]. Instead, we argue that there does not exist such a time scale. The reason is that the string segments beyond the second generation become non-uniform, which gives rise to unequal tension along the string, causing the local movement of the future generations. In fact, the late-time dynamics depend on two factors: the local GL instability and the local dynamics of the bulges. Although we do not find the time scale, the basic picture of the instability still holds. We find the minimal string radius follows a similar scaling law and we confirm the pinch off of the horizon in finite asymptotic time. This provides further evidence against the WCCC. Eventually, we evolve the system with higher resolution up until the full formation of the fourth generation. The fifth and sixth generations are also about to form. Due to the exponentially increasing computational cost, we were not able to continue the simulation further within the allocated resources we had. If in the future, given more computational resources, we should be able to continue the simulation and push it even closer to the pinch off. This helps to understand the nature of the singularity. In summary, our results provide a better picture of the late-time dynamics of the GL instability and more details about the late-time dynamics close to the pinch off.

The above conclusions are made from the simulation results of the $L = 10$ run, where the particular length was chosen for a direct comparison of our results with [3]. Therefore, it would be interesting to see whether they are universal properties for strings with different thickness. In the next chapter we will explore strings

with different lengths and masses, in order to obtain a more general picture of the development of the GL instability.

Chapter 5

Results from Strings with Different Lengths

In the previous chapter, we have presented the simulation results for the $L = 10$ string with the GRChombo code. With this particular length, we have seen that the horizon dynamics develops into a self-similar structure, which leads to the pinch off of the horizon in finite asymptotic time. Furthermore, we discover that the minimal string radius follows a scaling law. To determine whether these properties hold in general, we extend the simulations to strings with different lengths and masses. In this chapter, we present the results from the numerical simulations of strings with various lengths that we have explored and provide a more general picture of the development of the GL instability.

To extend the simulations to strings with different lengths, we fix the mass parameter of the parent 4D Schwarzschild black hole to $r_0 = 1$ and vary the initial string length L . We consider four different runs with $L = 8, 10, 12, 16$ respectively. We solve the EFE using the CCZ4 formulation as described in the previous chapter. The computational cost increases with the initial length of the string, as for larger L , the computational domain are larger. We aim to push each run as close to the singularity as possible.

Our simulation results support that, for all the cases we have considered, the GL instability of a perturbed black string evolves into a dynamical process that can be described as a quasi-stationary sequence of spherical BHs connected by thin and black string segments on different scales. Each string segment itself is thin and unstable to the GL instability. The position and the time of the formation of the

first generation is sensitive to the choice of initial conditions but the subsequent evolution is universal for all runs. Hence, in this chapter, we will concentrate more on describing the dynamics of the unstable black strings and the evolution of the AH beyond the first generation.

In Sec. 5.1, we present the horizons from the last step of our simulations for all the four runs. The evolution of the horizon areas over time for different runs is presented in Sec. 5.2. Sec. 5.3 gives a summary of the horizon properties, including the formation time and the number of satellite black holes for each generation in different runs. In Sec. 5.4, we provide more details about the satellite formation. We discuss the approach to the singularity in Sec. 5.5.

5.1 The geometry of the horizons

In Fig. 5.1 we display the embedding diagrams of the AHs taken at the last stage of our four simulations, for the $L = 8, 10, 12, 16$ runs from top to bottom. The normalised Kretschmann invariant K are superposed on the horizon (in red). The relative position of the formation of the first generation is sensitive to the choice of initial conditions. For all the four cases we considered, we confirm that the local structure of the horizon can be described by sequence of spherical BHs connected by black strings in different scales. The string segments connecting the blobs are themselves unstable to the GL instability. This results in a self-similar process of the development of the GL instabilities on different scales. The main results are consistent with that in the $L = 10$ case described in [3]. Hence, we can conclude that this self-similar process is universal during the evolution of the GL instability of black strings. Moreover, we confirm that the values of K is essentially 1 along the string segments of the AH. And it is approximately 6 near the centre of the blobs. This is the case for all the simulations of different L 's that we have explored.

An animation of the evolution of the AH for the $r_0 = 1$ and $L = 10$ black string can be found [here](#) ¹; other animations corresponding to strings of different lengths and thickness can be found in the [GRChombo YouTube channel](#) ².

¹youtu.be/Mc-jzvn_hto

²youtube.com/playlist?list=PLSkfizpQDrcbUn2JNjkL0LKcy9k_oGQ_-

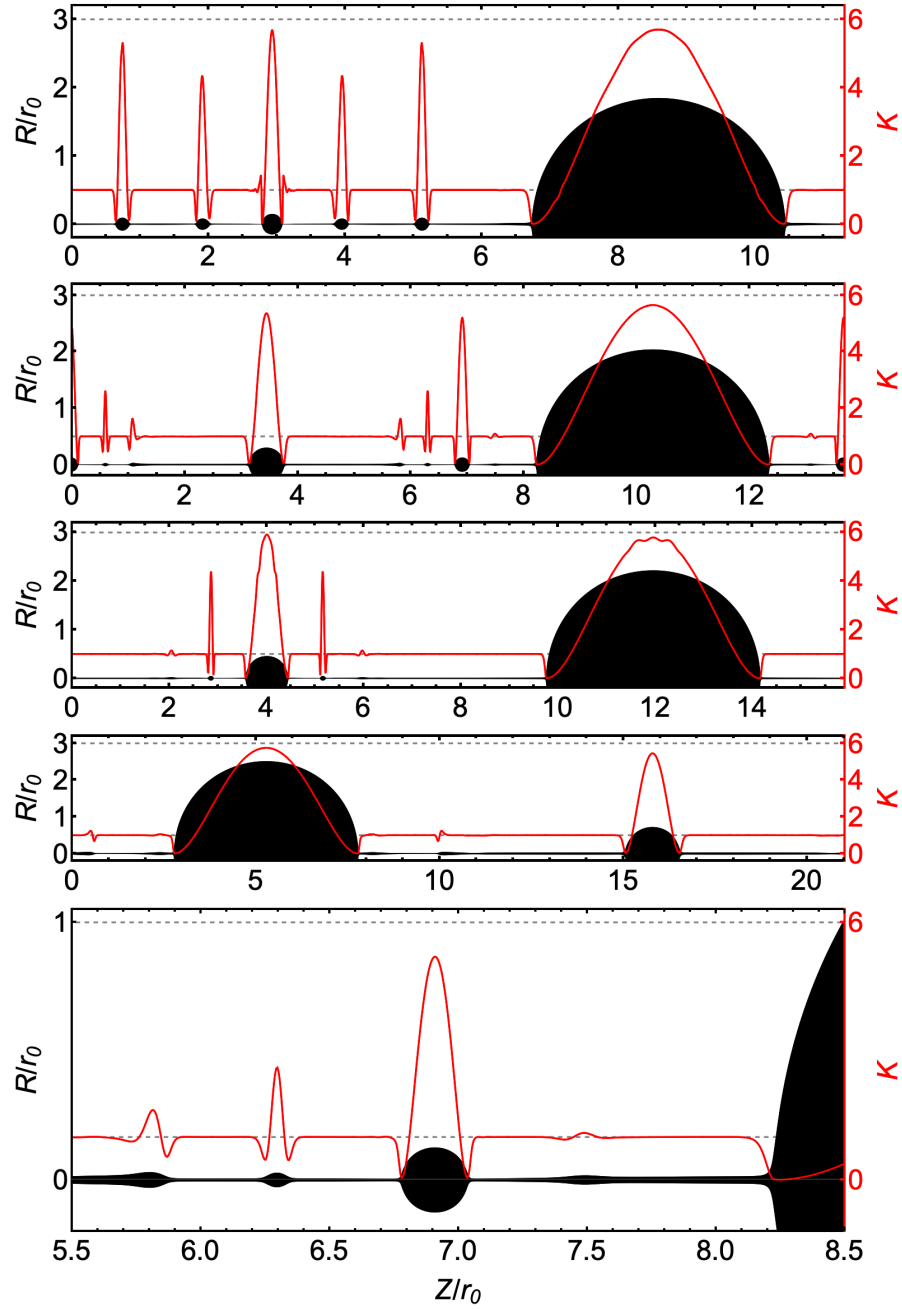


Fig. 5.1 Top: Embeddings of the geometry of the AH at the last stage of our simulations for $L = 8, 10, 12, 16$, from top to bottom; the corresponding length along the Z direction is 11.32, 13.69, 15.90 and 21.03 in units of r_0 , respectively. For better visualisation, we have rescaled the height of the plots so that all of them have the same width while maintaining the proportions of the embeddings. The induced Kretschmann invariant is superposed to the AH in red. Bottom: zoom in of the thinnest part near the second generation on the string in the $L = 10$ case, where we can see the third and fourth generations are obviously visible. The fourth is growing and moving towards the first blob. The fifth generation is about to form as well.

5.2 The AH area

During the evolution, we track the AH area for each simulation by the method that has described in the previous chapter. For the different values of L and masses we consider, the leading KK corrections are all non-negligible. In fact, the leading KK corrections to a 5D Schwarzschild black hole [4] are approximately 6%, 5%, 4% and 3% of their respective asymptotically flat values, corresponding to the $L = 8$, $L = 10$, $L = 12$, and $L = 16$ cases respectively.

For each run, we plot the AH area during the evolution in Fig. 5.2, along with the area for the 5D KK black hole with the same mass as the unperturbed black string. As we can see, the difference is smaller for the $L = 8$ case, but for larger values of the L , the final area of A/A_0 are even further away from the area of a single KK black hole with the same initial mass. In particular, for $L = 16$ the difference is more than 9%. The reason for this huge disagreement is that we only consider the area for a single 5D KK black hole but ignore the fact that there is a meta-state of the evolution, where the second generation also takes a considerable amount of the total mass of the system. Indeed, the second generation takes a considerable amount of the total mass. Fig. 5.3 indicates that the radius of the second generation bulge has $10\% \sim 30\%$ of the radius of the first generation bulge for different L 's. Especially for larger L 's, the second generation has larger radius/mass ratio compared with the first blob. Hence, its contribution to the final area should also be taken into account. Therefore, we could get a more accurate estimate by calculating the total area contributed by both the first generation and the second one.

We estimate the total area of the two KK black holes using the same radii as the first and second generation bulges at the end of our simulations by (5.1). The total mass of them maintains the same as the initial unperturbed black string. In Fig. 5.2, the total areas normalised by the initial mass are shown in the dotted lines. It indeed is a better estimate, and the agreement gets better when L increases.

$$A_{total} = A_1 + A_2, \quad A_i = 2\pi^2 r_i^3 \left(1 + \frac{3\zeta(2)}{8\pi^2} r_i^3\right), \quad i = 1, 2, \quad (5.1)$$

where r_i is the radius of the i^{th} generation at the last stage of the simulation.

The radius/mass ratio of the second generation with respect to the first blob increases with L . The reason for it is that the size of the first generation bulge compared to the thickness of the parent string decreases as L increases, as shown

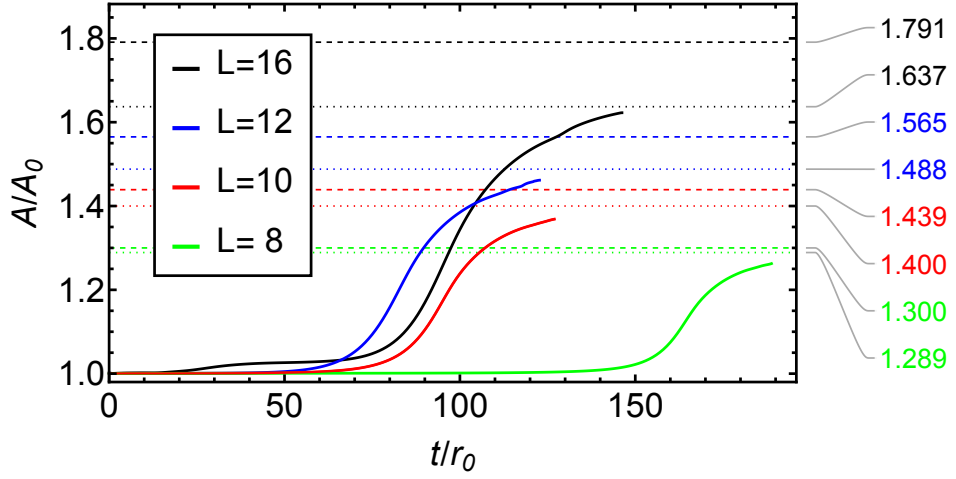


Fig. 5.2 Evolution of the AH area for the unstable black string in 5D with 4D mass parameter $r_0 = 1$ and different L 's. The dashed lines indicate the area for a slightly deformed 5D KK black hole with the same mass as the unperturbed black string [4]; The dotted lines are the areas of two black holes on a circle [5] with the same total mass as the unperturbed black string and the same radii as the first and second generation blobs measured at the end of the simulation.

in Fig. 5.3. As a result, the first generation of the string segment is thicker, which leads to larger second generation bulges compared to the first generation blob. This is expected that the second GL harmonic increases with L , keeping the radius of the string r_0 fixed. For L that is sufficiently large, GL harmonic would dominate the dynamics and one would expect the formation of two blobs with equal sizes. This phenomenon is observed in the third generation in the $L = 8$ run. Additionally, we notice that the size of the third generation compared to the second one also increases with L (see Fig. 5.1). Therefore, the estimated total area by only two KK BHs would be less accurate for smaller L .

It is likely that when the first generation forms there is a strong burst of gravitational waves emitted. In other cases of the GL instability, such a burst of emission is observed and its waveforms have been computed [35, 130]. After the formation of the first generation, the emission of the gravitational waves decreases over time, as the dynamics happens on ever decreasing scales where less and less mass is evolved. Near the pinch off the emission should be almost negligible. Right after the pinch off, there would be another strong emission of gravitational waves, as at that time the dynamics is approximately a head-on collision of two BHs, i.e. the first and the second generation blobs. The fact that the final AH area approaches the total area of two KK BHs implies that the emission of the gravitational radiation during the evolution of the GL instability is small by the end of our simulations. From the

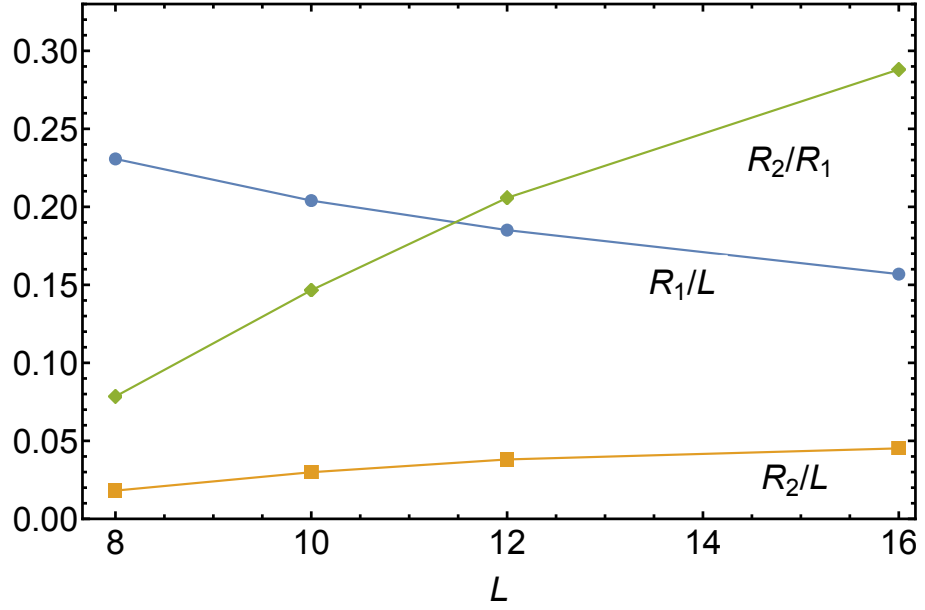


Fig. 5.3 Radius ratio of the first and second generations.

embedding diagrams in Fig. 5.1, we can see that the size of the second generation blob with respect to the first one increases with L . As a result, the mass ratio between the two BHs in the collision would decrease with L . In [131], they shown that in the 5D AF case the energy radiated in gravitational waves for the head-on collisions of black holes for different mass ratios is less than 0.1% of the initial total mass. Therefore, we expect that the total radiated energy via the gravitational wave emission during the GL instability of black strings, including the pinch off and final state should also be small. We hope to report on this in future work.

5.3 Horizon properties

As the computational cost for different L 's are different, we are not able to push the runs equally close to the singularities for all values of L due to the limitation of the computational resources. In particular, the $L = 10$ case corresponds to the fastest growth rate of the shortest wavelength instability and we have shown the results in the previous chapter. So we expect that in the other cases the dynamics would enter the non-linear regime later than the $L = 10$ case. From our data, the times that the first generation appears are $\Delta T_0/r_0 = 163.1, 93, 78, 91$ for $L = 8, 10, 12, 16$. As we expected, it takes a bit longer to enter the non-linear regime for the $L = 8$ case, which corresponds to a fatter string. In practice, we find that with our perturbations and the values of L we consider, the time that it takes for the first GL instability

to appear is more or less the same in all cases. The times for the second generation to appear after the first generation has formed are $\Delta T_1/r_0 = 10.6, 14.3, 15.3, 15.9$ for $L = 8, 10, 12, 16$, which increases with L .

From Table 5.1, we can obtain that the time for the first generation to form increases with L . Specifically, $(t_{p,1} - t_{n,1})/r_0 = 11.6, 14, 18.4, 21.7$ for $L = 8, 10, 12, 16$, respectively. The time for the second generation to form $(t_{p,2} - t_{n,2})/r_0 = 1.3, 2.5, 3.65, 5.1$ which also increases with L .

L	Gen.	$t_{p,i}/r_0$	$t_{n,i}/r_0$	n_s	$R_{s,i}/r_0$	$R_{h,f}/r_0$	$R_{s,i}/L_{s,i}$
8	1	163.1	174.7	1	1	1.846	0.125
	2	185.3	186.6	1	0.106	0.145	0.019
	3	188.1/188.1	188.63/188.62	2	0.0230	0.0657/0.0585	0.0078
10	1	93	107	1	1	2.04	0.1
	2	121.3	123.8	1	0.162	0.299	0.023
	3	124.0	125.6	1	0.0539	0.124	0.016
	4	126.8	?	$\geq 1/1$	0.0185/0.0165	?	0.0076/0.012
12	1	78	96.4	1	1	2.221	0.0833
	2	111.7	115.35	1	0.209	0.457	0.025
	3	chaotic	?	≥ 1	0.0452	?	0.010
16	1	91	112.7	1	1	2.51	0.0625
	2	128.6	133.7	1	0.351	0.723	0.034
	3	chaotic	?	≥ 1	0.0263	?	0.0039

Table 5.1 Properties of the various generations according to our definitions for the time of formation.

Moreover, the formation time for each generation to form and the way it evolves varies for different strings. As a result, in some runs we have seen the formation of more generations than the other runs. For example, we see that the forming of the sixth generation in the $L = 12$ run, while in the $L = 16$ run, we only see the third generation that are about to form. In Table 5.1, we summarise the time of formation for each generation in simulations with different L 's. In all the cases we have explored we do not find any evidence for a universal time scale relating the subsequent generations.

5.4 Satellite formation

Although the late-time dynamics of the horizons develop into a self-similar structure for all the cases we have considered, the formation details of the satellite BHs are different for different runs. We have already seen the AH evolution at different stages of the dynamics for the $L = 10$ case in Fig. 4.6. Apart from the relative

location of the first two generations and the time for each generation to appear, the dynamics up to the second generation are quantitatively the same for different L 's. That is, after the first generation has formed, the second generation forms in the middle of the first string segment. The size of the second generation with respect to the first one depends on the thickness of the initial string.

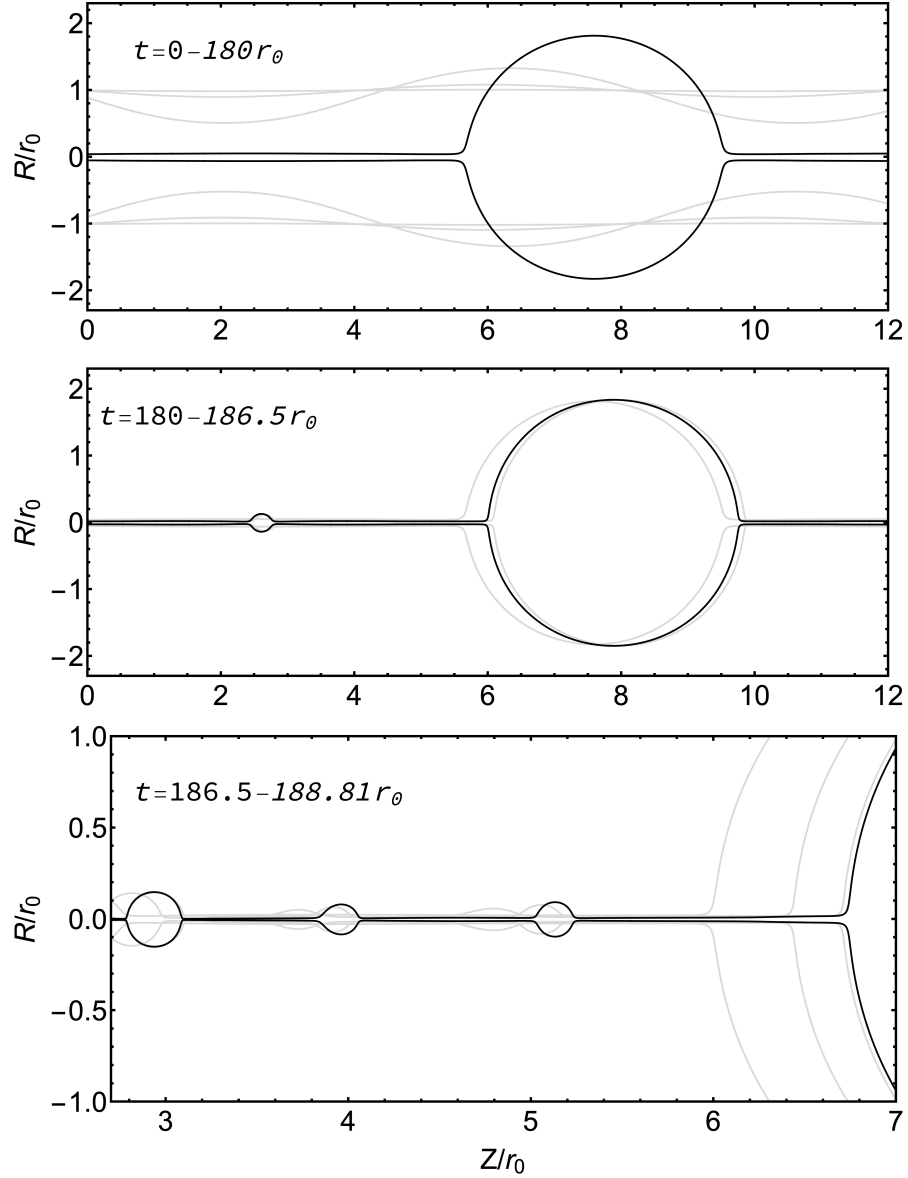


Fig. 5.4 Snapshots of the embedding diagrams of the AHs in our simulation at different stages. The length in the Z direction extends to 11.32 in the $L = 8$ case.

However, the further formation of the third generation and beyond are quite different for different runs. We observe that in some cases there are more than one blob forming at each string segment. We display the evolution process for the $L = 8$

run in Fig. 5.4. As we can see from the last panel in Fig. 5.4, there are two blobs forming at the same time at each string segment as the third generation. Moreover, in the $L = 10$ case two generations are forming at different string segments but at almost the same time, i.e. the fourth generation and the fifth one. In addition, in the case of $L = 12$, the third and fourth generations are eaten by the second one before it has time to fully form.

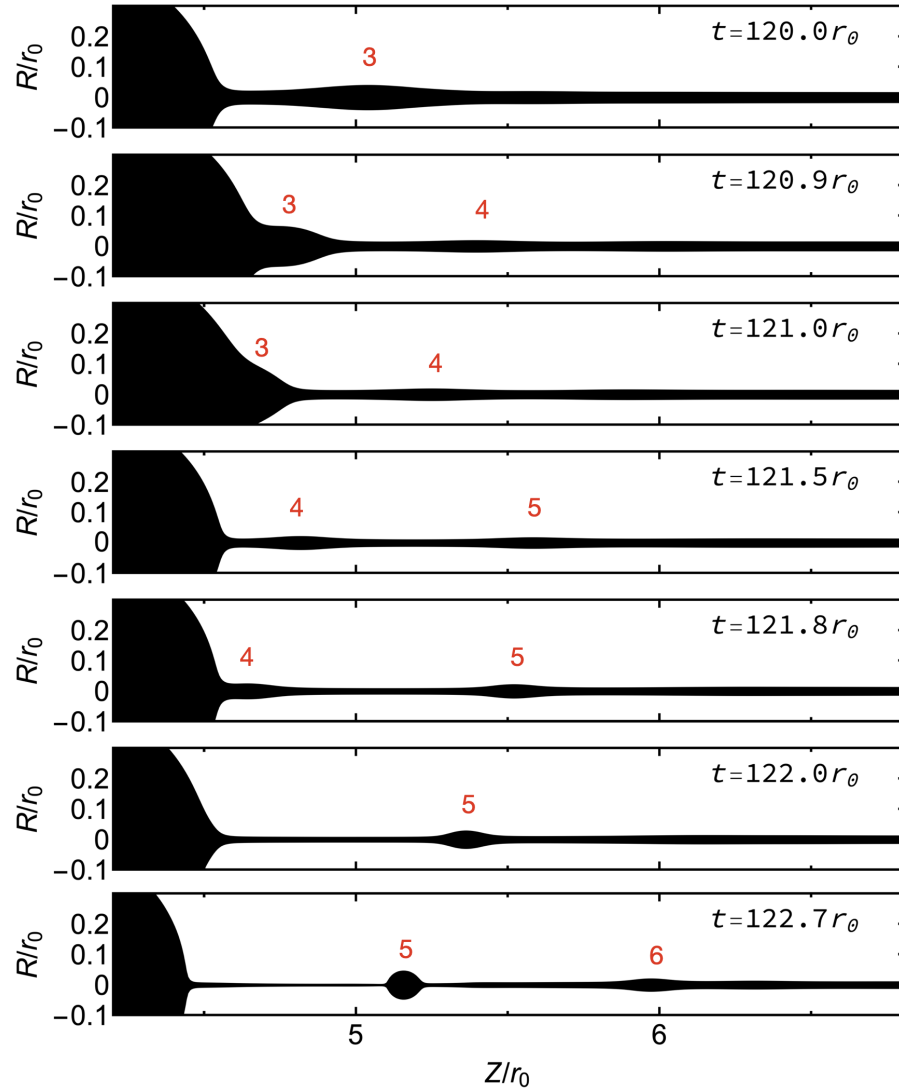


Fig. 5.5 Local dynamics of the bulges for the $L = 12$ case. The third and fourth generation bulges do not have enough time to fully form before being absorbed by the existing second generation bulge on the left. On the other hand, the fifth generation bulge fully forms and by the end of our simulation it is moving towards the second generation bulge. From the last panel we can see the sixth generation is about to form.

In the following we give more details about the local dynamics of the bulges for the $L = 12$ case. The local dynamics of the bulges is displayed in Fig. 5.5 about the string segment between the first and the second generations. After the second generation has formed, the third generation bulge starts to gather mass and its moving towards the second blob (see first panel in the figure). However, as it moves towards and is absorbed by the second blob before it fully forms (see second and third panels). Then a would-be fourth generation bulge starts to form near the third generation. It is also moving towards the second blob. The same situation happens here that it is also absorbed by the second generation bulge before it full forms. Then forming the fifth generation (fourth, fifth and sixth panels). This time it has enough time to fully form and it is still moving towards the second generation. Meanwhile, the sixth generation is about to form.

5.5 Approach to the singularity

In [3] the results indicate that the black string would pinch off in finite asymptotic time. They stated that the minimum of the areal radius of the black string follows an approximate scaling law

$$R_{min} = \alpha(t - t_c), \quad (5.2)$$

where α is a dimensionless constant and t_c is defined as the time for pinch off. We extract the values of α and t_c by fitting our simulation data to the scaling law (5.2). In Fig. 5.6 we display the logarithm plots for the minimum areal radius of the string as a function of the logarithm of the time to the singularity. Although we did not manage to get as close as the $L = 10, 12$ case to the singularity for the $L = 8, 16$ runs due to short of computational resources, we still extract the values in the scaling law based on the data we have. We collect the results of the fits for the various L 's in Table 5.2.

Although the development of the future generations for different runs towards the singularity are different, the results in Table 5.2 suggest that the slope of the scaling law (5.2) seems independent of L at least within errors. Hence, this suggests that there exists a universal scaling law that governs the pinch off of the black string horizon. Interestingly, the values of the slope for black string are essentially half of that found in the case of the ultraspinning instability of Myers-Perry black holes in six spacetime dimensions in [35], where the local geometry of the AH is that of

a black membrane. It would be interesting to explore the underlying factor that determines the difference between the slopes of the scaling laws.

L/r_0	a	t_c/r_0
8	0.0058	189.6
10	0.0052	127.9
12	0.0048	123.5
16	0.0045	148.2

Table 5.2 Slope of the scaling law (5.2) and the estimated pinch off time for the different L 's.

5.5.1 The pinch off

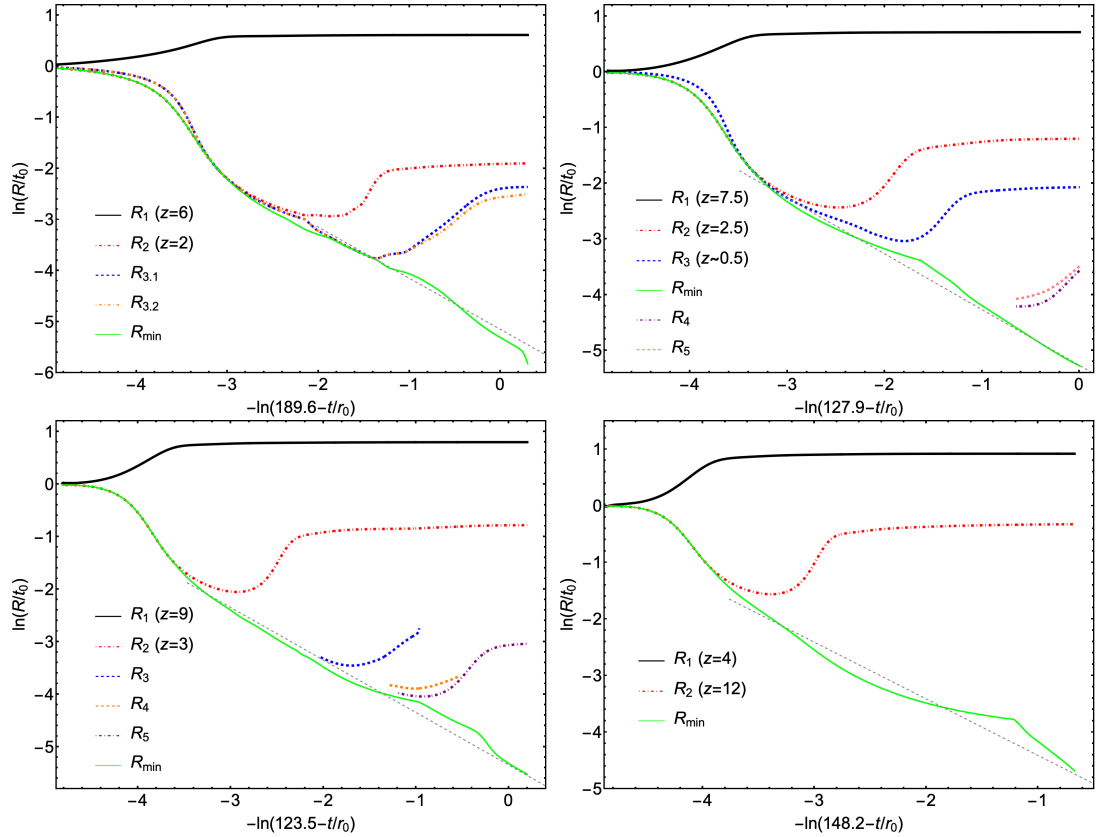


Fig. 5.6 The areal radius R of the AH as a function of the time to the singularity in the logarithmic coordinates, for the $L = 8, 10, 12, 16$ cases, from left to right and top to bottom, respectively. We display the evolution of the minimum string radius R_{min} as well as the equatorial radii of several generations. The grey dashed line is a visual add of the linear fit to the late-time minimal radius.

In Fig. 5.6 we display the logarithm of the minimum areal radius of the string as a function of the logarithm of the time to the singularity. Moreover, we also display the equatorial radii of several generations. The grey dashed line is a visual add of the linear fit to the late-time minimal radius. We can conclude that for all the cases we have considered, the minimal radius of the string follows a universal scaling law that is independent of the value of L . Therefore the horizon is expected to pinch off in finite asymptotic time in general.

5.5.2 Evolution of the proper length

In Fig. 5.7 we display the logarithm of the proper length of the string as a function of the logarithm of the time to the singularity. The slope for the $L = 8, 10, 12, 16$ cases is 0.053, 0.053, 0.049, 0.049, respectively. This is consistent with the value in [3].

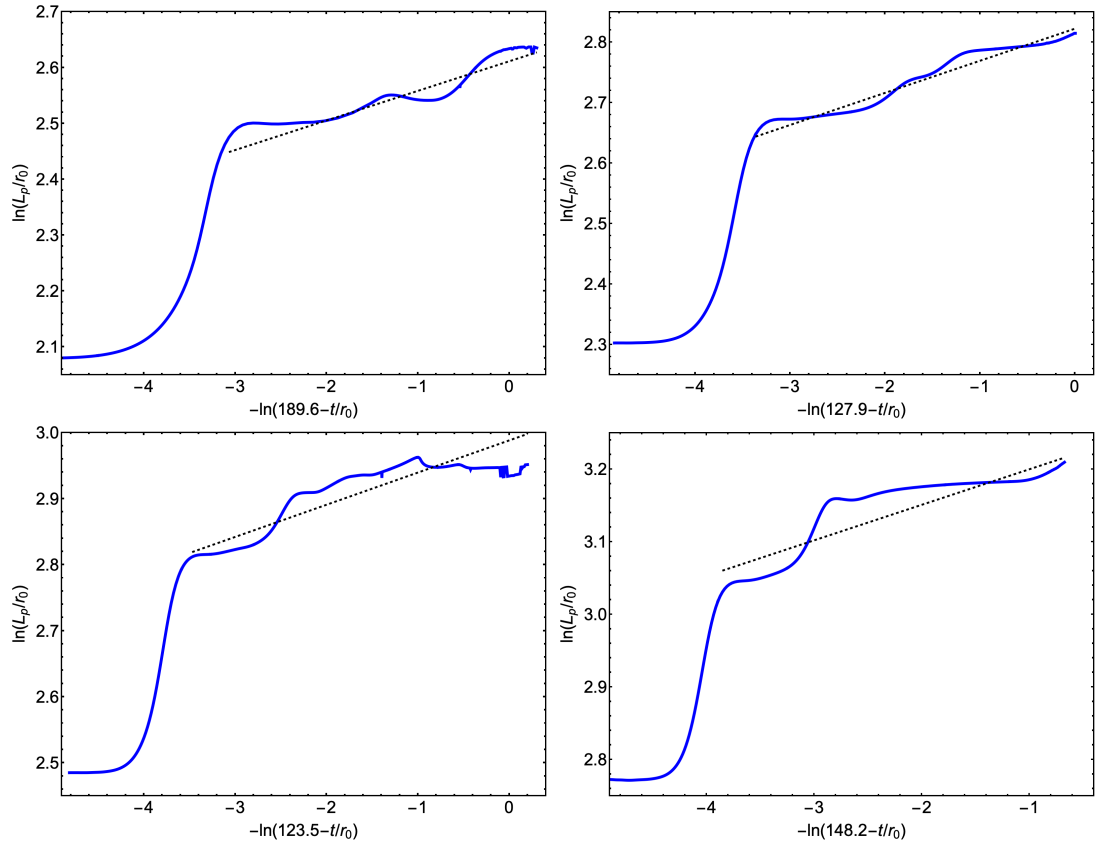


Fig. 5.7 The proper length of the string as a function of the logarithm of the time to the singularity in the logarithmic coordinates, for the $L = 8, 10, 12, 16$ cases, from left to right and top to bottom, respectively. The dashed line is linear fit to the late-time development of the proper length. The slope is 0.053, 0.053, 0.049, 0.049 for the $L = 8, 10, 12, 16$ cases, respectively.

5.5.3 Velocity profile

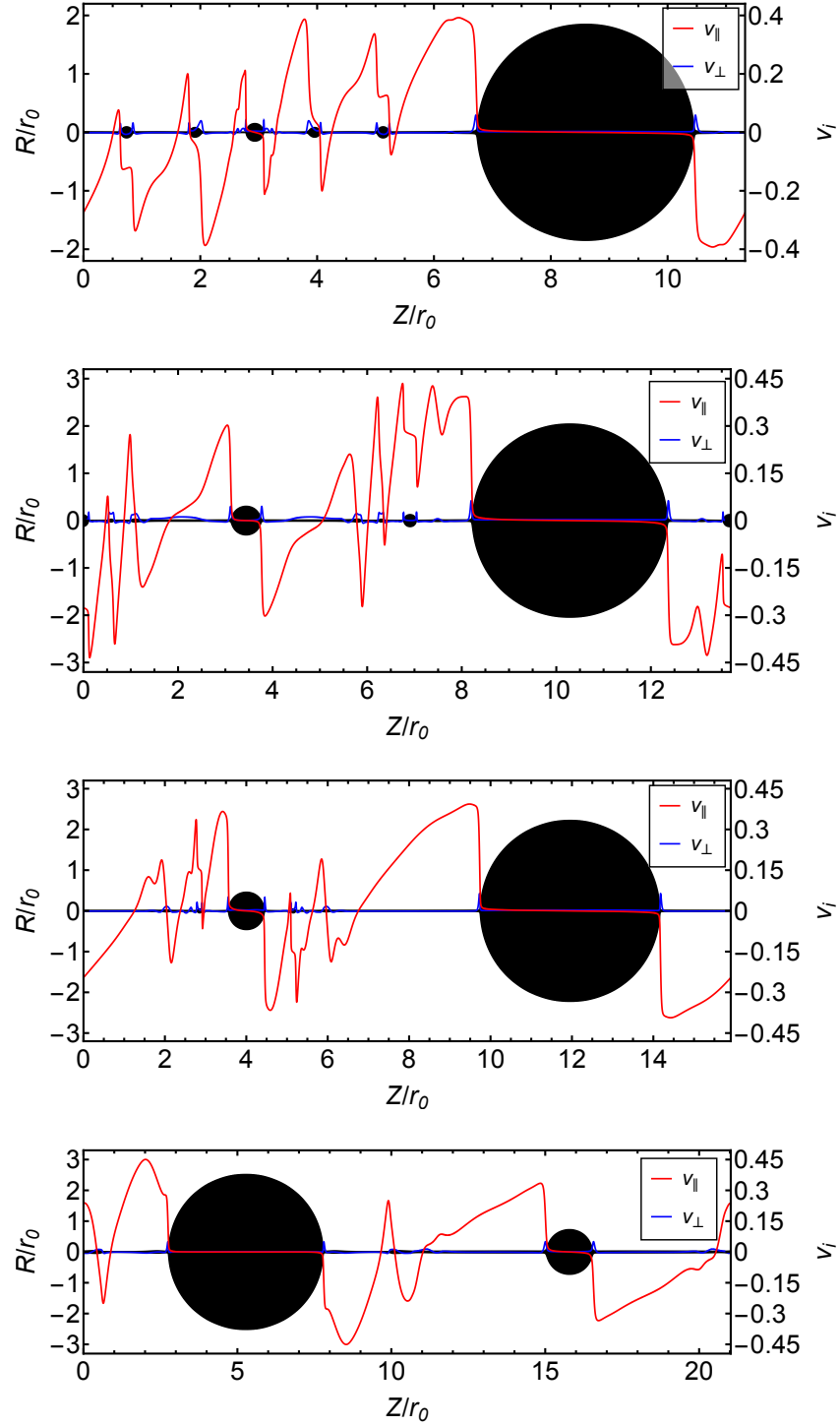


Fig. 5.8 Velocity profile at the last stage of the simulations for $L = 8, 10, 12, 16$, from top to bottom, respectively. The tangential and orthogonal velocities are shown in red and blue curves respectively.

In order to track the motion of the bulges qualitatively we plot the tangential and orthogonal velocities in Fig. 5.8. In all the cases, the motion of the blobs is slow compared to the development of the local GL instabilities on smaller scales. The smaller blobs are accreting matter from the surrounding segments of string, as shown by the non-zero orthogonal velocities, while they are collectively being dragged towards the second or first generation blobs.

5.5.4 Mode behaviour

In this section, we display the evolution of the expansion coefficients at different stages for different runs. In Fig. 5.9, we display the mode behaviour of the first string segment for different L 's, from $t_{n,1}$ to $t_{p,2}$.

In Fig. 5.10, we display the mode behaviour of the second string segment for different L 's, from $t_{n,2}$ to $t_{p,3}$.

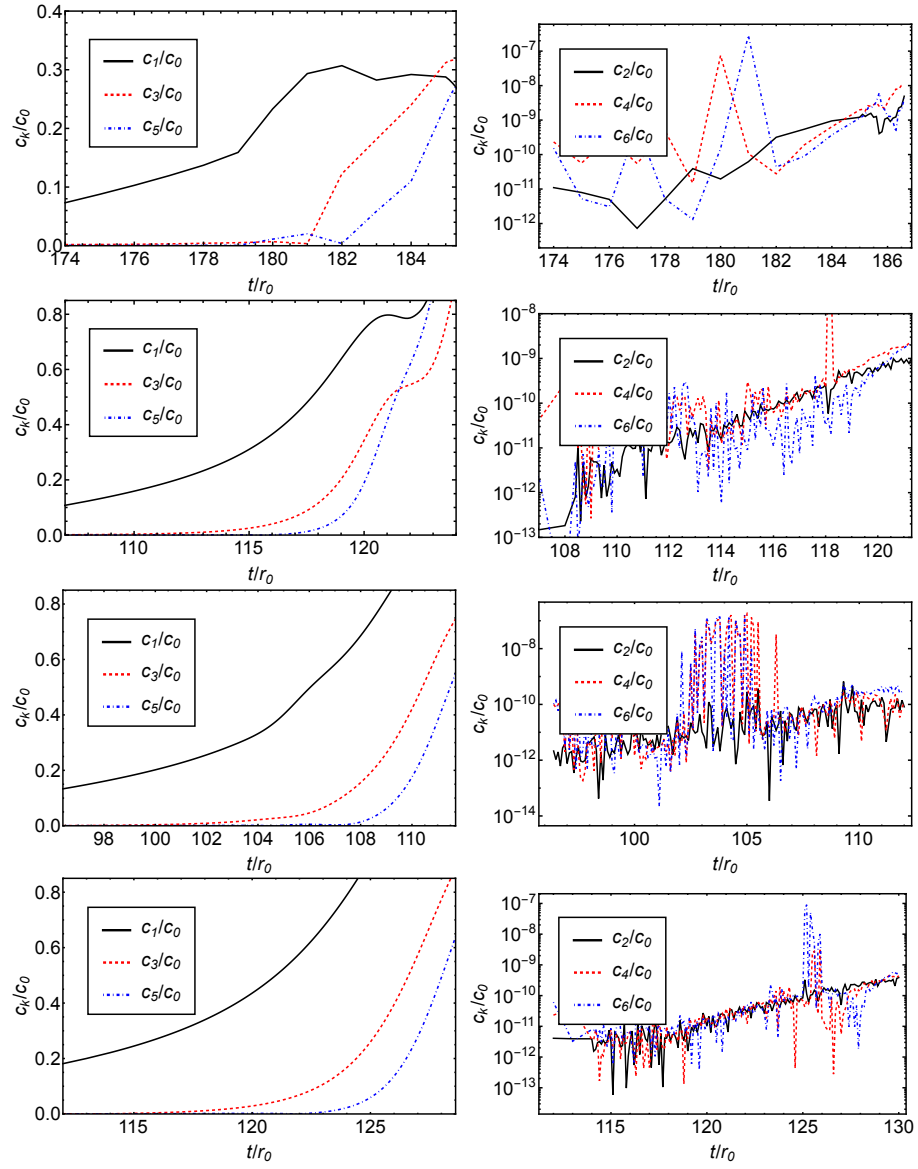


Fig. 5.9 Mode behaviour of the first string segment for different L 's, from $t_{n,1}$ to $t_{p,2}$

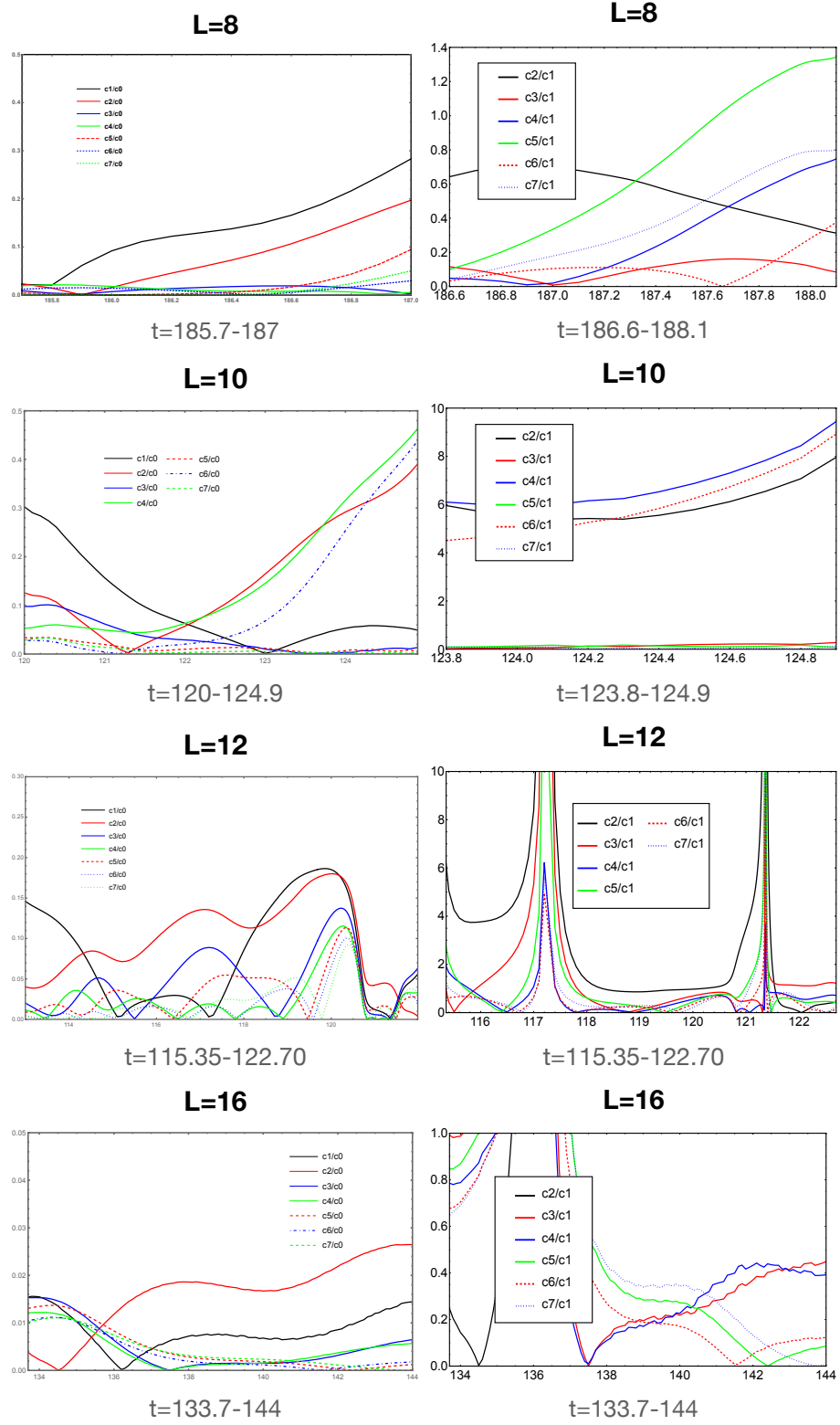


Fig. 5.10 Mode behaviour of the second string segment for different L 's, from $t_{n,2}$ to $t_{p,3}$

5.6 Discussion

In this chapter, we summarised the simulations results from the black strings of the various lengths we have explored. We find that the general picture of the development of the GL instability are the same for all cases. That is, the horizon develops into a fractal structure of satellite BHs and black strings on different scales. Although the details of the late-time dynamics of the generations are different for different L 's, the way the horizon approaches to the singularity is the same. In particular, we discover the the minimal radius of the string is governed by a scaling law that is independent of the value of L . Furthermore, the late-time development of the proper length also grows in a similar way. Therefore, it is a universal feature that the horizon will eventually pinch off in finite asymptotic time, thus it provides further evidence against the WCCC.

Our study extended the results of [3] in the following aspects. First, we have independently reproduced the simulation of black string that has the same initial setting as [3] and confirmed their main results. Second, we improved their simulation results and extended the evolution much closer to the pinch off to reveal more detailed and accurate late-time dynamics. Third, we have explored strings with different lengths to provide a more general picture of the GL instability on black strings. However, due to the limitation in the computational resources, we could not get each run equally close to the singularity. For future work, we aim to push the $L = 10$ run further as $L = 10$ corresponds to the fastest growth rate of the instability. It would be interesting to learn more about the nature of the singularity at the pinch off.

Chapter 6

Conclusion and Outlook

In this thesis, we have studied the gravitational instabilities in black string space-times and the violation to the Weak Cosmic Censorship conjecture by numerical simulations. We presented the numerical construction and analysis methods for working in higher dimensions. In particular, we have derived the CCZ4 formulation in arbitrary dimensions and implemented the equations in our own **GRChombo** code with the symmetry reduction terms by the modified Cartoon method. Appropriate initial conditions for the evolution has been derived which guarantees that the simulation does not crash in the very beginning. We used the Modified Gamma-driver shift conditions to help achieve stable simulations in higher-dimensional settings. Additionally, we have added singularity diffusion terms to damp the large gradient near the singularity. Equipped with these techniques and methods for higher dimensions, we managed to reproduce the previous study on the GL instability of the five-dimensional black strings. We have illustrated the numerical methods we used for achieving stable simulations and presented our simulation results and compared with the previous study. Furthermore, we have explored strings with different lengths to provide a more general picture of the development of the GL instability on black strings.

We have revisited the famous previous study on the GL instability on the five-dimensional black strings by Lehner and Pretorius [3]. We reproduced their results with a different and independent method and improved the simulation results with higher resolution. In particular, we extended the study to provide further evidence of the late-time dynamics of the GL instability. Our results agree with [3] very well up to the second generation. We have confirmed that the late-time dynamics of the unstable black string can be described by a sequence of black holes of various

sizes connected by string segments. Each of the string segment itself is consistently shrinking and is unstable to the GL instability on different scales, resulting in a pinch off in finite asymptotic time. Therefore, this process leads to a naked singularity that violates the WCCC.

Furthermore, we have explored strings with different lengths and masses. Our simulations have allowed us to get closer to the singularities than ever before so that we have provided a more general picture of the late-time development of the GL instability of the black strings. We have confirmed that the pinch off of the horizon in finite time is the fate for all the cases, but we do not find a universal time scale as stated in previous study in all cases we have considered. The reason for that in the late time of the development of the GL instability, the higher generation bulges are not only controlled by the local GL instability but also affected by the movement and tensions of the nearby bulges and strings. Besides, the string segments connecting the higher generations are not uniform any more beyond the third generation. So the bulges are not always appearing in the middle of the string segment and they are usually moving towards the previous generation, which depends on their relative locations and sizes. However, the minimum thickness of the string follows a scaling law (5.2) which leads to the pinch off of the horizon.

In our study, we carried out four runs in total for black strings with different lengths. Although $L = 10$ corresponds to the fastest growth rate of the GL instability, we did not observe the kick-in time of the GL instability in other runs significantly later. For future work, one can explore strings with a boarder range of the lengths to verify the theory about the growth rate of the GL instability. The set of the parameters in our study can be applied directly, as they were tested to work well regardless the length of the string. In addition, different initial perturbations can be tested to check whether the initial mode affects the development of the GL instability. We expect that the symmetry in the dynamics will still agree with the symmetry of the initial perturbation. Moreover, the evolution equations and the reduction terms in this work are derived in arbitrary dimension. They can be use to study problems in different dimensions in the future. It would be interesting to see whether the GL instability develops in the same way for problems in higher dimensions.

In our study, we have pushed the evolution of the GL instability of the black string closer than ever to the pinch off. One of the most interesting open questions about the evolution of the GL instability of the black string is to understand the nature

of the singularity at the pinch off. As the black string is probably the simplest and cleanest system of GR, it has profound implications for the physical consequences of certain violations of the WCCC, which has significant effects to the predictivity of the theory of GR. It is conjectured in [132] that the pinch off of the GL instability of black strings would have a similar picture to that in the case of non-relativistic incompressible fluids. In [123], they found that there is a universal scale invariant attractor solution of the Navier-Stokes equations that governs the pinch off of an axisymmetric column of fluid. Moreover, [123] also shows that the region that is involved in the pinch off is basically only a microscopic part of the fluid, and this region is insensitive to the evolution of the fluid on macroscopic scales. These indicate that the loss of predictivity of the classical hydrodynamic equations at the pinch off is minimal and the development of the pinch off is not affected by the macroscopic evolution of the fluid. Therefore, it would be interesting to see whether black strings have the same nature close to the pinch off. Another interesting question is before the pinch off whether there are an infinite amount of generations or there are only a finite number of generations. In the former case, the horizon will develop into a fractal structure, while in the latter case this structure would break down at some point. In the future, we will continue the run to get closer to the singularity and explore what governs the pinch off and understand its nature.

Another interesting direction is to explore the GL instability with higher derivative corrections to the Einstein-Hilbert Lagrangian. The higher derivative corrections are expected to become important when the evolution of the black string approaches the pinch off [82]. Recent studies have shown that certain higher derivative theories of gravity in higher dimensions are well-posed in reasonably straightforward modifications of the gauges that are commonly used in numerical relativity [133–135]. Therefore, it would be interesting to check whether this is also the case in the regime that can be probed by numerical simulations and quantify the effects of such corrections on the dynamics during the evolution of the GL instability.

References

- [1] Thomas King, Simon Butcher, and Lukasz Zalewski. *Apocrita - High Performance Computing Cluster for Queen Mary University of London*.
- [2] Miguel Alcubierre. *Introduction to 3+1 numerical relativity*, volume 140. OUP Oxford, 2008.
- [3] Luis Lehner and Frans Pretorius. Final state of gregory-laflamme instability. *arXiv preprint arXiv:1106.5184*, 2011.
- [4] Troels Harmark. Small black holes on cylinders. *Physical Review D*, 69(10):104015, 2004.
- [5] Oscar JC Dias, Troels Harmark, Robert C Myers, and Niels A Obers. Multi-black-hole configurations on the cylinder. *Physical Review D*, 76(10):104025, 2007.
- [6] Clifford M Will. The confrontation between general relativity and experiment. *Living reviews in relativity*, 17:1–117, 2014.
- [7] Karl Schwarzschild. Über das gravitationsfeld eines massenpunktes nach der einstein’schen theorie. *Berlin. Sitzungsberichte*, 18, 1916.
- [8] Hans Reissner. Über die eigengravitation des elektrischen felde nach der einsteinschen theorie. *Annalen der Physik*, 355(9):106–120, 1916.
- [9] Gunnar Nordström. On the energy of the gravitation field in einstein’s theory. *Koninklijke Nederlandse Akademie van Wetenschappen Proceedings Series B Physical Sciences*, 20:1238–1245, 1918.
- [10] Roy P Kerr. Gravitational field of a spinning mass as an example of algebraically special metrics. *Physical review letters*, 11(5):237, 1963.
- [11] Benjamin P Abbott, Richard Abbott, TD Abbott, MR Abernathy, Fausto Acernese, Kendall Ackley, Carl Adams, Thomas Adams, Paolo Addesso, RX Adhikari, et al. Observation of gravitational waves from a binary black hole merger. *Physical review letters*, 116(6):061102, 2016.
- [12] Benjamin P Abbott, Richard Abbott, TD Abbott, MR Abernathy, F Acernese, K Ackley, C Adams, T Adams, P Addesso, RX Adhikari, et al. Properties of the binary black hole merger GW150914. *Physical review letters*, 116(24):241102, 2016.

- [13] Junaid Aasi, BP Abbott, Richard Abbott, Thomas Abbott, MR Abernathy, Kendall Ackley, Carl Adams, Thomas Adams, Paolo Addesso, RX Adhikari, et al. Advanced LIGO. *Classical and quantum gravity*, 32(7):074001, 2015.
- [14] Benjamin P Abbott, R Abbott, TD Abbott, Fausto Acernese, K Ackley, C Adams, T Adams, P Addesso, RX Adhikari, VB Adya, et al. GW170608: observation of a 19 solar-mass binary black hole coalescence. *The Astrophysical Journal Letters*, 851(2):L35, 2017.
- [15] LIGO Scientific, Benjamin P Abbott, R Abbott, TD Abbott, F Acernese, K Ackley, C Adams, T Adams, P Addesso, RX Adhikari, et al. GW170104: observation of a 50-solar-mass binary black hole coalescence at redshift 0.2. *Physical review letters*, 118(22):221101, 2017.
- [16] Benjamin P Abbott, Richard Abbott, TD Abbott, F Acernese, K Ackley, C Adams, T Adams, P Addesso, Rana X Adhikari, Vaishali B Adya, et al. GW170814: a three-detector observation of gravitational waves from a binary black hole coalescence. *Physical review letters*, 119(14):141101, 2017.
- [17] Benjamin P Abbott, Rich Abbott, TDea Abbott, Fausto Acernese, Kendall Ackley, Carl Adams, Thomas Adams, Paolo Addesso, RX Adhikari, Vaishali B Adya, et al. GW170817: observation of gravitational waves from a binary neutron star inspiral. *Physical review letters*, 119(16):161101, 2017.
- [18] Benjamin P Abbott, R Abbott, TD Abbott, S Abraham, F Acernese, K Ackley, C Adams, VB Adya, C Affeldt, M Agathos, et al. Prospects for observing and localizing gravitational-wave transients with advanced LIGO, advanced Virgo and KAGRA. *Living reviews in relativity*, 23:1–69, 2020.
- [19] R Abbott, TD Abbott, S Abraham, F Acernese, K Ackley, A Adams, C Adams, RX Adhikari, VB Adya, Christoph Affeldt, et al. GWTC-2: compact binary coalescences observed by ligo and virgo during the first half of the third observing run. *Physical Review X*, 11(2):021053, 2021.
- [20] Fet al Acernese, M Agathos, K Agatsuma, D Aisa, N Allemandou, A Allocca, J Amarni, P Astone, G Balestri, G Ballardini, et al. Advanced Virgo: a second-generation interferometric gravitational wave detector. *Classical and Quantum Gravity*, 32(2):024001, 2014.
- [21] Benjamin P Abbott, R Abbott, TD Abbott, MR Abernathy, F Acernese, K Ackley, C Adams, T Adams, P Addesso, RX Adhikari, et al. GW151226: observation of gravitational waves from a 22-solar-mass binary black hole coalescence. *Physical review letters*, 116(24):241103, 2016.
- [22] Rebecca Azulay, Anne-Kathrin Baczko, David Ball, Mislav Baloković, John Barrett, Dan Bintley, Lindy Blackburn, Wilfred Boland, Katherine L Bouman, Geoffrey C Bower, et al. First M87 event horizon telescope results. i. the shadow of the supermassive black hole. *The Astrophysical Journal Letters*, 875(L1):17pp, 2019.
- [23] Kazunori Akiyama, Antxon Alberdi, Walter Alef, Juan Carlos Algaba, Richard Anantua, Keiichi Asada, Rebecca Azulay, Uwe Bach, Anne-Kathrin Baczko, David Ball, et al. First sagittarius A* event horizon telescope results. iv.

- variability, morphology, and black hole mass. *The Astrophysical Journal Letters*, 930(2):L15, 2022.
- [24] Roger Penrose. Gravitational collapse and space-time singularities. *Physical Review Letters*, 14(3):57, 1965.
- [25] Stephen William Hawking and Roger Penrose. The singularities of gravitational collapse and cosmology. *Proceedings of the Royal Society of London. A. Mathematical and Physical Sciences*, 314(1519):529–548, 1970.
- [26] Roger Penrose. Gravitational collapse: The role of general relativity. *Nuovo Cimento Rivista Serie*, 1:252, 1969.
- [27] Robert Geroch and Gary T Horowitz. Asymptotically simple does not imply asymptotically minkowskian. *Physical Review Letters*, 40(4):203, 1978.
- [28] Robert Geroch and Gary T Horowitz. Global structure of spacetimes, in *General Relativity: An Einstein Centenary Survey*. 1979.
- [29] Demetrios Christodoulou. The instability of naked singularities in the gravitational collapse of a scalar field. *Annals of Mathematics*, 149(1):183–217, 1999.
- [30] Matthew W Choptuik. Universality and scaling in gravitational collapse of a massless scalar field. *Physical Review Letters*, 70(1):9, 1993.
- [31] Theodor Kaluza. Zum unitätsproblem der physik. *Sitzungsberichte der Königlich Preussischen Akademie der Wissenschaften (Berlin)*, pages 966–972, 1921.
- [32] Oskar Klein. *Quantentheorie und fünfdimensionale Relativitätstheorie*, volume 37. Springer, 1926.
- [33] Ruth Gregory. *The Gregory-Laflamme instability*, volume 70, 2837. Cambridge University Press, 1993.
- [34] Pau Figueras, Markus Kunesch, and Saran Tunyasuvunakool. End point of black ring instabilities and the weak cosmic censorship conjecture. *Physical review letters*, 116(7):071102, 2016.
- [35] Pau Figueras, Markus Kunesch, Luis Lehner, and Saran Tunyasuvunakool. End point of the ultraspinning instability and violation of cosmic censorship. *Physical Review Letters*, 118(15):151103, 2017.
- [36] Hans Bantilan, Pau Figueras, Markus Kunesch, and Rodrigo Panosso Macedo. End point of nonaxisymmetric black hole instabilities in higher dimensions. *Physical Review D*, 100(8):086014, 2019.
- [37] Tomas Andrade, Pau Figueras, and Ulrich Sperhake. Evidence for violations of weak cosmic censorship in black hole collisions in higher dimensions. *Journal of High Energy Physics*, 2022(3):1–29, 2022.
- [38] Roberto Emparan and Robert C Myers. Instability of ultra-spinning black holes. *Journal of High Energy Physics*, 2003(09):025, 2003.

- [39] Oscar JC Dias, Pau Figueras, Ricardo Monteiro, Jorge E Santos, and Roberto Emparan. Instability and new phases of higher-dimensional rotating black holes. *Physical Review D*, 80(11):111701, 2009.
- [40] Oscar JC Dias, Pau Figueras, Ricardo Monteiro, Harvey S Reall, and Jorge E Santos. An instability of higher-dimensional rotating black holes. *Journal of High Energy Physics*, 2010(5):1–47, 2010.
- [41] Óscar JC Dias, Gavin S Hartnett, and Jorge E Santos. Quasinormal modes of asymptotically flat rotating black holes. *Classical and Quantum Gravity*, 31(24):245011, 2014.
- [42] Jorge E Santos and Benson Way. Neutral black rings in five dimensions are unstable. *Physical Review Letters*, 114(22):221101, 2015.
- [43] Veronika E Hubeny and Mukund Rangamani. Unstable horizons. *Journal of High Energy Physics*, 2002(05):027, 2002.
- [44] HJ De Vega and LN Lipatov. Interaction of reggeized gluons in the baxter-sklyanin representation. *Physical Review D*, 64(11):114019, 2001.
- [45] Masaru Shibata and Hirotaka Yoshino. Bar-mode instability of a rapidly spinning black hole in higher dimensions: Numerical simulation in general relativity. *Physical Review D*, 81(10):104035, 2010.
- [46] William G Cook, Pau Figueras, Markus Kunesch, Ulrich Sperhake, and Saran Tunyasuvunakool. Dimensional reduction in numerical relativity: Modified cartoon formalism and regularization. *International Journal of Modern Physics D*, 25(09):1641013, 2016.
- [47] Katy Clough, Pau Figueras, Hal Finkel, Markus Kunesch, Eugene A Lim, and Saran Tunyasuvunakool. GRChombo: numerical relativity with adaptive mesh refinement. *Classical and Quantum Gravity*, 32(24):245011, 2015.
- [48] Tomas Andrade, Llibert Areste Salo, Josu C Aurrekoetxea, Jamie Bamber, Katy Clough, Robin Croft, Eloy de Jong, Amelia Drew, Alejandro Duran, Pedro G Ferreira, et al. GRChombo: An adaptable numerical relativity code for fundamental physics. *J. Open Source Softw.*, 6(3703), 2022.
- [49] M Adams, PO Schwartz, H Johansen, P Colella, TJ Ligoeki, D Martin, N Keen, D Graves, D Modiano, and B Van Straalen. Chombo software package for amr applications-design document (tech. rep.). *Berkeley, CA: Applied Numerical Algorithms Group Computational Research Division Lawrence Berkeley National Laboratory*, 2015.
- [50] Katy Clough and Eugene A Lim. Critical phenomena in non-spherically symmetric scalar bubble collapse. *arXiv preprint arXiv:1602.02568*, 2016.
- [51] Thomas Helfer, David JE Marsh, Katy Clough, Malcolm Fairbairn, Eugene A Lim, and Ricardo Becerril. Black hole formation from axion stars. *Journal of Cosmology and Astroparticle Physics*, 2017(03):055, 2017.

- [52] Katy Clough, Eugene A Lim, Brandon S DiNunno, Willy Fischler, Raphael Flauger, and Sonia Paban. Robustness of inflation to inhomogeneous initial conditions. *Journal of Cosmology and Astroparticle Physics*, 2017(09):025.
- [53] Katy Clough, Tim Dietrich, and Jens C Niemeyer. Axion star collisions with black holes and neutron stars in full 3d numerical relativity. *Physical Review D*, 98(8):083020, 2018.
- [54] James Y Widdicombe, Thomas Helfer, David JE Marsh, and Eugene A Lim. Formation of relativistic axion stars. *Journal of Cosmology and Astroparticle Physics*, 2018(10):005.
- [55] Katy Clough, Raphael Flauger, and Eugene A Lim. Robustness of inflation to large tensor perturbations. *Journal of Cosmology and Astroparticle Physics*, 2018(05):065.
- [56] Thomas Helfer, Josu C Aurrekoetxea, and Eugene A Lim. Cosmic string loop collapse in full general relativity. *Physical Review D*, 99(10):104028, 2019.
- [57] Tomas Andrade, Roberto Emparan, David Licht, and Raimon Luna. Cosmic censorship violation in black hole collisions in higher dimensions. *Journal of High Energy Physics*, 2019(4):1–9, 2019.
- [58] Katy Clough, Pedro G Ferreira, and Macarena Lagos. Growth of massive scalar hair around a schwarzschild black hole. *Physical Review D*, 100(6):063014, 2019.
- [59] Francesco Muia, Michele Cicoli, Katy Clough, Francisco Pedro, Fernando Quevedo, and Gian Paolo Vacca. The fate of dense scalar stars. *Journal of Cosmology and Astroparticle Physics*, 2019(07):044.
- [60] James Y Widdicombe, Thomas Helfer, and Eugene A Lim. Black hole formation in relativistic oscillaton collisions. *Journal of Cosmology and Astroparticle Physics*, 2020(01):027.
- [61] Pau Figueras and Tiago França. Gravitational collapse in cubic horndeski theories. *Classical and Quantum Gravity*, 37(22):225009, 2020.
- [62] Jamie Bamber, Katy Clough, Pedro G Ferreira, Lam Hui, and Macarena Lagos. Growth of accretion driven scalar hair around kerr black holes. *Physical Review D*, 103(4):044059, 2021.
- [63] Miren Radia, Ulrich Sperhake, Emanuele Berti, and Robin Croft. Anomalies in the gravitational recoil of eccentric black-hole mergers with unequal mass ratios. *Physical Review D*, 103(10):104006, 2021.
- [64] Dina Traykova, Katy Clough, Thomas Helfer, Emanuele Berti, Pedro G Ferreira, and Lam Hui. Dynamical friction from scalar dark matter in the relativistic regime. *Physical Review D*, 104(10):103014, 2021.
- [65] Cristian Joana and Sébastien Clesse. Inhomogeneous preinflation across hubble scales in full general relativity. *Physical Review D*, 103(8):083501, 2021.

- [66] Zainab Nazari, Michele Cicoli, Katy Clough, and Francesco Muia. Oscillon collapse to black holes. *Journal of Cosmology and Astroparticle Physics*, 2021(05):027, 2021.
- [67] Pau Figueras and Tiago França. Black hole binaries in cubic horndeski theories. *Physical Review D*, 105(12):124004, 2022.
- [68] Miren Radia, Ulrich Sperhake, Amelia Drew, Katy Clough, Pau Figueras, Eugene A Lim, Justin L Ripley, Josu C Aurrekoetxea, Tiago França, and Thomas Helfer. Lessons for adaptive mesh refinement in numerical relativity. *Classical and Quantum Gravity*, 39(13):135006, 2022.
- [69] Thomas Helfer, Ulrich Sperhake, Robin Croft, Miren Radia, Bo-Xuan Ge, and Eugene A Lim. Malaise and remedy of binary boson-star initial data. *Classical and Quantum Gravity*, 39(7):074001, 2022.
- [70] Eloy De Jong, Josu C Aurrekoetxea, and Eugene A Lim. Primordial black hole formation with full numerical relativity. *Journal of Cosmology and Astroparticle Physics*, 2022(03):029.
- [71] Tomas Andrade, Pau Figueras, and Ulrich Sperhake. Evidence for violations of weak cosmic censorship in black hole collisions in higher dimensions. *JHEP*, 03:111, 2022.
- [72] Amelia Drew and EPS Shellard. Radiation from global topological strings using adaptive mesh refinement: methodology and massless modes. *Physical Review D*, 105(6):063517, 2022.
- [73] Zipeng Wang, Thomas Helfer, Katy Clough, and Emanuele Berti. Superradiance in massive vector fields with spatially varying mass. *Physical Review D*, 105(10):104055, 2022.
- [74] Cristian Joana. Gravitational dynamics in higgs inflation: Preinflation and preheating with an auxiliary field. *Physical Review D*, 106(2):023504, 2022.
- [75] Katy Clough, Thomas Helfer, Helvi Witek, and Emanuele Berti. Ghost instabilities in self-interacting vector fields: The problem with proca fields. *Physical review letters*, 129(15):151102, 2022.
- [76] Josu C Aurrekoetxea, Pedro G Ferreira, Katy Clough, Eugene A Lim, and Oliver J Tattersall. Where is the ringdown: Reconstructing quasinormal modes from dispersive waves. *Physical Review D*, 106(10):104002, 2022.
- [77] Josu C Aurrekoetxea, Katy Clough, and Eugene A Lim. Cttk: A new method to solve the initial data constraints in numerical relativity. *arXiv preprint arXiv:2207.03125*, 2022.
- [78] Robin Croft, Thomas Helfer, Bo-Xuan Ge, Miren Radia, Tamara Evstafyeva, Eugene A Lim, Ulrich Sperhake, and Katy Clough. The gravitational afterglow of boson stars. *Classical and Quantum Gravity*, 2022.
- [79] Mark Ho-Yeuk Cheung, Vishal Baibhav, Emanuele Berti, Vitor Cardoso, Gregorio Carullo, Roberto Cotesta, Walter Del Pozzo, Francisco Duque, Thomas Helfer, Estuti Shukla, et al. Nonlinear effects in black hole ringdown. *Physical Review Letters*, 130(8):081401, 2023.

-
- [80] Llibert Aresté Saló, Katy Clough, and Pau Figueras. Well-posedness of the four-derivative scalar-tensor theory of gravity in singularity avoiding coordinates. *Physical Review Letters*, 129(26):261104, 2022.
 - [81] Jamie Bamber, Josu C Aurrekoetxea, Katy Clough, and Pedro G Ferreira. Black hole merger simulations in wave dark matter environments. *Physical Review D*, 107(2):024035, 2023.
 - [82] Pau Figueras, Tiago França, Chenxia Gu, and Tomas Andrade. Endpoint of the Gregory-Laflamme instability of black strings revisited. *Physical Review D*, 107(4):044028, 2023.
 - [83] Thomas W Baumgarte and Stuart L Shapiro. Numerical relativity: solving einstein’s equations on the computer. 2010.
 - [84] Helmut Friedrich. On the hyperbolicity of Einstein’s and other gauge field equations. *Communications in Mathematical Physics*, 100(4):525–543, 1985.
 - [85] James W. York. Sources of gravitational radiation. *Cambridge University Press*, page pp. 83–126, 1979. ISBN 0-521-22778-X.
 - [86] Takashi Nakamura, Kenichi Oohara, and Yasufumi Kojima. General relativistic collapse to black holes and gravitational waves from black holes. *Progress of Theoretical Physics Supplement*, 90:1–218, 1987.
 - [87] Masaru Shibata and Takashi Nakamura. Evolution of three-dimensional gravitational waves: Harmonic slicing case. *Physical Review D*, 52(10):5428, 1995.
 - [88] Thomas W Baumgarte and Stuart L Shapiro. Numerical integration of Einstein’s field equations. *Physical Review D*, 59(2):024007, 1998.
 - [89] Daniela Alic, Carles Bona-Casas, Carles Bona, Luciano Rezzolla, and Carlos Palenzuela. Conformal and covariant formulation of the Z4 system with constraint-violation damping. *Physical Review D*, 85(064040), 2012.
 - [90] Frans Pretorius. Numerical relativity using a generalized harmonic decomposition. *Classical and Quantum Gravity*, 22(2):425, 2005.
 - [91] Carles Bona, Joan Masso, Edward Seidel, and Joan Stela. New formalism for numerical relativity. *Physical Review Letters*, 75(4):600, 1995.
 - [92] Miguel Alcubierre, Bernd Brügmann, Peter Diener, Michael Koppitz, Denis Pollney, Edward Seidel, and Ryoji Takahashi. Gauge conditions for long-term numerical black hole evolutions without excision. *Physical Review D*, 67(8):084023, 2003.
 - [93] Doreen Müller, Jason Grigsby, and Bernd Brügmann. Dynamical shift condition for unequal mass black hole binaries. *Physical Review D*, 82(6):064004, 2010.
 - [94] Erik Schnetter. Time step size limitation introduced by the bssn gamma driver. *Classical and Quantum Gravity*, 27(16):167001, 2010.

- [95] Daniela Alic, Luciano Rezzolla, Ian Hinder, and Philipp Mösta. Dynamical damping terms for symmetry-seeking shift conditions. *Classical and quantum gravity*, 27(24):245023, 2010.
- [96] Daniela Alic, Wolfgang Kastaun, and Luciano Rezzolla. Constraint damping of the conformal and covariant formulation of the z4 system in simulations of binary neutron stars. *Physical Review D*, 88(6):064049, 2013.
- [97] F. Pretorius. Numerical relativity using a generalized harmonic decomposition. *Class. Quant. Grav.*, 22(425), 2005.
- [98] Einstein Albert, W Perrett, and G Jeffery. The foundation of the general theory of relativity. *Annalen der Physik*, 354(7):769, 1916.
- [99] Robert M. Wald. General relativity. *The univerisity of Chicago Press*, 1984.
- [100] Carles Bona, Tomáš Ledvinka, Carlos Palenzuela, and M Žáček. General-covariant evolution formalism for numerical relativity. *Physical Review D*, 67(10):104005, 2003.
- [101] G. Calabrese C. Gundlach, J. M. Martin-Garcia and I. Hinder. Constraint damping in the z4 formulation and harmonic gauge. *Class. Quant. Grav.*, 22(3767), 2005.
- [102] Béla Szilágyi. Key elements of robustness in binary black hole evolutions using spectral methods. *International Journal of Modern Physics D*, 23(07):1430014, 2014.
- [103] Atanu Kumar. Covariant perturbations through a simple nonsingular bounce. *Physical Review D*, 89(8):084059, 2014.
- [104] Michael Boyle, Daniel Hemberger, Dante AB Iozzo, Geoffrey Lovelace, Serguei Ossokine, Harald P Pfeiffer, Mark A Scheel, Leo C Stein, Charles J Woodford, Aaron B Zimmerman, et al. The sxs collaboration catalog of binary black hole simulations. *Classical and Quantum Gravity*, 36(19):195006, 2019.
- [105] Béla Szilágyi, Jonathan Blackman, Alessandra Buonanno, Andrea Taracchini, Harald P Pfeiffer, Mark A Scheel, Tony Chu, Lawrence E Kidder, and Yi Pan. Approaching the post-newtonian regime with numerical relativity: a compact-object binary simulation spanning 350 gravitational-wave cycles. *Physical Review Letters*, 115(3):031102, 2015.
- [106] Juan Maldacena. The large-n limit of superconformal field theories and supergravity. *International journal of theoretical physics*, 38(4):1113–1133, 1999.
- [107] Steven S Gubser, Igor R Klebanov, and Alexander M Polyakov. Gauge theory correlators from non-critical string theory. *Physics Letters B*, 428(1-2):105–114, 1998.
- [108] Edward Witten. Anti de sitter space and holography. *Advances in Theoretical and Mathematical Physics*, 2(2):253–291, 1998.

-
- [109] R. C. Myers and M. J. Perry. Black holes in higher dimensional space-times. *Annals Phys.*, 172(304):525–543.
 - [110] Roberto Emparan and Harvey S. Reall. A rotating black ring solution in five dimensions. *Physical Review Letters*, 88(10), feb 2002.
 - [111] Henriette Elvang and Pau Figueras. Black saturn. *Journal of High Energy Physics*, 2007(05):050, 2007.
 - [112] Hirotaka Yoshino and Masaru Shibata. Higher-dimensional numerical relativity: Formulation and code tests. *Physical Review D*, 80(8):084025, 2009.
 - [113] David Brown, Olivier Sarbach, Erik Schnetter, Manuel Tiglio, Peter Diener, Ian Hawke, and Denis Pollney. Excision without excision. *Physical Review D*, 76(8):081503, 2007.
 - [114] David Brown, Peter Diener, Olivier Sarbach, Erik Schnetter, and Manuel Tiglio. Turduckening black holes: an analytical and computational study. *Physical Review D*, 79(4):044023, 2009.
 - [115] Satish Balay, William D Gropp, Lois Curfman McInnes, and Barry F Smith. Efficient management of parallelism in object-oriented numerical software libraries. *Modern software tools for scientific computing*, pages 163–202, 1997.
 - [116] Demetrios Christodoulou. On the global initial value problem and the issue of singularities. *Classical and Quantum Gravity*, 16(12A):A23, 1999.
 - [117] J Tafel and M Jóźwikowski. New solutions of initial conditions in general relativity. *Classical and Quantum Gravity*, 31(11):115001, 2014.
 - [118] D Christodoulou. The formation of black holes in general relativity on recent developments in theoretical and experimental general relativity, astrophysics and relativistic field theories. 1:3, 2009.
 - [119] Gary T Horowitz, Jorge E Santos, and Benson Way. Evidence for an electrifying violation of cosmic censorship. *Classical and Quantum Gravity*, 33(19):195007, sep 2016.
 - [120] Toby Crisford and Jorge E. Santos. Violating the weak cosmic censorship conjecture in four-dimensional anti-de sitter space. *Physical Review Letters*, 118(18), may 2017.
 - [121] Matthew Choptuik, Luis Lehner, Ignacio (Inaki) Olabarrieta, Roman Petryk, Frans Pretorius, and Hugo Villegas. Towards the final fate of an unstable black string. *Phys. Rev. D*, 68(044001), 2003.
 - [122] Stephen W Hawking and George FR Ellis. *The large scale structure of space-time*. Cambridge university press, 2023.
 - [123] Jens Eggers. Universal pinching of 3d axisymmetric free-surface flow. *Physical Review Letters*, 71(21):3458, 1993.
 - [124] Umpei Miyamoto. One-dimensional approximation of viscous flows. *Journal of High Energy Physics*, 2010(10):1–18, 2010.

-
- [125] Paul Painlevé. La mécanique classique et la théorie de la relativité. *Comptes Rendus Academie des Sciences (serie non specifiée)*, 173:677–680, 1921.
 - [126] Allvar Gullstrand. Allgemeine lösung des statischen einkörperproblems in der einsteinschen gravitationstheorie. 1922.
 - [127] A. Lapidus. A detached shock calculation by second-order finite differences. *J. Comput. Phys.*, 2(154), 1967.
 - [128] J.Donea and A.Huerta. Finite element methods for flow problems. 2003.
 - [129] J. Von Neumann and R. D. Richtmyer. A method for the numerical calculation of hydrodynamic shocks. *J. Appl. Phys.*, 21(232), 1950.
 - [130] Tomas Andrade, Pau Figueras, and Ulrich Sperhake. Violations of weak cosmic censorship in black hole collisions. *arXiv preprint arXiv:2011.03049*, 2020.
 - [131] Helvi Witek, Vitor Cardoso, Leonardo Gualtieri, Carlos Herdeiro, Ulrich Sperhake, and Miguel Zilhao. Head-on collisions of unequal mass black holes in D=5 dimensions. *Physical Review D*, 83(4):044017, 2011.
 - [132] Roberto Emparan. Predictivity lost, predictivity regained: a miltonian cosmic censorship conjecture. *International Journal of Modern Physics D*, 29(14):2043021, 2020.
 - [133] Aron D Kovacs and Harvey S Reall. Well-posed formulation of scalar-tensor effective field theory. *Physical Review Letters*, 124(22):221101, 2020.
 - [134] Aron D Kovacs and Harvey S Reall. Well-posed formulation of lovelock and horndeski theories. *Physical Review D*, 101(12):124003, 2020.
 - [135] Llibert Aresté Saló, Katy Clough, and Pau Figueras. Well-posedness of the four-derivative scalar-tensor theory of gravity in singularity avoiding coordinates. *Physical Review Letters*, 129(26):261104, 2022.

Appendix A

Symmetry reduction terms

$$\tilde{\Gamma}_{ww}^i = -\frac{1}{2}\tilde{\gamma}^{ik}\partial_k\tilde{\gamma}_{ww} + \frac{\delta_z^i - \tilde{\gamma}^{iz}\tilde{\gamma}_{ww}}{z} \quad (\text{A.1})$$

$$\tilde{\Gamma}^i += N\tilde{\gamma}^{ww}\tilde{\Gamma}_{ww}^i \quad (\text{A.2})$$

$$D_w D_w \alpha = \tilde{\gamma}_{ww}\tilde{\gamma}^{dk}\frac{\partial_k\alpha}{z} + \frac{1}{2}\tilde{\gamma}^{kl}\left((\partial_k\tilde{\gamma}_{ww})(\partial_l\alpha) - \frac{\tilde{\gamma}_{ww}}{\chi}(\partial_k\chi)(\partial_l\alpha)\right) \quad (\text{A.3})$$

$$\partial_t\chi += -\frac{2}{D-1}\chi N\frac{\beta^z}{z} \quad (\text{A.4})$$

$$\partial_t\tilde{\gamma}_{ij} += -\frac{2}{D-1}\tilde{\gamma}_{ij}N\frac{\beta^z}{z} \quad (\text{A.5})$$

$$\partial_t\tilde{\gamma}_{ww} += \beta^m\partial_m\tilde{\gamma}_{ww} - \frac{2}{D-1}\tilde{\gamma}_{ww}\left(\partial_m\beta^m - d\frac{\beta^z}{z}\right) - 2\alpha\tilde{A}_{ww} \quad (\text{A.6})$$

$$\begin{aligned} \mathcal{R}_{ij}^{\text{ex}} := & \frac{N}{2\chi}\left(\frac{1}{2}\tilde{\gamma}^{ww}\tilde{\gamma}^{kl}\partial_l\tilde{\gamma}_{ww} + \frac{\tilde{\gamma}^{kz}}{z}\right)\partial_k\chi + N\tilde{\gamma}^{ww}\left(-\frac{1}{2}\frac{\partial_z\tilde{\gamma}_{ij}z}{+}\delta_{z(i}\tilde{\gamma}_{j)z} - \frac{\delta_{iz}\delta_{jz}\tilde{\gamma}_{ww}}{z^2}\right. \\ & \left. + \frac{\tilde{\gamma}^{ww}\tilde{\gamma}_{d(j}-\delta_{d(j)}\partial_i)\tilde{\gamma}_{ww}}{z} - \frac{1}{4}\tilde{\gamma}^{ww}(\partial_i\tilde{\gamma}_{ww})(\partial_j\tilde{\gamma}_{ww})\right) = R_{ij}^{\text{ex}} \end{aligned} \quad (\text{A.7})$$

$$\begin{aligned} \mathcal{R}_{ww} = & \frac{\tilde{\gamma}_{ww}}{2\chi}(\tilde{\gamma}^{mn}\tilde{D}_m\tilde{D}_n\chi + (D+N-3)\left(\frac{1}{2}\tilde{\gamma}^{ww}\tilde{\gamma}^{mn}\partial_n\tilde{\gamma}_{ww} + \frac{\tilde{\gamma}^{mz}}{z}\right)\partial_m\chi \\ & - \frac{D-1}{2\chi}\tilde{\gamma}^{mn}\partial_m\chi\partial_n\chi) - \frac{1}{2}\tilde{\gamma}^{mn}\partial_m\partial_n\tilde{\gamma}_{ww} + \frac{1}{2}\tilde{\gamma}^{ww}\tilde{\gamma}^{mn}\partial_m\tilde{\gamma}_{ww}\partial_n\tilde{\gamma}_{ww} - \frac{N}{2}\tilde{\gamma}^{ww}\frac{\partial_z\tilde{\gamma}_{ww}}{z} \\ & + \tilde{\gamma}_{ww}\frac{\bar{\Gamma}^z}{z} + \frac{1}{2}\bar{\Gamma}^m\partial_m\tilde{\gamma}_{ww} + \frac{\tilde{\gamma}^z\tilde{\gamma}_{ww}-1}{z^2} - \frac{\gamma_{ww}}{\chi}Z^k\partial_k\chi + \tilde{Z}_k\partial_k\tilde{\gamma}_{ww} \end{aligned} \quad (\text{A.8})$$

$$\partial_t K += -N\chi\tilde{\gamma}^{ww}D_w D_w \alpha + \alpha\left((\mathcal{R}^{\text{ex}})_k^k + N\mathcal{R}_w^w\right) \quad (\text{A.9})$$

$$\partial_t\Theta += \frac{\alpha}{2}\left(-N(\tilde{\gamma}^{ww}\tilde{A}_{ww})^2 + (\mathcal{R}^{\text{ex}})_k^k + N\mathcal{R}_w^w\right) \quad (\text{A.10})$$

$$\partial_t \tilde{A}_{ij} += -\frac{2}{D-1} \tilde{A}_{ij} N \frac{\beta^z}{z} + \chi \left(\alpha \left((\mathcal{R}^{\text{ex}})_{ij}^{\text{TF}*} - \frac{N}{D-1} \gamma_{ij} \mathcal{R}_w{}^w \right) + \frac{N}{D-1} D^w D_w \alpha \right) \quad (\text{A.11})$$

$$\begin{aligned} \partial_t \tilde{A}_{ww} += & \beta^m \partial_m \tilde{A}_{ww} - \frac{2}{D-1} \tilde{A}_{ww} \left(\partial_m \beta^m - d \frac{\beta^z}{z} \right) + \alpha \tilde{A}_{ww} (K - 2\tilde{\gamma}^{ww} \tilde{A}_{ww} \\ & + \chi (\alpha (\mathcal{R}_{ww} - 8\pi S_{ww}) - D_w D_w \alpha)^{TF} - 2\alpha \tilde{A}_{ww} \Theta \end{aligned} \quad (\text{A.12})$$

$$\begin{aligned} \partial_t \hat{\Gamma}^i += & \hat{\Gamma}_{\text{ex}}^i := \frac{2}{D-1} (\tilde{\Gamma}^i + 2\kappa_3 \tilde{Z}^i) N \frac{\beta^z}{z} + N \tilde{\gamma}^{ww} \left(\frac{\partial_z \beta^i}{z} - \delta_z^i \frac{\beta^z}{z^2} \right) \\ & + \frac{D-3}{D-1} N \left(\tilde{\gamma}^{ik} \frac{\partial_k \beta^z}{z} - \tilde{\gamma}^{iz} \frac{\beta^z}{z^2} \right) + 2\alpha N \tilde{\Gamma}_{ww}^i \tilde{A}^{ww} \end{aligned} \quad (\text{A.13})$$

$$\partial_t B += \hat{\Gamma}_{\text{ex}}^i \quad (\text{A.14})$$

$$\mathcal{H} += (R^{\text{ex}})_k{}^k + N R_w{}^w - N \tilde{A}_{ww} \tilde{A}^{ww} \quad (\text{A.15})$$

$$\mathcal{M}^i += N \frac{\tilde{A}^{zi} - \delta_{zi} \tilde{A}^{ww}}{z} + \tilde{\Gamma}_{ww}^i \tilde{A}^{ww} \quad (\text{A.16})$$

where $i, j, m, n = 1, 2$.

Appendix B

Numerical test

The typical resolution of our simulations has the coarsest grid spacing of $h = 0.25r_0$. In addition, we carry out several extra runs with lower or higher resolutions for the $L = 10$ case. Specifically, we have $\Delta_{\text{low}} = \frac{10}{7}h$, $\Delta_{\text{medium}} = \frac{7}{5}h$ and $\Delta_{\text{high}} = \frac{2}{3}h$. We monitor the evolution of the AH area and present the convergence results in Fig. B.1 and Fig. B.2 as a supplement to the convergence results in Chapter 4.5.

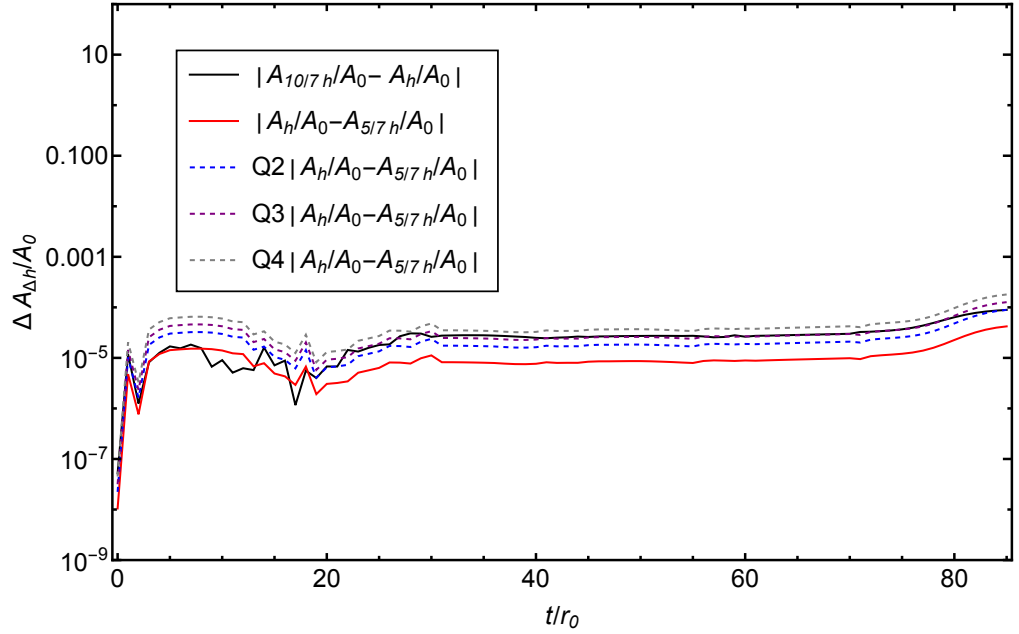


Fig. B.1 Convergence test for the AH area for the $r_0 = 1$, $L = 10$ black string. This plot shows that the order of convergence is roughly three. The computational cost of the high resolution run limited the time of the tests.

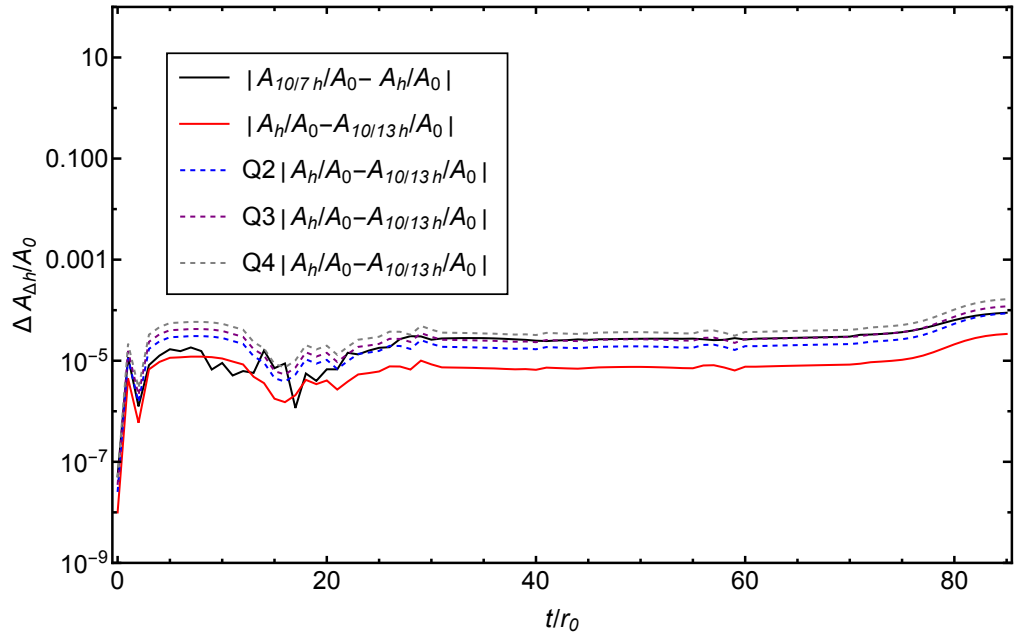


Fig. B.2 Convergence test for the AH area for the $r_0 = 1$, $L = 10$ black string. This plot shows that the order of convergence is roughly three. The computational cost of the high resolution run limited the time of the tests.

Due to limited computational cost, we only evolve the low and the high resolution runs for a limited amount of time, but in all the cases, the order of convergence during the evolution is roughly 3. This is what we would expected.